Leveraging Capillarity

Kevin R. Murphy

Dissertation submitted to the Faculty of the
Virginia Polytechnic Institute and State University
in partial fulfillment of the requirements for the degree of

Doctor of Philosophy
in
Engineering Mechanics

Jonathan B. Boreyko, Chair
Jiangtao Cheng
Mark S. Cramer
Scott T. Huxtable
Anne E. Staples

August 3rd, 2022
Blacksburg, Virginia

Keywords: Interfacial phenomena, dropwise condensation, liquid bridges, frost, SLIPS

Leveraging Capillarity

Kevin R. Murphy

(Abstract)

Surface tension is an essential force for the functioning of the world and life. Centuries of study, and still, new applications and limits of surface tension are being explored. Water has always drawn attention for its high surface tension value, 72 mN/m compared to ethanol's 20 mN/m. The high surface tension allows for numerous applications, superhydrophobic surfaces being one that takes heavy advantage of that value. Superhydrophobic surfaces have a high surface energy cost with water, resulting in small contact areas with high advancing and receding contact angles and low contact angle hysteresis. This results in very low adhesion on the surfaces. Here we study the ability of superhydrophobic surfaces with their low adhesion to shed meltwater from frost, showing a decrease in frost thickness to below 3 mm for the meltwater to shed. We then take another approach to removing water from a surface, rather than increasing the surface energy cost, we introduce a difference in surface energy cost. Introducing a porous surface across from a solid one, droplets transfer from the solid to the porous, removing over 90% of the volume of the droplet from the solid surface. We thoroughly examine and model the hydrodynamics of the transfer process, varying the solid surface, the donor surface, and the liquid. This bridging between surfaces is then applied to fog harps, examining the efficiencies of large-form fog harps. Fog harps have shown a 3 to 5 times increase in water collection compared to the industry-standard mesh collector. However, droplets from fog collected on the wires eventually grow large enough to touch neighboring wires. To minimize their surface energy, they begin pulling wires together, "tangling" them. This can potentially reduce efficiency, but has not been applied to large-scale harps until here. Another application of surface tension is then examined, using lower surface tension oils, but trapping them in microstructures to make slippery liquid-infused porous surfaces (SLIPS). The oil coats the microstructure, due to its lower surface tension. This creates a lubricating layer on the surface, along with potential air pockets reducing friction further. These surfaces have been studied extensively with liquids being placed on them, but here we begin to examine them when solids are used instead, showing some interesting cases where increasing the viscosity of the oil actually decreases the friction force.

Leveraging Capillarity

Kevin R. Murphy

(General Audience Abstract)

Sponges are something everyone has used, and most people can tell you that they work using surface tension. And for most people, that's enough. It's actually more useful to know to squeeze your sponge dry when you're done to prevent mold, than it is to know that it holds onto liquids because of surface tension. But the point here was to take the study of sponges and surface tension to the extreme. To the point that some knowledge is going to be gained solely for the sake of gaining knowledge. Not all knowledge will have immediate uses, but this doesn't take value away from the knowledge, or any eventual uses it might have.

So we start this by looking at the building of scientific knowledge and noticing that a brick is missing. Superhydrophobic surfaces, surfaces that water doesn't want to touch, have been studied very extensively and their properties have been thoroughly explored. However a direct comparison of the defrosting behaviors, the process of frost melting on a surface, between superhydrophobic and hydrophobic surfaces had not been done. Water does prefer to be on a hydrophobic surface compared to a superhydrophobic one, but it's still uncomfortable. A plate was treated so that half was hydrophobic and the other half was superhydrophobic. Frost was grown across the surface and then melted simultaneously, allowing us to characterize the differences in the behaviors, highlighting the ability of the superhydrophobic surface to shed water droplets at smaller sizes than other surfaces.

Next is a pure fluid mechanics work supporting a heat transfer application. Evaporation, for enhanced heat transfer, and a hydrophilic wick, essentially a sponge, are paired to create a plate with one-way heat transfer. Heating side A can heat side B, but heating side B can't heat side A. Water in the wick gets heated, evaporates from side A and then condenses on side B, carrying heat with it. The condensation grows until it touches the wick, which then pulls it in, allowing it to be evaporated again and cycling more heat. When side B, the smooth surface, is heated, the water can evaporate off it and condense in the wick, but then it has no way to return, preventing further heat transfer. The process of droplets being pulled from side B to the wick in side A is key to the process. It's a sponge pulling water in using surface tension. However, all the smaller pieces have been taken for granted. The second piece is a systematic study of this capture mechanism, exploring the effects of changing liquids, donor surfaces, and receiving porous wicks.

Third is a continuation of the lab's previous work on Fog Harps, arrays of vertical fibers held in place to let fog run into them. The droplets grow until they slide down and can be collected. The wires of the harp are close enough that the water can actually start to tangle them together. This tangling can increase the water needed for sliding and collection to begin. Tensioning the wires can help mitigate the tangling. Here we show harps on around $1\,\mathrm{m}^2$, using optimal wire size and spacing that is possible for mass manufacturing. The harps were tested in the lab using humidifiers to generate fog for the harps to collect.

Finally, an initial study of solid objects being pulled across oil-infused microstructured surfaces. The microstructure helps keep the oil on the surface thanks to the surface energy of the oil. These oil-infused surfaces have been studied extensively when liquids are placed on them, but not with solid objects. Solid objects can exert significantly more pressure than liquids, which naturally want to spread when they reach a certain thickness. Experiments were performed with a variety of oil viscosities, microstructures, and oil excess thicknesses. This work is not entirely complete but a significant portion of it is presented here.

For my parents, who ensured that I do not ever need to worry about earning before deciding on pursuing higher education and who taught me that doing something is always better than doing nothing.

Acknowledgments

**"The most important step a man can take. It's not the first one, is it?
It's the *next* one. Always the next step Dalinar."**

**"The most important words a man can say are 'I will do better.'
These are not the most important words *any* man can say.
I am a man, and they are what I needed to say."**

Both from Oathbringer by Brandon Sanderson

I'm writing this particular section on my 28th birthday. It's strange since, for me, each birthday has always seemed very similar to the day before and after it, and I wasn't trying to finish this by a certain age, but here I am. But I will try to be as genuine as possible, knowing that I often miss the mark and default to silence when any words at all would mean more. I also hoped to have picked some quotes that are pertinent to the moment, despite only having come across them in the last month, and the sheer amount of music I've listened to and loved in my life. Particularly Green Day. Thank you Mom and Dad for inspiring in me a love of music.

To get back on topic, this document is the culmination of not just the last 6 years of work, but of the effort, advice, and encourgament of many, some of whom I will inevitably forget. I shall still attempt to thank those deserve it most. So, here we go.

To my entire extended family, seemingly uncountable cousins and aunts and uncles from both sides, thank you for all of the words of encouragement you have given me over the years.

To my labmates in the Nature Inspired Fluids and Interfaces Lab, thank you. To the undergrads who still welcomed me for Dungeons and Dragons even though I was a grad student, to the grad students who welcomed me when I first joined as an undergrad, you are wonderful, and I can't thank you enough. Farzad, you never shied away from a problem or responsibility, regardless of how many others were on your plate. Saurabh, your dedication to the craft of research was daunting at times, but always amazing. I am astounded by the work you did and continue to do, all of which was driven by an intellect I loved every insight to, even when I didn't understand what you were talking about at the time.

Ranit, you were a rock, unmovable and unstoppable. I don't ever recall a moment where you

hesitated with your Ph.D. or on a project, despite anything that happened. Weiwei, your work ethic is, and probably forever will be, unmatched. You are an outlier among outliers. I am honored to have worked closely with and have known you both.

To all of my committee, thank you again for your time, and in particular for your understanding with the delays for my exams. I'm grateful for every attempt to find holes in my work that need to be fixed in order to make it better.

For my friends from before. Joe Jajonie, you were a loose cannon, and hope you still are to some degree. I wouldn't have it any other way. Your drive for always serving the world around you, even if it meant going against the grain, was amazing. To the entire dorm of West Ambler Johnston when I was there, you were friends when I needed them most.

Sophie, you probably put up with the most nonsense from me of anyone in my life, excluding my parents. Thank you for still being here some 12 years later. Amy, thank you in particular for all of your help regarding my mental health. Your words in December of 2019 got me back to work in January of 2020. They were the spark that got me back on track.

Robert Killefer IV. You are my brother. We are complete opposites in many ways. But my graditude to you is beyond words. A trip to Spain will be on me in the near future. I love you man.

Luz, any door I can open for you, I will. After that I want to see what you do. I want to see you love life and run forward headfirst with almost reckless abandon for whatever you want. Almost.

Dad. Thank you for always being a source of consistency. The world keeps moving. You taught me to find things in it to enjoy. Money or a title never mattered as much as enjoying what you were doing.

Mom. You moved everything to help me on multiple occasions, and threatened to on many more. Your help was more than I could ever ask or hope for. In some cases, it was almost too much, but was never unwelcome. I love you and Dad both immeasurably.

Professor Boreyko. I think I will always wonder how much of a risk I was for you. I didn't stand out in your class. I didn't have a stellar record in undergrad. It seemed you took me on simply because I came back a month later to ask about undergraduate research when you said to. You got me into graduate school when I had at best a 2.7 GPA and the requirement was a 3.0 and no other school accepted me. Your continued guidance throughout the 8 years of working for you has been incredible. I can't begin to express my gratitude at your understanding during my health problems. And your trust in my in these past two years has been a massive boost to me, even when I wasn't sure it was justified. I hope I continue to be worthy of that trust.

With that, time to take one of the last steps in this particular journey. Another step towards the destination.

Contents

List of Tables

List of Figures

Symbols

γ	Surface Tension, assumed liquid-air
ΔP	Pressure Drop
R_1, R_2	Radii of Curvature of an Interface
θ	Apparent Contact Angle of a Liquid on a Surface
γ_{lg}	Liquid-Gas Surface Tension
γ_{ls}	Liquid-Solid Surface Tension
γ_{sg}	Solid-Gas Surface Tension
R	Radius of Curvature of a Droplet
R'	Adjusted Radius of Curvature of Droplet
θ_R	Receding Contact Angle
θ_A	Advancing Contact Angle
τ_{ice}	Shear Stress to Break Ice
T_∞	Ambient Temperature
P_∞	Ambient Pressure
RH	Relative Humidity
h_f	Frost Thickness
T_p	Temperature of Plate during Frost Growth
P_s	Saturation Pressure
α	Tilt Angle for Melting
V	Droplet Volume
a	Droplet Contact Radius
g	Acceleration of Gravity
$F^\star$	Non-Dimensional Paramter of Droplet Sliding
$\dot{q}$	Heat Power per Area
t_{SHPB}	Time for Removal on a Superhydrophobic Surface
t_{HPB}	Time for Removal on a Hydrophobic Surface
m_{frost}	Mass of Frost Layer
L_f	Latent Heat of Fusion
L_v	Latent Heat of Vaporization
$E^\star$	Non-Dimensional Energy for Frost Sheet Removal

ρ_{frost}	Frost Density
ϕ	Solid Fraction
θ_Y	Young's Angle
$E_c^\star$	Critical Non-Dimensional Energy for Frost Sheet Removal
h_c	Critical Height for Frost Removal
$h_{c,SHPB}$	Critical Height for Frost Removal on a Superhydrophobic Surface
$h_{c,HPB}$	Critical Height for Frost Removal on a Hydrophobic Surface
D_c	Critical Droplet Diameter for Shedding
ρ	Density
μ	Dynamic Viscosity
h	Height of Gap between Surfaces
r_d	Donor Contact Radius
r_r	Receving Contact Radius
θ_r	Apparent Receiving Contact Angle
θ_d	Apparent Donor Contact Angle
r_p	Pore Radius
t	Time
t_wet	Wetting Timescale
t_wick	Wicking Timescale
t_{ci}	Capillary-Inertial Timescale
t_{vc}	Viscocapillary Timescale
Oh	Ohnesorge Number
v_{ci}	Capillary-Inertial Velocity
v_{vc}	Viscocapillary Velocity
τ	Tortuosity
CP	Non-Dimensional Coupling Parameter
t_{cross}	Crossover Timescale
β_{vc}	Viscocapillary Fitting Factor
β_{ci}	Capillary-Inertial Fitting Factor
dz	Height of the Flow Field Inside the Droplet during Bridging
ΔP_{adv}	Laplace Pressure at the Advancing Contact Line

ΔP_{rec}	Laplace Pressure at the Receding Contact Line
ΔP_{ρ}	Inertial Pressure Drop
ΔP_{μ}	Viscous Pressure Drop
v_r,$\dot{r}_r$	Velocity of the Receiving Contact Radius
v_d,$\dot{d}_r$	Velocity of the Donor Contact Radius
$\Delta P_{\mu,Global}$	Viscous Pressure Drop across the Liquid Bridge
$\Delta P_{\mu,Local}$	Viscous Pressure Drop across the Viscous Wedge
h_{μ}	Viscous Wedge Height
∇P	Pressure Gradient
v_{wick}	Wicking Velocity
κ	Permeability
L	Wicking Length
R_c	Radius of Curvature of a Droplet on the outside of the Porous Surface
s	Position along the Curve of the Bridge Profile
L_i	Wicked Length at Frame i
i	Frame Number
L_0	Initial Wicked Length
Λ	Non-Dimensional Height of Liquid Bridge
K	Non-Dimensional Aspect Ratio of Contact Radii
$V^{\star}$	Non-Dimensional Volume of the Liquid Bridge
P	Pitch/Center-to-Center Distance between Wires
D	Diameter of Wires
n	Number of Wires Tangling
a_{cap}	Position of Droplet Center from Wire Edge for Capture
R_{wire}	Radius of the Wires
L_{dry}	Dry Length of Wires
L_{wet}	Wet Length of Wires
h_p	Height of the Pillars
w	Width of the Pillars
ν	Kinematic Viscoity
ω	Spin Coat Speed

δ_0	Initial Oil Thickness
U	Pull Velocity
W_c	Width of the Cube
F_F	Friction Force
z_c	Distance from the Pillar Tops to the bottom of the Cube
t_s	Spin Coat Duration
ΔP_{Cube}	Pressure Drop from the Cube Weight
U_t	Max Velocity of Flow above Pillar Tops
Q_t	Volumetric Flow Rate from the Pillar Tops
$\dot{z_c}$	Speed of Cube Sinking
F_{SD}	Stoke's Drag Force
F_g	Gravitation Force
F_n	Normal Force
F_{Pull}	Pulling Force
x_n	Position of the Effective Normal Force

Abbreviations

SHPB	Superhydrophobic (A surface with very low adhesion for water).
SLIPS	Slippery Liquid-Infused Porous Surface (A surface with a microsturcture filled with oil)
HPB	Hydrophobic
HPL	Hydrophilic
CFD	Computational Fluid Dynamics

Attributions

Some chapters of this thesis include material already published in or submitted to peer-reviewed journals, as detailed below.

Still need some of this information.

Chapter 3: Defrosting of Superhydrophobic Surfaces

Originally published as: Dynamic Defrosting on Superhydrophobic Surfaces, Kevin R. Murphy, William T. McClintic, Kevin C. Lester, C. Patrick Collier, and Jonathan B. Boreyko, *ACS Applied Materials and Interfaces*, **9**, 2017, 24308-24317, DOI: 10.1021/acsami.7b05651

J.B.B. conceived the research. J.B.B., K.C.L., and C.P.P. designed the research. J.B.B. and K.C.L. fabricated the surfaces. W.T.M. conducted the experiments. K.R.M. performed the image processing and data analysis. K.R.M. and J.B.B. developed the theoretical models. K.R.M. and J.B.B. wrote the paper, and all authors proofread and polished the manuscript.

Chapter 4: Porous Bridging

Accepted as: Bridging-Droplet Transfer from Solid to Porous Surfaces, Kevin R. Murphy and Jonathan B. Boreyko, *Journal of Fluid Mechanics*, Accepted August 2022.

J.B.B. conceived the research. K.R M. carried out the experiments and analyzed the data and images. Modeling was derived and the manuscript was written by J.B.B. and K.R.M. Both authors proofread, added comments, and approved the manuscript.

Chapter 5: Full Scale Fog Harps: Limits of Lab Testing

This work has not been submitted or published yet.

Jonathan B. Boreyko conceived the research. Experiments were performed and data was analyzed by Kevin Murphy and James Kaindu. Modeling was derived by Jonathan B. Boreyko, Kevin R. Murphy, and James Kaindu.

Chapter 6: Solids being pulled on SLIPS surfaces

This work has not been submitted or published yet.

Jonathan B. Boreyko conceived the research. Experiments were performed by Mohammad Habibi and Ziad Rashed. Data was analyzed by Ziad Rashed and Kevin R. Murphy. Modeling was developed by Kevin R. Murphy and Jonathan B. Boreyko.

Chapter 1

Background

1.1 Capillarity

Each of these projects is dependent on the usage of surface tension (force/length), or surface energy (energy/area), symbolized by γ. Surface tension at a contact line manifests as a force, $F = \gamma L$. Every interface has a related energy "cost", the larger the surface, the higher the cost ($E = \gamma A$). The cost is also dependent on the two substances, a water-oil interface has a different cost from a water-air interface, manifesting as changes in γ.

The size and type of interface matter, but also the curvature of the interface matters. As an interface is a two-dimensional object, it has two radii of curvature at each point, which can be converted to a pressure at each point. This is the known as Laplace Pressure [2]:

$$\Delta P = \gamma \left(\frac{1}{R_1} + \frac{1}{R_2} \right) \tag{1.1}$$

The curvatures in figure 1.1 can be calculated for every position along an interface. If the ambient pressure is the same at all points, but the curvatures are not, and therefore the Laplace pressures are not constant, flow will occur within the liquid [3].

Surface energy, surface tension, and Laplace pressure are all different faces of the same die. The processes investigated here take advantage of minimizing surface energy and pressure gradients resulting from Laplace pressures varying across a surface. A liquid can change to a shape with a larger contact area if surface energy is minimized. This is critical for a slipper liquid infused porous surface(SLIPS), where an oil is used that cloaks over a microstructure, as the oil-silicon and oil-air interfaces actually have lower total surface energy than just the silicon-air interface. All of these processes rely on the concept of capillarity, but that is one of the few things these projects have in common.

1.2 Contact Lines

One of the major manifestations of surface tension is a three-phase contact line. Each of the three interfaces present contribute to the behavior of the contact line. The forces are not

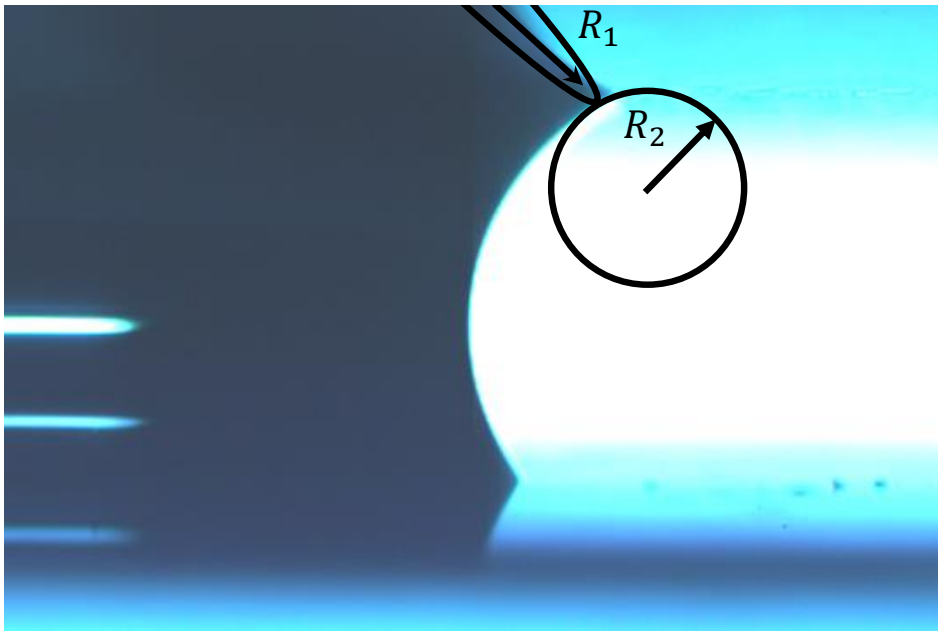

Figure 1.1: A liquid-air interface with 2 radii of curvature, the combination of which is correlated to the Laplace pressure drop across the interface.

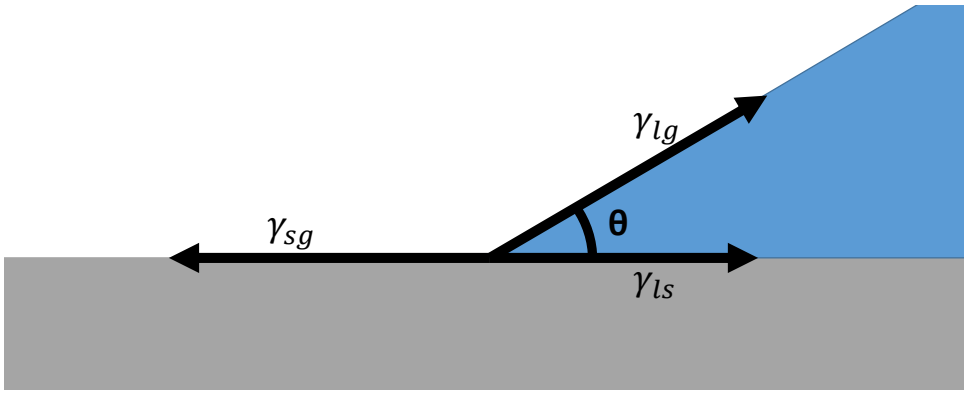

Figure 1.2: A three-phase contact line, balancing the surface tensions of the solid-liquid, liquid-gas, and solid-gas interfaces. Young's equation mathematically describes the relationship between the surface tensions and the contact angle.

inherently balanced, with the movement of the contact line being dependent on the contact angle, θ, of the water. As θ decreases, the contact line can start to recede if the solid-liquid and liquid-gas surface tensions begin to outweigh the solid-gas surface tension. The reverse is true as θ increases for an advancing contact line. The points at which the contact line moves are known as the receding contact angle, θ_R, and advancing contact angle, θ_A for the low and high angle respectively. The difference between the two angles is known as the contact angle hysteresis. The larger the hysteresis is, the more that is required for the droplet to

move. These angles, and thus the hysteresis, can be manipulated heavily by chemicals and microstructures on the surface. Chemical treatments can increase or decrease the contact angles depending on interactions with the fluid on them, while physical microstructures will increase contact angles that are above 90 ° and decrease contact angles that are below 90 °.

A stationary contact line can have a contact angle of any value between the advancing contact angle and the receding contact angle. Each combination of surface tensions will have a theoretical equilibrium contact angle called the Young's Contact Angle, θ_Y [2], which can be calculated from the following:

$$Cos(\theta_Y) = \frac{\gamma_{sg} - \gamma_{ls}}{\gamma_{lg}} \tag{1.2}$$

Liquids may not sit at this contact angle though. This equation only takes into account surface tensions and does not consider any structures or defects on the surface, producing apparent contact angles that differ from the Young's equilibrium contact angle.

1.3 Work of Adhesion

Taking the surface energy side allows for analyzing the problem of changing interfaces using work of adhesion. Work of adhesion is the cost of creating new interfaces or breaking old ones [4]. The simplified version of this is $dE = d\gamma A$, relating an energy cost to a change in surface energy. The change in surface energy can come from a change in surface tensions or a change in surface area. An example of a change in surface energy costs could be a droplet hitting a surface, changing the surface energy cost from the liquid-gas to a mix of liquid-gas and liquid-solid. This is joined by the change in area from a droplet impacting a surface and spreading out based on its inertia. The changing area of the interface will incur an energy cost as well as the changing interfaces.

The splitting of a droplet via the collapse of a liquid bridge can result in two liquid-gas interfaces or liquid-liquid interfaces being created incurring an energy cost for the process.

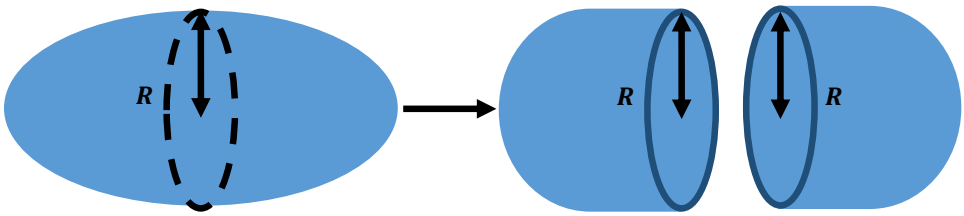

Figure 1.3: A droplet being split in half, with two liquid-air interfaces being created as a result.

The droplet being split requires an increase in surface area, as shown in figure 1.3. The

energy needed for the new interface area can be estimated by using $E = \gamma A$, with γ being known and $A = 2\pi R^2$. Some of this energy will be dissipated as the droplets move back to a spherical shape.

1.4 Energy Minimization

This brings us to the key mechanism of surface tension for these projects, energy minimization. Droplets naturally want to be in the shape of a sphere, the lowest ratio of surface area to volume possible. This minimizes the surface energy cost of the droplet, and deforming the droplet takes energy input, or an introduction of another surface to interact with. On top of this, the droplet will not naturally stay in another shape. This is because the energy cost increases as the deformation increases, resulting in energy costs continuously decreasing as the droplet moves back closer to being a sphere. The reason a rain drop has the shape it does is because it is falling through air, continually being deformed by the wind as it falls. This continuous desire to decrease surface energy is essential for using surface tension in engineering applications. Instabilities such as the Rayleigh-Plateau and Rayleigh-Taylor instabilities are caused by liquids minimizing their surface energy by splitting larger bodies into smaller ones [2].

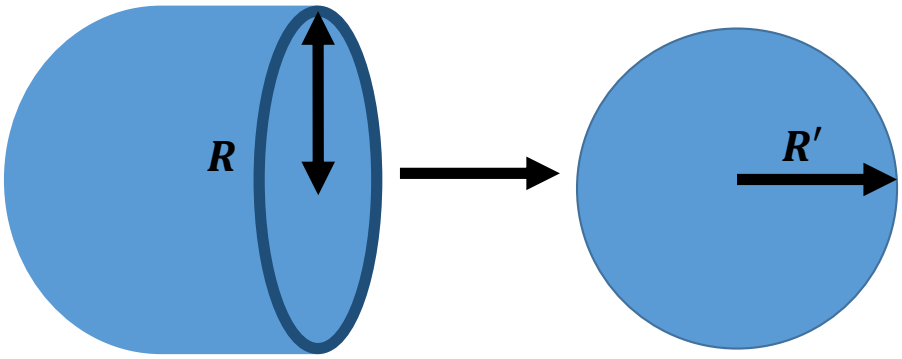

Figure 1.4: Half of a split droplet reducing it's surface energy by changing its shape to a sphere.

A split droplet will begin to reshape itself, with Laplace pressure differences manifesting at the areas created by the new interface. The droplet reduces it surface area until every point on its surface has the same curvature, reducing its surface energy cost, and eliminating Laplace pressure differences, as shown in figure 1.4. Two evenly split halves of a droplet will total about 50% more surface area, more surface energy than the droplet needed before splitting. Once each of the halves reduces its surface energy, the total will be about a 25% increase in surface area, dissipating the other 25% difference in energy. It's still required to input the 50% energy to start the process, even though the total net energy will be lesser.

Chapter 2

Introduction

2.1 Motivation

(*"Any sufficiently advanced technology is indistinguishable from magic."-Arthur C. Clarke*)

At first glance, the projects here seem rather disparate, not seriously connected together. They share the use of capillary action, some as a driving force, some as an enabling mechanism. In reality, these projects required significant chunks of knowledge that didn't directly apply to other projects. The crossover between them comes in the application of research principles. All of these projects stemmed from the question of "What if...?" What if the frost is grown on a superhydrophobic (SHPB) surface? What if the droplet is just touched by a wick? What if we used this screen to collect fog? What if the droplet is a solid object instead? Each of these had an application further down the road, but understanding why something works or doesn't work is essential for that application. The path resulting from the "What if...?" is rarely linear. You can guess how long a project is going to take but doing something new inevitably means solving problems that haven't been solved before. Part of good research is pushing to understand things better, especially if the results aren't what you were hoping for when you set out. And for me, understanding how something works only makes it more interesting.

For some people, learning how a magic trick is done makes it less interesting. It's the opposite for me. Understanding how a trick is done allows me to appreciate the technical skill required to perform the trick. The same is true of research but the tricks are performed by nature. There are few things more satisfying than graphing experiments on top of theory and having it match. That match is a peek into how nature works. I want to keep chasing that brilliance as long as possible.

2.2 Goals and Objectives

The goal of these projects is to understand the behavior of certain interfacial phenomena in a way that they can potentially be used for real world applications. Each of these four projects has a different focus, each geared towards a different application with different industrial impact. As such, each of those projects will introduce those in turn.

Objective 1: Defrosting of Superhydrophobic Surfaces

Recent studies have shown that frost can grow in a suspended Cassie state on nanostructured superhydrophobic surfaces [5, 6, 7, 8]. During defrosting, the melting sheet of Cassie frost spontaneously dewets into quasi-spherical slush droplets that are highly mobile. Promoting Cassie frost would therefore seem advantageous from a defrosting standpoint allowing water to potentially be removed by gravity rather than having to evaporate it; however, nobody has systematically compared the efficiency of defrosting Cassie ice versus defrosting conventional surfaces. Here, we characterize the defrosting of an aluminum plate, one half of which exhibits a superhydrophobic nanostructure while the other half is smooth and hydrophobic. For thick frost sheets ($> 1\,\mathrm{mm}$), the superhydrophobic surface was able to dynamically shed the meltwater, even at very low tilt angles. In contrast, the hydrophobic surface was unable to shed any appreciable meltwater even at a 90° tilt angle. For thin frost layers ($\lesssim 1\,\mathrm{mm}$), not even the superhydrophobic surface could mobilize the meltwater. We attribute this to the large apparent contact angle of the meltwater, which for small amounts of frost serves to minimize coalescence events and prevent droplets from approaching the capillary length. Finally, we demonstrate a new mode of dynamic defrosting using an upside-down surface orientation, where the melting frost was able to uniformly detach from the superhydrophobic side and subsequently pull the frost from the hydrophobic side in a chain reaction. Treating surfaces to enable Cassie frost is therefore very desirable for enabling rapid and low-energy thermal defrosting, but only for frost sheets that are sufficiently thick.

Objective 2: Systematic Study of Liquid Droplets Bridging from Solid to Porous Surfaces

When the top of a sessile droplet is contacted by an opposing solid surface, the droplet can transfer depending on the wettabilities and relative velocity of the surfaces. What if the surface receiving the liquid was porous? High-speed imaging was used to capture the transfer of a droplet from a solid substrate to an opposing porous surface. The parameters that were varied include the wettability of the donor substrate, the pore size of the receiving surface, and the droplet's volume and working fluid. Generally, the transfer process is split into two sequential regimes, wetting and wicking, with wicking being three orders of magnitude longer than wetting on average. The wetting regime is split into two sub-regimes, the donor-independent and donor-dependent regimes. The donor-independent regime follows the dynamics of droplet coalescence, starting in a mass-limited viscous regime followed by a capillary-inertial regime. The donor-dependent regime is driven by a global change in Laplace pressure across the liquid bridge, with the viscous wedge of the receding contact line being the rate-limiting factor. The wicking regime is governed by Darcy's Law, completing the transfer process of the droplet.

Objective 3: Practical Scale Fog Harps in the Lab

Fog harvesting has been used in numerous places around the world to address water scarcity [9, 10]. Compared to mesh netting, Fog Harps have been shown to increase the passive collection of water in both light and heavy fog [1, 11, 12, 13]. However, Fog Harps remain

constrained by wire tangling and scalability concerns. Here, we develop a Fog Harp that is mass manufacturable and can readily tune the wire tension to solve the tangling problem. For example, the fog collection efficiency in a heavy fog was doubled as the tension was increased to progress from five-wire tangling events down to four-wire tangling. Interestingly, the four-wire tangling performed similarly to a scale-model harp with no tangling, suggesting that full-scale harps greatly enhance the aerodynamic efficiency. We also updated our elastocapillary tangling model, revealing the maximum frame height for any desired wire tension where wire tangling would be avoided. The experimental results and correlated tangling model give a clear roadmap for developing mass manufacturable Fog Harps that are anti-tangling, to find the true performance ceiling of passive fog harvesters.

Objective 4: Modeling the Behavior of Solid Objects on SLIPS surfaces

SLIPS have been extensively studied when liquids are deposited on them, particularly due to the low adhesion and friction they exhibit for liquids. However, the friction hasn't been measured for solids. This is of particular interest as the microstructure used for a SLIPS is designed to hold oil in channels, allowing it to replenish the layer of oil on top of the microstructure where the object sits. This could allow for a decrease in the amount of oil drained during use, decreasing maintenance and oil used over time. This durability is of key importance in lubrication applications. Here we study the behavior of a solid aluminum cube being dragged across SLIPS with different microstructures, initial oil thicknesses, and oil viscosities. We then attempt to model the behavior of the cube from the moment it is placed on the surface through the twenty second pull on the surface.

2.3 Organization

Chapter 1 was a brief overview of capillary action and behaviors. This chapter, chapter 2, gives a short synopsis of each of the sections and how they relate to each other. Chapter 3 breaks down the differences in the behavior of frost on hydrophobic and superhydrophobic surfaces. In particular, the difference in shedding behavior during melting. Chapter 4 is a systematic study of sessile liquid droplets transferring from a solid surface to a porous surface. Chapter 5 analyzes the results of testing large scale harps in a lab setting. Chapter 6 explores the beginnings of studying solid objects moving across SLIPS. Chapter 7 breaks down the conclusions from each of the other chapters as well as the questions still to be answered from chapters 5 and 6 in particular.

Chapter 3

Defrosting of Superhydrophobic Surfaces

3.1 Introduction

Accretion of ice and frost on the surfaces of airplanes, wind turbines, transmission lines, and other infrastructure poses a serious problem to their efficiency and reliability, resulting in annual economic losses of many billions [14]. Motivated by this issue, many reports have investigated whether the robust water repellency of superhydrophobic surfaces could additionally minimize ice accretion, either by preventing freezing entirely or by greatly reducing the ice adhesion strength [15, 16]. The former strategy is often referred to as anti-icing, while the latter enhances mechanical or thermal de-icing. The anti-icing approach is enabled by two features of suspended Cassie droplets on superhydrophobic surfaces: their minimal contact angle hysteresis [17] and a delay in the onset of heterogeneous ice nucleation [18, 19, 20, 21, 22, 23, 24, 25]. These complementary traits can be exploited to rapidly shed impacting supercooled water from the surface before any freezing can occur [25, 26, 27, 28, 29].

While a chilled superhydrophobic surface is thus capable of preventing icing in a dry environment, the issue of achieving anti-icing under practical humid conditions is fundamentally different and much more problematic. Humidity results in the nucleation of supercooled condensation which subsequently freezes over into frost, a process known as condensation frosting [14]. On superhydrophobic surfaces that are microstructured, condensation grows in an impaled Wenzel state[30, 31], which prevents droplet mobilization and promotes even stronger ice adhesion than with traditional surfaces [26, 32, 33, 34, 35]. However, some hope for anti-icing was restored when it was discovered that when the superhydrophobic surface is nanostructured, condensation can now inflate into the desired Cassie state [36, 37, 38, 39, 40, 41, 42]. Supercooled condensation can therefore be removed from a nanostructured surface before freezing occurs, either by gravity for millimetric droplets [43, 44] or by coalescence-induced jumping for micro-droplets [45, 46]. Surprisingly, even when supercooled condensate are continually removed, the surface still frosts over due to an inter-droplet ice bridging phenomenon that initiates at edge/surface defects and propagates ice across the droplet population via localized vapor pressure gradients [45, 47, 48, 49, 50, 51, 52, 53].

We therefore must retreat once again from the chimera of using superhydrophobicity to

achieve passive anti-icing, at least under humid conditions, and instead focus on enhancing de-icing. For example, by infusing a superhydrophobic substrate with lubricant [54], the ice adhesion strength can be reduced by an order of magnitude compared to an ultra-smooth silicon substrate [55]. Unfortunately, the ice serves to wick the lubricant away from the infused surface over time, so the durability of such an approach seems doubtful [56]. Recent works have shown that soft elastomeric substrates can significantly reduce ice adhesion ($\tau_{\text{ice}} < 10\,\text{kPa}$) with excellent long-term durability [57, 58]. Finally, returning to nanostructured superhydrophobic surfaces, the suspended Cassie state of the frost engenders an order of magnitude decrease in ice adhesion compared to a smooth silicon surface [59]. However, mechanical de-icing in the context of superhydrophobic surfaces seems impractical, as it is established that the iterative fracturing of ice from the surface damages the hydrophobic coating and/or surface roughness over time [35].

Instead of resorting to mechanical de-icing, could the Cassie state of frost on nanostructured superhydrophobic surfaces instead be exploited to enhance thermal de-icing? We recently demonstrated that as a sheet of Cassie frost is melting, it is able to spontaneously dewet into highly mobile Cassie droplets that can easily slide off the surface at small tilt angles [5]. The "dynamic defrosting" of Cassie ice seems quite promising and has encouraged several follow-up studies that confirmed the rapid shedding of the meltwater [6, 7, 8, 60, 61, 62, 63] . However, a direct and systematic comparison of dynamic defrosting on superhydrophobic surfaces versus defrosting on conventional surfaces remains lacking, especially for practical large-area surfaces. Enhanced defrosting on superhydrophobic surfaces has also been reported elsewhere [64, 65, 66, 67, 68], but is not analogous to dynamic defrosting as defined here, as the frost was either not in a robust Cassie state or the surface was oriented horizontally.

Here, we systematically characterize defrosting on a large-area aluminum plate, where half of the plate exhibits a superhydrophobic nanostructure that promotes Cassie frost while the other half is smooth and hydrophobic. We use image processing to directly compare the defrosting rates of the superhydrophobic and hydrophobic surfaces for a variety of frost thicknesses and tilt angles. Provided that the frost is sufficiently thick, we demonstrate that only the Cassie frost on the superhydrophobic surface is able to dynamically shed upon melting, even at very low tilt angles. The dynamic defrosting of Cassie ice therefore significantly enhances the efficiency of thermal de-icing, as only the latent heat of fusion has to be input, while the latent heat of vaporization is instead replaced with gravitational mobilization. Our demonstration of dynamic defrosting on a scalable aluminum surface, rather than a small-area silicon chip,[5] illustrates its potential for use in real-life applications such as airplanes and heat exchangers.

3.2 Experimental Section

3.2.1 Surface Fabrication

An aluminum plate of dimensions 15.24 cm × 15.24 cm × 0.64 cm was degreased by submerging in acetone and subsequently isopropyl alcohol for 10 min each. The plate was then rinsed with deionized water, dried with nitrogen gas, and dehydrated on a 180 °C hot plate for 30 min. After drying, the aluminum plate was deep cleaned for 30 min with oxygen plasma at 600 W (TePla America IoN Wave 10 Plasma System). One half of the plate was then dipped into a water bath heated to 70 °C for 10 min, which imparts an aluminum hydroxide nanostructure (Figure 1a) [69]. After dehydrating and deep cleaning the plate again, it was sealed into a container along with 100μL of trichloro(1H, 1H, 2H, 2H−perfluorooctyl)silane and placed into an oven at 70 °C for 1 hr. This resulted in the vapor-phase deposition of a hydrophobic silane monolayer that conformally coated the entire front face of the hybrid plate.

The half of the plate exhibiting the aluminum hydroxide nanostructure was rendered highly superhydrophobic (SHPB) by the silane coating; this recipe is already well-known to promote jumping-droplet condensation that exhibits a suspended Cassie state [70, 71, 72]. As has been previously established [5, 59], promoting a Cassie state for supercooled condensate simultaneously promotes the formation of Cassie frost upon freezing. In contrast, the half of the aluminum face that was not dipped in hot water was simply smooth and hydrophobic (HPB) after silanization, which allowed for a direct side-by-side comparison of Cassie frost versus conventional frost (Figure 1b). The Cassie wetting state of dew was confirmed by observing jumping-droplet condensation with a Phantom v711 high-speed camera (Figure 1c). Using the shrink-swell method on a goniometer (ramé-hart Model 590), the advancing and receding apparent contact angles of deposited droplets were measured to be $\theta_A/\theta_R = 170°/169°$ on the SHPB surface and $\theta_A/\theta_R = 94°/77°$ on the HPB surface.

3.2.2 Experimental Setup

To grow frost, the aluminum plate was firmly clamped onto the top of a large block of dry ice (Figure 2a). The ambient environment was warm and humid: $T_\infty = 23 \pm 0.5$ °C and RH $= 40 \pm 2$ %, resulting in an ambient vapor pressure of $P_\infty = 1{,}120 \pm 90$ Pa. The average temperature of the aluminum plate when fixed to the dry ice was measured to be $T_p = -70 \pm 7$ °C by bonding a thermocouple to a corner of its top face. This setup therefore facilitates a very low saturation pressure at the substrate ($P_s < 1$ Pa), which allowed for thick frost sheets ($h_f = 5$ mm) to be grown within approximately 10 min. A camera looking at the side of the plate was used to determine the average thickness of frost growing along the edge. Once the frost grew to the desired thickness for a given trial: $h_f = 1$ mm, 3 mm, or 5 mm, the plate was removed from the dry ice and immediately placed on an angled platform

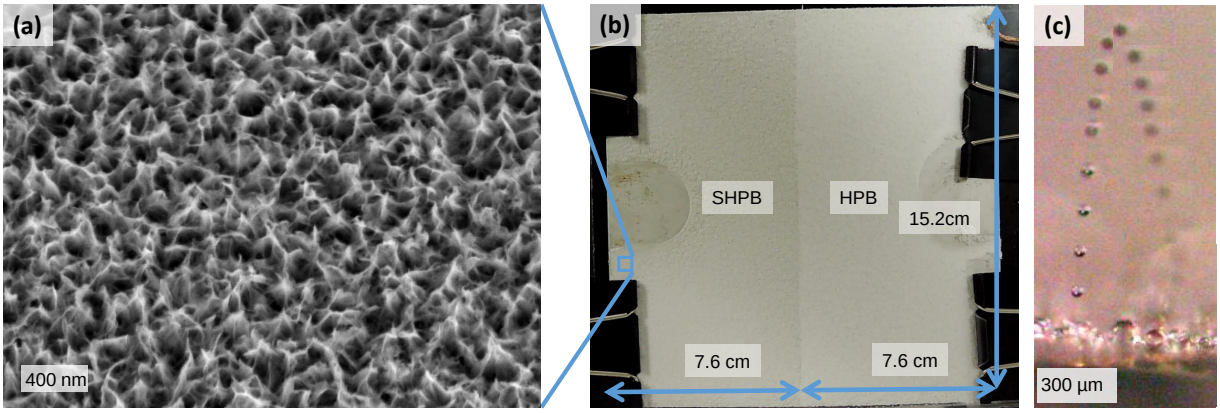

Figure 3.1: (a) Scanning electron micrograph of the superhydrophobic nanostructure. (b) Photograph of frost grown on the hybrid aluminum plate, which facilitated the direct comparison of defrosting on a nanostructured superhydrophobic surface (SHPB, left) versus a smooth hydrophobic surface (HPB, right). The dry circles visible on either side are from clamps used to fix the plate to dry ice during the initial frost growth; these regions were not included in the analysis. (c) Side-view time lapse photography of a dew droplet spontaneously jumping from the SHPB surface upon coalescence, captured over a 42 ms period. The jumping event confirms the suspended Cassie state of the condensation, which is required to subsequently promote Cassie frost upon freezing.

exhibiting a tilt angle of $\alpha = 15°$, 30°, or 90° with respect to the horizontal. One defrosting trial was performed and analyzed for every possible combination of α and h_f. A digital camera was angled to obtain a perfect bird's-eye-view of the aluminum plate and recorded the resulting defrosting behavior (Figure 2b). The camera recorded at 30 fps until the frost had completely melted into pure water droplets and any dynamic behavior had ceased. From that point onward, any meltwater that remained stuck on the substrate was recorded at one frame every 30 s until the droplets completely evaporated.

3.2.3 Image Analysis

Binary masks of the defrosting videos were obtained using a custom Java program that was able to identify the edges of both ice and droplets. The ice recognition method worked by taking the first frame of the melting video, when the surface was completely covered in ice, and comparing it to each frame afterwards. Using a tolerance that decreased over time, the program was able to determine if there was ice on the surface at any given location or time. The edges of liquid droplets were obtained by looking at changes in the RGB values of each pixel with respect to those around it. By combining these methods together, we obtained binary masks that could be analyzed in ImageJ to obtain the projected surface coverage of water/ice on the surface, as well as discern the diameters of fully melted droplets. An area of

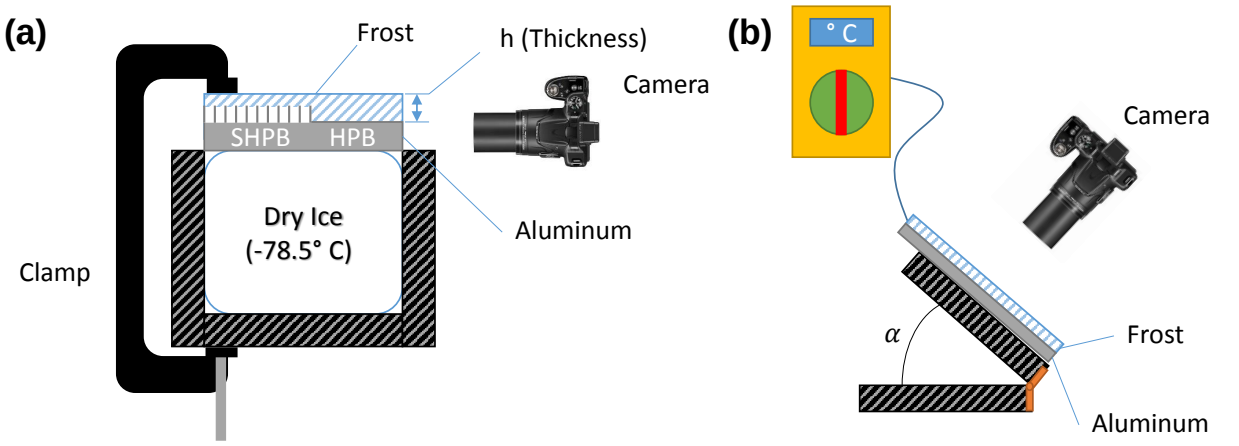

Figure 3.2: (a) Schematic of the experimental setup used to grow frost of thickness h_f on the SHPB (left) and HPB (right) halves of an aluminum plate. (b) After removing the plate from the dry ice, the melting and evaporation of ice and water from the surface at a fixed tilt angle α was captured with a camera.

approximately 3 cm × 13 cm was analyzed in the center of both the SHPB and HPB regions, in order to avoid both boundary effects (between the SHPB/HPB regions) and any damage caused by clamps along the outside perimeter. Specifically, for a given trial there was an edge-to-edge separation of 7 mm between the SHPB and HPB areas to be analyzed, such that any effects the boundary line has on the growth or melting of frost were cropped out. To reduce the time required for the program to run, only a tenth of the images captured during melting were analyzed, resulting in an effective frame rate of 3 fps.

3.3 Results and Discussion

A visual comparison of defrosting on the superhydrophobic (SHPB) versus hydrophobic (HPB) halves of the aluminum surface is provided in Figure 3. Just prior to melting, the frost sheet looked uniform when comparing the SHPB side to the HPB side. This is somewhat surprising, as recent reports have shown that nanostructured superhydrophobic surfaces serve to reduce the packing density of frost sheets compared to smooth hydrophobic surfaces [45, 73]. This discrepancy can be easily resolved by considering the disparate temperatures the frost was grown at. In the previous report, the frost was grown at $T_p = -10\,^{\circ}\mathrm{C}$ or $-20\,^{\circ}\mathrm{C}$, where the in-plane frost growth is governed by inter-droplet ice bridging [45]. In this case, the jumping-droplet effect that is exclusive to the superhydrophobic surface serves to minimize the size of the supercooled droplets, which causes local bridge failure and dryout for roughly 2/3 of the droplets. Therefore, the superhydrophobic surface exhibited a much smaller in-plane footprint of frozen droplets compared to the hydrophobic surface, where nearly every droplet froze successfully. In contrast, here the temperature of the substrate was far colder

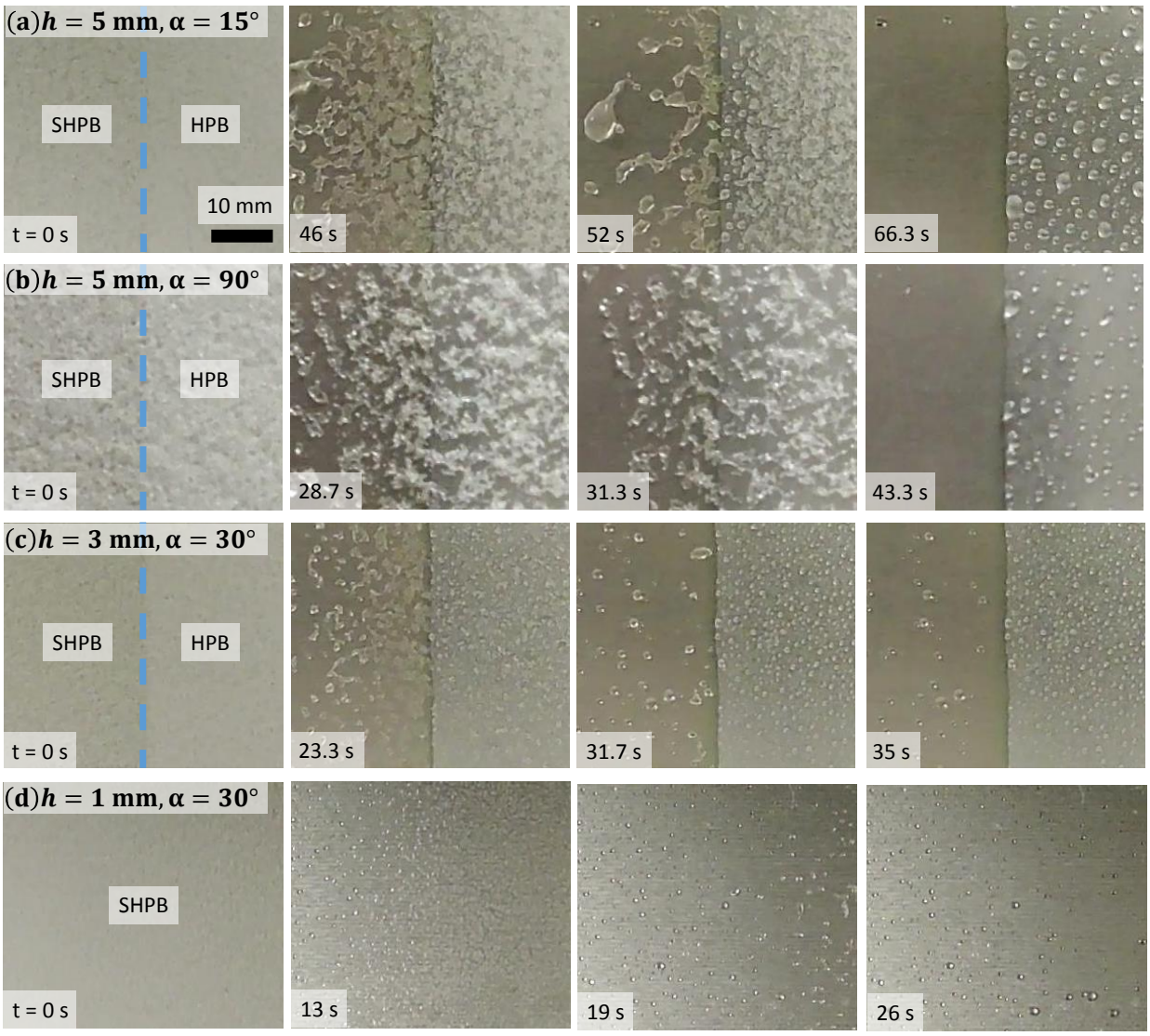

Figure 3.3: Direct visual comparison of defrosting on SHPB versus HPB surfaces. (a,b) For thick frost sheets ($h_f = 5\,\text{mm}$), the defrosting SHPB surface was able to shed nearly 100% of the meltwater from the surface over a wide range of tilt angles: (a) $\alpha = 15°$ and (b) $\alpha = 90°$. In contrast, all of the melted droplets adhered on the HPB side of the aluminum plate. (c) For moderate frost thicknesses ($h_f = 3\,\text{mm}$), the SHPB surface was still uniquely able to shed some of the meltwater, with the extent of shedding depending strongly upon the tilt angle ($\alpha = 30°$ shown here). (d) The dynamic defrosting on the SHPB surface broke down for $h_f = 1\,\text{mm}$ frost, as the droplets were too small to facilitate gravitational shedding. Only the SHPB side is shown here (for $\alpha = 30°$) to better visualize the small droplets. See Movies M1–M7 in the Supporting Information.

($T_p = -70\,^{\circ}\mathrm{C}$), such that the supercooled condensate froze almost immediately at the liquid-solid interface for both the HPB and SHPB surfaces and bypassed the contrasting results induced by inter-droplet ice bridging.

As the frost melted into liquid water, only the SHPB surface promoted the gravitational shedding of droplets from the surface. Given the gravitational removal mechanism of meltwater droplets, it is surprising to note that the amount of dynamic defrosting possible depended more strongly on the initial frost thickness (h_f) than the tilt angle (α). For example, both the $\alpha = 15^{\circ}$ and 90° trials shed virtually all of the meltwater from the SHPB surface for $h_f = 5\,\mathrm{mm}$ frost sheets (Figure 3a,b). The only major difference would appear to be the time scale: droplet shedding for $\alpha = 90^{\circ}$ was about 33% faster than with $\alpha = 15^{\circ}$. When reducing the frost thickness to $h_f = 3\,\mathrm{mm}$, smaller droplets remained pinned (Figure 3c) and the tilt angle was more important, as will be discussed in more detail later in the manuscript. Finally, for very thin frost sheets ($h_f = 1\,\mathrm{mm}$), nearly all of the meltwater droplets were too small for even the SHPB surface to shed, regardless of the tilt angle (Figure 3d). These findings clearly demonstrate that dynamic defrosting on a nanostructured superhydrophobic surface is the most efficient way to thermally remove ice and meltwater, but only for sufficiently thick frost layers.

A more quantitative comparison of the defrosting dynamics is provided in Figure 4, where image analysis provided the projected surface coverage of ice/water on the SHPB versus HPB surfaces over time. Due to challenges inherent to imaging small droplets over a large surface area, only defrosting of $h_f = 3\,\mathrm{mm}$ and 5 mm frost sheets were able to be converted into accurate binary masks for analysis. For the HPB surface, where all meltwater adhered to the substrate, the decrease in surface coverage over time strictly corresponds to the dewetting of the continuous frost sheet into discrete droplets upon melting. After melting was complete but prior to evaporation, the surface coverage of the droplets was $15 \pm 10\%$ on the HPB surface, with the uncertainty likely due to random variations in how the ice melts/dewets along with minor imperfections in the image analysis. For the SHPB surface, the surface coverage decreased not only from dewetting, but additionally from the gravitational shedding of melting droplets from the surface. This resulted in lower surface coverages of $< 10\%$ for $h_f = 3\,\mathrm{mm}$ frost at low tilt angles and $< 5\%$ for $h_f = 3\,\mathrm{mm}$ frost at $\alpha = 90^{\circ}$ or $h_f = 5\,\mathrm{mm}$ frost for all tilt angles tested. For the case of the $h_f = 5\,\mathrm{mm}$ frost, the hysteresis of ice/water on the SHPB surface was so low that it even accelerated the rate of dewetting during melting compared to the HPB surface.

The liquid mass remaining adhered to the SHPB versus HPB surfaces after melting (but prior to evaporation) was also estimated, as shown in Figure 5. Calculations of liquid mass were obtained by measuring the radius of curvature (R) of each static meltwater droplet after the frost had completely melted. The volume of each droplet can then be calculated from the relation $V = (\pi/3)R^3(2 - 3\cos\theta_R + \cos^3\theta_R)$, using $\theta_R = 169^{\circ}$ for dewetted meltwater on the SHPB surface and $\theta_R = 77^{\circ}$ for the HPB surface. The initial masses per area of the 3 mm and 5 mm thick frost sheets were assumed to be equal to the averaged mass per area of meltwater in the HPB region for all trials where no droplets were able to shed.

In contrast to the surface coverage plots in Figure 4, where dewetting versus shedding effects are hard to disentangle, the mass measurements in Figure 5 serve to isolate shedding events. When $h_f = 3\,\text{mm}$, the amount of melting frost removed from the SHPB surface depended strongly on the tilt angle. For example, less than 10% of the melting frost was able to shed when $\alpha = 15°$ compared to removing about two-thirds of all water when $\alpha = 90°$. For $h_f = 5\,\text{mm}$, the tilt angle was much less important. The SHPB surface was able to remove about 90% of the melting frost for tilt angles of 15° and 30°, compared to a slight improvement to 95% removal for $\alpha = 90°$. For all cases with the HPB surfaces, virtually all of the meltwater remained adhered, such that the calculations of liquid mass remaining on the surface varied from 80 – 120% which simply represents the uncertainty inherent to our indirect calculations of mass.

The mobilization versus pinning of meltwater on the surface can be understood as a competition between forces caused by gravity and contact angle hysteresis [74]:

$$F^* = \frac{\rho V g \sin\alpha}{\pi a \gamma (\cos\theta_R - \cos\theta_A)}, \tag{3.1}$$

where droplet shedding is possible when $F^* > 1$. Note that V is a droplet's volume, g is gravity, a is a droplet's contact radius, γ is surface tension, and θ_R and θ_A are the receding and advancing apparent contact angles. Note that both V and a for each droplet were calculated from the measured radius of curvature R and the average apparent contact angle: $\theta \approx (\theta_A + \theta_R)/2$. Specifically, $V = (\pi/3)R^3(2 - 3\cos\theta + \cos^3\theta)$ and $a = R\sin\theta$. Note that the values of θ_R and θ_A of the HPB and SHPB surfaces were assumed to correspond to those measured using deposited droplets on a goniometer. Of course, for SHPB surfaces it is never certain that the wetting state and hysteresis of condensed droplets will correspond to that of deposited droplets, but our assumption seems reasonable here given the established Casie state of the condensed water/ice.

	Superhydrophobic				**Hydrophobic**			
	$h_f = 3\,\text{mm}$		$h_f = 5\,\text{mm}$		$h_f = 3\,\text{mm}$		$h_f = 5\,\text{mm}$	
	D(mm)	**F***	**D(mm)**	**F***	**D(mm)**	**F***	**D(mm)**	**F***
$\alpha = 15°$	1.74	1.24	1.84	1.39	(0.85)	(0.03)	(2.90)	(0.32)
$\alpha = 30°$	1.24	1.22	1.36	1.47	(1.20)	(0.11)	7.04	3.63
$\alpha = 90°$	1.24	2.44	2.65	11.13	(1.02)	(0.15)	(2.04)	(0.61)

Table 3.1: The diameter (D) and ratio of gravity versus hysteresis forces (F^*) of meltwater droplets on the SHPB and HPB surfaces. For trials where the meltwater was able to slide down the surface ($F^* > 1$), values correspond to the smallest droplet able to mobilize. For trials where all meltwater droplets adhered to the surface ($F^* < 1$), the values are now in parenthesis and represent the largest droplet.

If Eq. 3.1 is accurate, it follows that the critical (minimum) droplet size required for dynamic defrosting, $D_c = 2R_c$, should correspond to $F_c^* \approx 1$. Values of D_c were obtained by reviewing

the videos of dynamic defrosting to measure the diameter of the smallest droplet that was able to successfully mobilize from the surface for each trial (Figure 6). For $\alpha = 15°$ and $\alpha = 30°$, the measured values of D_c on the SHPB surface corresponded to $F^* = 1$–1.5 in all cases (Table 1). This confirms that the hysteresis of a SHPB meltwater droplet is, at worst, only slightly higher than for a droplet deposited onto an equivalently dry surface. This is rationalized by the fact that jumping-droplet condensation is not actually in a perfect Cassie state, but instead, typically begins impaled inside of a unit cell(s) of nanoroughness and only expands into a Cassie state as the droplet grows [39, 40, 41]. Much larger values of F^* were calculated for the SHPB surface when $\alpha = 90°$, but this is simply because *all* droplets were able to shed at this large tilt angle, such that even the smallest mobilized droplet exceeded the critical size ($D > D_c$).

For the HPB surface, where meltwater droplets were always pinned, it was confirmed that $F^* < 1$ even for the largest droplets (Table 1). The dramatically smaller values of F^* for the HPB surface compared to the SHPB surface, despite the melted droplets being similarly millimetric in size, is due to the unusually small hysteresis ($\theta_A - \theta_R \sim 1°$) inherent to the Cassie-state droplets on the SHPB surface. For the one case where a single droplet was able to slide down the HPB surface ($h_f = 5\,\text{mm}$ and $\alpha = 30°$), we note that the melting droplet was unusually large ($D \approx 7\,\text{mm}$) which results in $F^* > 1$ as expected. While the large frost thickness ($h_f = 5\,\text{mm}$) was certainly crucial for producing a large enough droplet to shed on the HPB surface, we expect that it was mere chance that it occurred for the $\alpha = 30°$ trial rather than the other tilt angles. The variance of the maximum meltwater droplet size for a given value of h_f is likely due to the complexity inherent to the growth and subsequent melting of dendritic frost sheets. For the case of thin frost sheets ($h_f = 1\,\text{mm}$), the droplets were microscopic in size, such that $F^* < 1$ for both the HPB and SHPB surfaces.

Immediately after all ice melting and droplet shedding was completed for a given trial, the evaporation of the adhered droplets remaining on the surface was analyzed. For each trial, both the surface coverage and mass of droplets on the HPB surface were roughly an order of magnitude larger compared to the corresponding SHPB surface (cf. Figures 4 and 5). As a result, in most trials it took droplets on the HPB surface approximately 1,000 s longer to completely evaporate ($< 0.5\%$ coverage) compared to the SHPB surface. For the 5 mm frost, the initial coverage of adhered droplets was already $< 1\%$ after only 60 s of melting, such that there was no appreciable need to evaporate meltwater at all! This illustrates the unique advantage of dynamic defrosting: to completely dry a frosted surface, the thermal input only needs to satisfy the latent heat of fusion, while the latent heat of vaporization is completely replaced by passive droplet shedding.

Assuming a sufficiently thick frost layer ($h_f \geq 3\,\text{mm}$) to promote robust dynamic defrosting (negligible adhered meltwater), the savings in energy versus conventional defrosting can be quantified. From our previous report, molecular dynamics simulations revealed that melting Cassie frost can readily flow (i.e. dewet and shed) when it is approximately 90% liquid [5]. Therefore, when Cassie frost is 90% melted, the meltwater will shed leaving the surface effectively dry. Assuming a heat input of constant power per unit area ($\dot{q}$) and a

frost sheet of known mass per unit area (m_{frost}), the time required to dynamically defrost a superhydrophobic substrate is given by:

$$t_{SHPB} \approx \frac{(0.9 m_{\text{frost}}) L_f}{\dot{q}}, \tag{3.2}$$

where $L_f = 334\,\text{kJ/kg}$ is the latent heat of fusion of water at 0 °C. Conversely, since virtually all meltwater remains adhered to hydrophobic surfaces, the ice must fully melt *and* evaporate to dry the surface:

$$t_{HPB} \approx \frac{m_{\text{frost}}(L_f + L_v)}{\dot{q}}, \tag{3.3}$$

where $L_v = 2{,}446\,\text{kJ/kg}$ is the latent heat of vaporization of water at room temperature. Assuming identical heat inputs and frost sheets, the ratio in defrosting times is given by $t_{SHPB}/t_{HPB} \approx (0.9L_f)/(L_f + L_v) \approx 0.11$. This analysis reveals that dynamic defrosting is about 9.2 times faster than conventional defrosting with regards to drying a frosted surface, almost exactly an order of magnitude enhancement (in good agreement with Figure 4). If time were held constant instead of heat, it similarly follows that a superhydrophobic surface would require 9.2 times less heat input compared to conventional surfaces to dry the frosted surface.

Finally, we attempted one trial where $h_f = 3\,\text{mm}$ of frost was flipped completely over during defrosting, such that $\alpha = 180°$ (Figure 7). Instead of a bird's-eye-view, we employed an isometric camera angle for this one case. Interestingly, before the frost had even melted fully enough to produce liquid-like droplets, it was observed to "fall" off the SHPB side as a continuous sheet. Furthermore, this dynamic peeling extended across the border to the HPB side, until nearly all of the melting frost was removed in less than 1 s of total time.

Since the frost had to partially melt before it initially detached from the SHPB side, let's approximate the melting film as liquid-like in composition. Detachment of melting frost from an upside-down surface is therefore a direct competition between gravitational energy and the work of adhesion:

$$E^* = \frac{h_f^2 \rho_{\text{frost}} g}{\phi\gamma(1 + \cos\theta_Y)}, \tag{3.4}$$

where h_f and ρ_{frost} are the height and effective density of the frost sheet prior to melting, ϕ is the solid fraction of the surface, and θ_Y is the Young's contact angle of a droplet on an equivalently smooth surface. Note that both the gravitational energy and work of adhesion contain a surface area term, which cancel out in Eq. 3.4.

The mass per area of the frost sheet prior to melting was estimated from the measurements discussed in Figure 5. Using a reference point of ($h_f = 0\,\text{m}$, $m_{\text{frost}} = 0\,\text{kg/m}^2$) and the two existing points calculated earlier, ($h_f = 0.003\,\text{m}$, $m_{\text{frost}} = 0.170\,\text{kg/m}^2$) and ($h_f = 0.005\,\text{m}$, $m_{\text{frost}} = 0.436\,\text{kg/m}^2$), a quadratic relationship was solved for giving the mass per area of the frost as a function of the frost thickness:

$$m_{\text{frost}} = f(h_f) = 15270 h_f^2 + 10.81 h_f, \tag{3.5}$$

where m_{frost} is equivalent to $\rho_{\text{frost}} h_f$ so that the relationship can be substituted into Eq. 3.4:

$$E^* = \frac{(15269h_f^3 + 10.812h_f^2)g}{\phi\gamma(1+\cos\theta_Y)}. \tag{3.6}$$

Conveniently, our wettability measurements of the smooth HPB side provide the Young's angle: $\theta_Y \approx \theta_A \approx 94°$. Finally, the solid fraction of the SHPB surface can be calculated by plugging the Young's angle and apparent contact angle ($\theta \approx 170°$) into the Cassie equation [17]:

$$\phi = \frac{1+\cos\theta}{(1+\cos\theta_Y)}, \tag{3.7}$$

which yields $\phi = 0.016$. For the smooth HPB surface, $\phi = 1$, which is the only parameter in Eq. 3.6 that is different compared to the SHPB surface.

The critical thickness required for a frost sheet to detach from an upside-down surface upon partial melting can be estimated by setting $E_c^* = 1$ in Eq. 3.6 and solving for h_c. For our SHPB/HPB hybrid surface, we calculate $h_{c,\text{SHPB}} = 1.8\,\text{mm}$ and $h_{c,\text{HPB}} = 7.2\,\text{mm}$, respectively. This explains why the melting frost was initially only able to detach from the SHPB side of the surface, as $h_{c,\text{SHPB}} < h_f < h_{c,\text{HPB}}$. As the melting frost on the SHPB side detached, it was observed to pull down on the inter-connected ice/water still adhered to the HPB side, which serves to dramatically increase the gravitational term in Eq. 3.6. Conservatively, we can imagine that the entire weight of the hinged SHPB ice/water is weighing down an equivalent surface area of ice/water still adhered to the HPB side, such that the numerator of Eq. 3.6 is doubled. This results in a new critical thickness of $h_{c,\text{HPB}} \approx 5.7\,\text{mm}$ that is now exceeded by the $h_f \approx 6\,\text{mm}$ effective thickness of the dual frost sheets weighing down the HPB region. In reality, it is likely that the hinging SHPB frost will only be weighing down a localized region of the HPB frost, concentrating the gravitational force over a much smaller area which would decrease the value of $h_{c,\text{HPB}}$ well beneath our conservative estimate. This is well evidenced by Figure 7, where the melting HPB frost is initially adhered but easily falls off within the region adjacent to the hinging frost.

Considering that dynamic defrosting is only optimal for sufficiently thick frost sheets, we suggest that heat pumps are perhaps the most promising application for this surface technology. This is because the thermal defrosting of the outdoor components of a heat pump is programmable, such that the unit can wait until the frost is thick enough before initiating a defrost cycle [75, 76]. Finally, we suggest some future directions for research on dynamic defrosting. It is already established that mechanical de-icing serves to rapidly degrade the quality of a SHPB surface [35], but whether a SHPB surface breaks down under repeated dynamic defrosting events is still an open question. So far, it has only been shown that there is no apparent damage to a nanostructured SHPB surface after 10 cycles of frosting/defrosting [5], future studies could probe the breakdown limit to determine the practicality of superhydrophobic defrosters. We have focused here on the macroscopic aspects of dynamic defrosting; however, future studies could examine in more detail a recent discovery that meltwater mobilization also occurs on a microscopic scale due to coalescence-induced jumping

[63]. Our discovery of the frost peeling off the upside-down surface, while interesting, was not systematic and could hopefully inspire more detailed follow-up studies. Finally, it has been briefly demonstrated that dynamic defrosting also occurs on slippery liquid-infused porous surfaces (SLIPS) [44, 77], as SLIPS surfaces also exhibit minimal contact angle hysteresis [54]. Putting aside the durability issues of oil/ice systems due to wicking [78**?**], it would be interesting to contrast the physics of dynamic defrosting on SHPB versus SLIPS surfaces.

3.4 Conclusion

In conclusion, we demonstrated that nanostructured superhydrophobic surfaces are uniquely able to shed the majority of melting frost from the surface by gravity, but only for frost sheets that are sufficiently thick: $h_f \geq 3\,\text{mm}$ for $\alpha \approx 90°$ or $h_f \geq 5\,\text{mm}$ for $\alpha \approx 15°$. The enabling mechanism is the suspended Cassie state of the supercooled condensation and frost that form on the superhydrophobic surface, which promotes a minimal contact angle hysteresis that allows even small meltwater droplets ($D \approx 1\,\text{mm}$) to slide off the surface at low tilt angles ($\alpha \leq 15°$). In contrast, virtually all meltwater on smooth hydrophobic surfaces remains completely adhered to the surface, even at large tilt angles, and has to be slowly evaporated to dry the surface. Finally, we observed that when utilizing an upside-down orientation, the entire sheet of melting frost on the superhydrophobic surface was able to rapidly detach and could even pull off frost still adhered to the neighboring hydrophobic region. These so-called "dynamic defrosting" phenomena on the superhydrophobic surface are attractive because the input of thermal energy only needs to overcome the latent heat of fusion, while completely bypassing the latent heat of vaporization which requires an order of magnitude more thermal energy and time.

3.5 Supporting Information

Nine movies representative of Figures 3, 4, and 6 are available in the Supporting Information. This material is available free of charge via the internet at http://pubs.acs.org.

3.6 Acknowledgements

The surface fabrication and defrosting experiments were conducted at the Center for Nanophase Materials Sciences, which is a DOE Office of Science User Facility. We are thankful to A.Lynn Abbott for helpful discussions regarding the image analysis. K.R.M. and J.B.B. acknowledge startup funds from the Department of Biomedical Engineering and Mechanics at Virginia Tech.

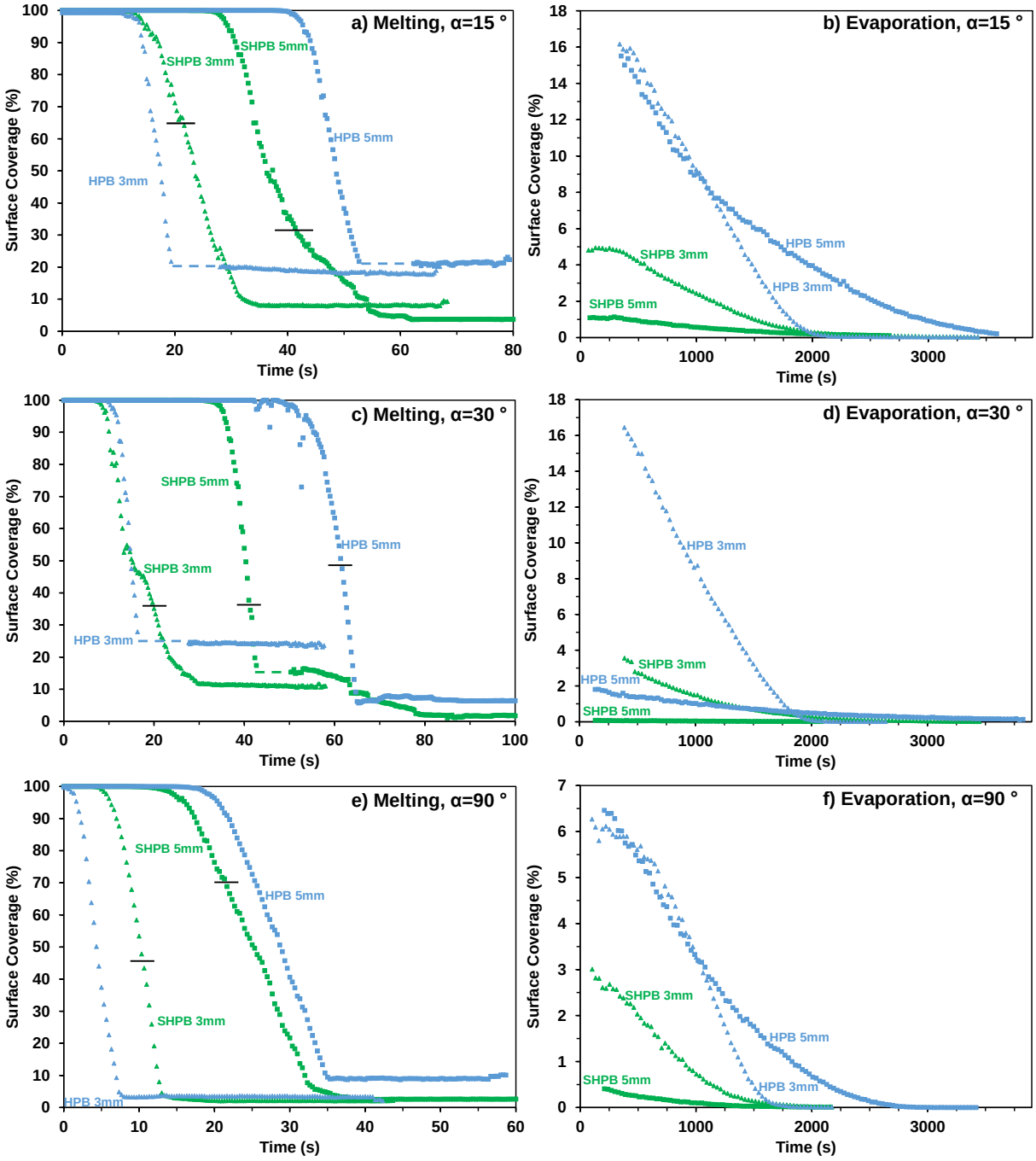

Figure 3.4: Projected surface coverage of ice/water with respect to time during the melting of a frost sheet and the subsequent evaporation of the adhered meltwater. Time zero corresponds to the onset of observable melting of a frost sheet. The short horizontal black lines correspond to the onset of the meltwater dynamically shedding, which is exclusive to the SHPB surfaces. The tilt angle of the defrosting surface is (a,b) $\alpha = 15°$, (c,d) $\alpha = 30°$, and (e,f) $\alpha = 90°$. See Movie M8 in the Supporting Information as an example of the image analysis.

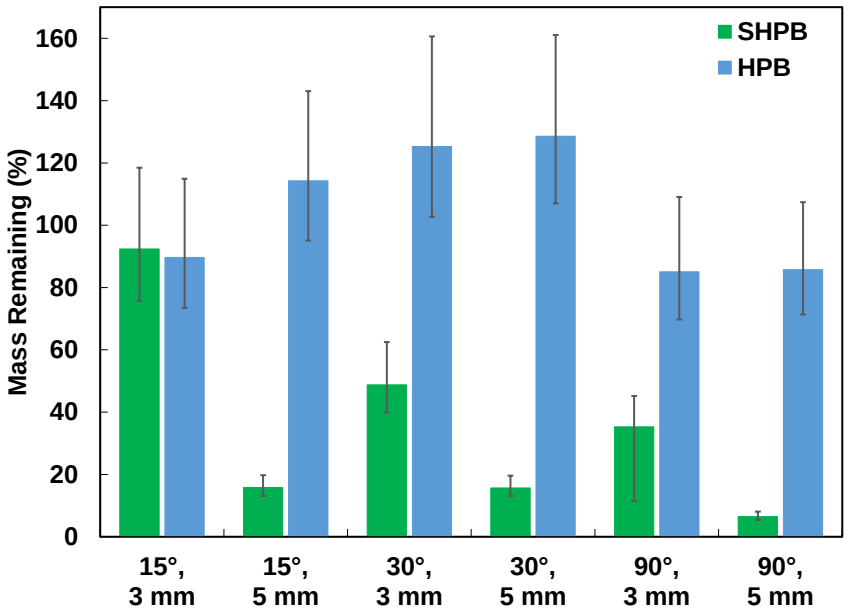

Figure 3.5: Estimated percentage of the mass of water remaining on SHPB (green) and HPB (blue) surfaces after the frost has melted, as a function of the tilt angle and initial frost thickness. The value of the frost mass prior to defrosting for a given value of h_f was found by averaging the total mass of the adhered liquid on the HPB regions for each trial where no shedding occurred. Error bars represent plus and minus a standard deviation from the averaged value of the initial ice mass.

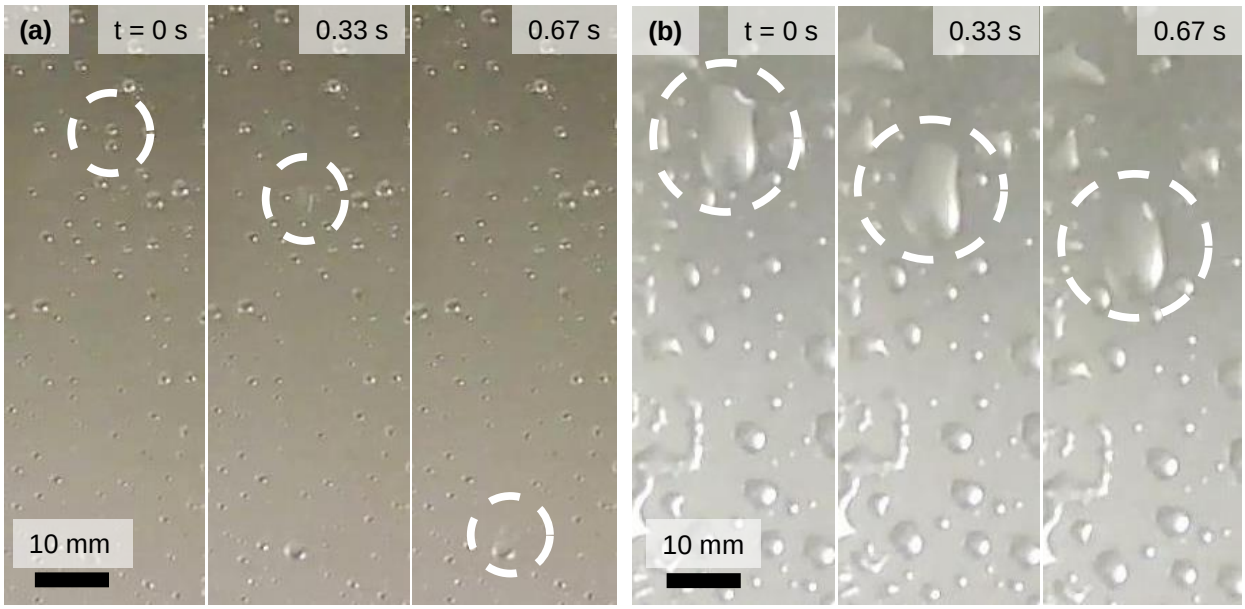

Figure 3.6: Meltwater droplets sliding down the (a) SHPB and (b) HPB surfaces. The low hysteresis of Cassie frost on the SHPB surface served to decrease the critical size of shedding condensate ($D_c \approx 1\,\text{mm}$) relative to the HPB surface ($D_c \approx 10\,\text{mm}$) by an order of magnitude. The experimental conditions were $\alpha = 15°$ and $h_f = 3\,\text{mm}$ for (a) and $\alpha = 30°$ and $h_f = 5\,\text{mm}$ for (b).

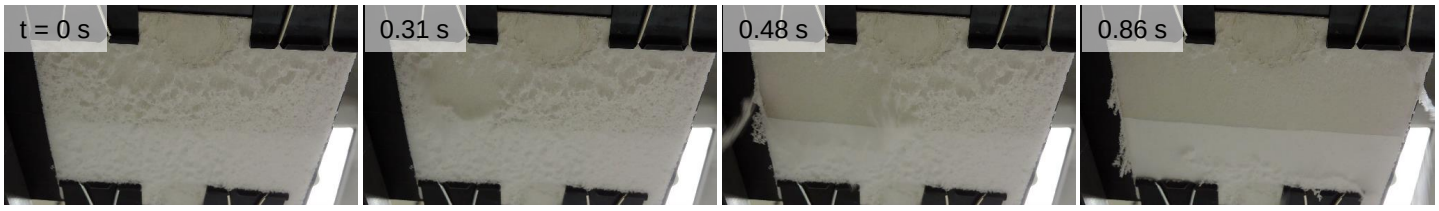

Figure 3.7: During defrosting on an upside-down surface, the melting frost was able to rapidly detach from the SHPB side (top half of image), subsequently peeling off the HPB frost (bottom half) in a chain reaction. See Movie M9 in the Supporting Information.

Chapter 4

Porous Bridging

4.1 Introduction

The physical transfer of droplets from one solid substrate to an opposing one has been investigated extensively over the past decade. Droplet transfer is typically achieved by lowering the upper substrate onto the top of the droplet to form a bridge and subsequently raising the upper substrate. In some cases, the upper substrate is slowly raised to stretch the bridge quasi-statically [3], whereas in other cases the liquid bridge is stretched with an appreciable inertial force [79, 80]. If the wettabilities of the substrates are the same, droplet transfer is limited to about 50% of the droplet's volume [81]. The extent of droplet transfer can be enhanced by, or limited by, the wettability difference between the two surfaces, with the portion of the droplet transferred increasing as the wettability difference increases [81]. The magnitude of each substrate's contact angle hysteresis governs where contact line pinning occurs, which also affects the transfer process [82]. In an extreme case of a droplet transferring from a nanostructured superhydrophobic substrate to a hydrophilic substrate, nearly the entire droplet volume could transfer without any need to move the substrates [83].

The ability to transfer a droplet without any relative motion between the substrates is attractive in its simplicity, but raises the question of how to initiate the transfer in the first place. [83] solved this issue in two different ways. For dispensed droplets, the upper substrate was slowly lowered until it gently contacted the target droplet, at which point the transfer process itself was purely a function of the surface wettabilities. To avoid the motion of the parallel substrates entirely, they bonded one substrate to a cold plate, such that dew droplets nucleated and grew until they could touch the opposing surface. The condensation approach was utilized in bridging-droplet vapor chambers by [84] and [85], where a wicked evaporator was placed opposite a smooth hydrophobic condenser. This asymmetry in surface wettability enabled one-way heat transfer, i.e., a thermal diode. In the forward mode of operation, continuous phase-change heat transfer was facilitated by the bridging-droplet return of dropwise condensate to the opposing wicked evaporator. The heat source was switched to the hydrophobic surface in the reverse mode, such that condensation is now trapped inside the opposing wick resulting in an insulating vapor gap. In contrast to the existing studies on the physics of droplet transfer, the receiving surface for the bridging-droplet thermal diode was porous instead of solid. This will fundamentally alter the hydrodynamics of the bridging-droplet transfer process, which to date has not been explored and could be used to

further optimize the design.

Here, we study bridging-droplet transfer from a solid substrate to an opposing porous ceramic surface. By virtue of the receiving surface being porous rather than solid, droplet transfer could occur spontaneously with no relative movement of the surfaces required. Systematically varying the substrate wettability, receiving pore size, and droplet volume and working fluid, we characterize the various wetting and wicking phenomena that comprise the droplet transfer process. During the initial wetting of the receiving surface, we identify a crossover from donor-independent behavior to a donor-dependent regime, where the receding viscous wedge at the donor substrate becomes rate-limiting. This is followed by a much longer wicking regime, where the liquid bridge slowly recedes along both surfaces and the wicking rate follows Darcy's law.

4.2 Materials and Methods

The wettability of the solid substrate was varied as either hydrophilic, hydrophobic, or superhydrophobic. An untreated silicon wafer with 100 nm of SiO_2 (WRS Materials, P2742753) was used as the hydrophilic substrate. Prior to use, the wafers were cleaned by submerging in acetone, isopropyl alcohol, and water, followed by drying and 4 min in a plasma cleaner (Plasma Etch Inc., PE-25). The hydrophobic substrate was a silicon wafer that was cleaned in the same manner followed by vapor-phase silanization. This was done by placing the wafer in a petri dish alongside an open vial of 25 μL of trichloro(1H,1H,2H,2H-perfluorooctyl)silane (Sigma Aldrich) on a hot plate set to 70 ° C for 6 h. The superhydrophobic surface was created by thermally dewetting a platinum film on a silicon wafer, creating a non-lithographic etch mask that resulted in nanopillars after dry etching [5, 86]. The nanopillars were then rendered superhydrophobic using the same silane treatment as the hydrophobic surface. The advancing and receding contact angles of the surfaces were measured using the shrink-swell method on a goniometer, with the average of ten measurements being shown in table 4.1. The porous ceramic surfaces were commercially available and exhibited an average nanopore radius of either $r_p \approx 80$ nm (SoilMoisture, 0604D01.5-B15M1) or $r_p \approx 800$ nm (SoilMoisture, 0604D01.5-B01M1). As specified by the manufacturer, the porous ceramics exhibited $\phi \approx 0.33$ for both pore sizes. The advancing and receding contact angles of droplets on the porous disk were not measurable due to the dynamic wicking into the nanopores.

Side-view imaging that summarizes the experimental setup is shown in figure 4.1. A liquid droplet was manually deposited on one of the solid substrates. The droplet volume was varied as either $V = 0.5\,\mu$L or 5 μL, while the choice of working fluid was either distilled water, ethanol, or 100 cSt silicone oil (table 4.2). Three trials were performed using water droplets for each combination of donor substrate wettability, droplet volume, and receiving pore radius. Fixing the donor substrate to the hydrophobic wettability, three trials were performed for each combination of working fluid, droplet volume, and receiving pore radius.

Table 4.1: Contact angle, advancing contact angle, receding contact angle, and contact angle hysteresis of water on the three surfaces used in our experiments. The errors are plus/minus one standard deviation of the measurements.

Surface	θ_{A}	θ_R	θ_{A} - θ_{R}
HPL	$78.6° \pm 0.8°$	$42° \pm 3°$	≈35°
HPB	$119.1° \pm 0.9°$	$88° \pm 1°$	≈30°
SHPB	$162.1° \pm 0.8°$	$152.7° \pm 0.7°$	≈10°

Table 4.2: Physical characteristics of the liquids used in our experiments.

Liquid	ρ (kg/m^3)	μ (mPa·s)	γ (N/m)
Water	1000	1.8	0.072
Ethanol	789	1.2	0.021
100 cSt Silicon Oil	960	96	0.020

After the droplet was deposited, an overlying porous ceramic disk was slowly lowered using a linear manual translation stage. The velocity of the disk can be estimated from the high-speed videos and, while not inherently controlled, was significantly slower than any wetting and was stopped after wetting started. The disk was lowered until it touched the top of a droplet of height h (figure 4.1a). The disk was stopped as soon as it was observed to touch the droplet. Slowly lowering the roof can be considered analogous to the real-life scenario of a vapor chamber [84], where the dew droplets would continually grow until touching the static roof. The speed at which the porous disk was lowered was orders of magnitude slower than the resulting bridging hydrodynamics, which was captured using side-view high speed imaging (Phantom v711). The primary benchmarks captured by the camera were the evolution of the donor contact radius (r_{d}), donor contact angle (θ_{d}), receiving contact radius (r_{r}), and receiving contact angle (θ_{r}). To ensure consistency, the porous disk was laterally repositioned between trials to ensure the pores above the bridging droplet were initially dry. As will be shown later, the wicking behavior can be assumed to be one-dimensional, resulting in the wetted area of the porous media for each trial being approximately the same as the footprint of each droplet. The porous disk was repositioned so that each trial would have a full droplet diameter separating its part of the disk from any other trials.Wetted porous media were outside the scope of this work. The humidity was not controlled, as the water and surfaces were the same temperature as the room and the evaporation of the droplet would take significantly longer than the absorption for ambient conditions. The bridging hydrodynamics of the deposited droplets are expected to be equivalent to condensed droplets for the hydrophilic and hydrophobic substrates. For the nanostructured superhydrophobic substrate, dew droplets are known to inflate in an imperfect Cassie state [40], such that they would exhibit a slightly larger contact angle hysteresis compared to the deposited droplets used here.

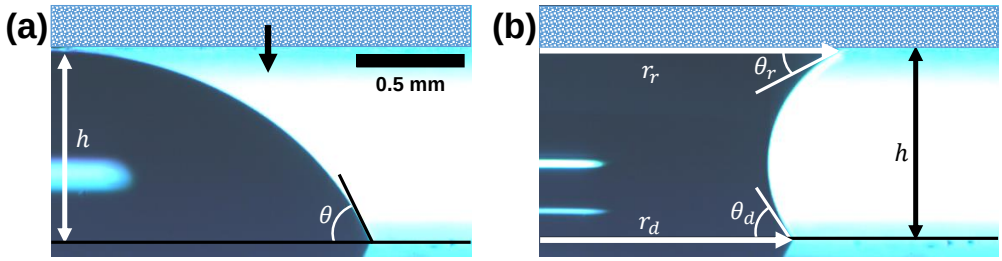

Figure 4.1: (a) Side-view photograph of a sessile droplet with a static contact angle θ, just prior to bridging into an overlying porous surface. The porous roof, false-colored to enhance visibility, was slowly lowered until the gap height (h) matched the height of the droplet. (b) During the bridging process, relevant parameters include the contact radii for the donor and receiving surfaces, r_d and r_r respectively, the contact angles for the donor and receiving surfaces, θ_d and θ_r respectively, and the height of the gap, h, which is fixed during the bridging process and equal to the height of the droplet before bridging.

4.3 Visualization of Droplet Bridging

In the first set of experiments, the high-speed camera was set to a relatively slower capture rate in order to film the entire bridging-droplet process. These videos showed that the bridging can be divided into an initial wetting regime and a subsequent wicking regime (Figures 4.2 and 4.3). During the wetting regime, the top of the droplet touches the receiving porous surface to grow an additional contact line, while the donor contact line recedes. The wetting regime begins at first contact with the receiving surface and ends when the droplet has reached a new equilibrium shape. During the wicking regime, the droplet's volume transfers to the inside of the porous receiving surface, aside from the pinched-off droplet that remains on the donor surface. The wicking regime begins at the end of the wetting regime and ends when all of the liquid on the receiving surface has been sucked into the wick.

Figure 4.2a shows a droplet bridging from a hydrophilic silicon substrate to a porous ceramic surface with an effective pore radius of 800 nm. The first row of images depicts the wetting regime, which culminates in a fairly symmetric liquid bridge due to the similar contact angles of both surfaces. The second row of images shows the wicking regime, where the liquid bridge gradually recedes along both surfaces as the water is sucked into the wick. Eventually, the quasi-steady bridge shape becomes unstable, where the neck radius rapidly decays and then splits into two droplets, one on each surface. Upon becoming unstable, the bridge took about ~ 1 ms to pinch-off, which is comparable to the capillary-inertial time scale as has been previously reported [87]. The upper droplet then continues to wick inside of the porous ceramic, exhibiting a constant contact diameter throughout, until it is entirely absorbed. The lower droplet survives indefinitely in the absence of evaporation. There is a vast disparity in time scales between the two regimes, for example here the wetting regime

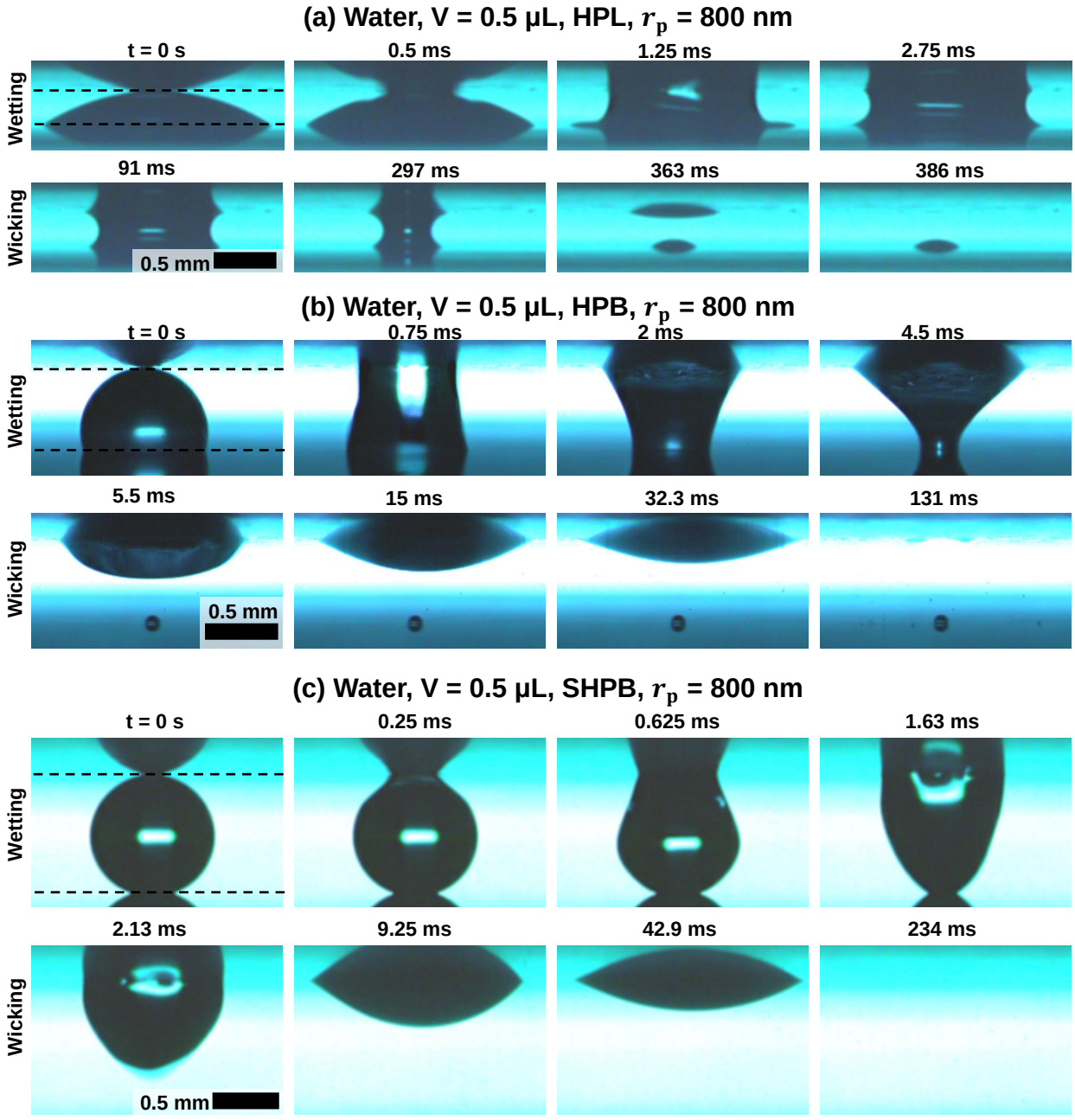

Figure 4.2: High-speed imaging of the bridging process for water droplets, where the donor substrate was (a) hydrophilic (HPL), (b) hydrophobic (HPB), or (c) superhydrophobic (SHPB). The first row of each trial depicts the wetting regime, while the second row shows the subsequent wicking regime. See Movies 1 and 2 in the Supporting Information.

lasted $t_{\text{wet}} \sim 1\,\text{ms}$ while the wicking regime lasted $t_{\text{wick}} \sim 100\,\text{ms}$.

When switching the donor substrate to smooth hydrophobic silicon, shown in figure 4.2b, the wetting and wicking regimes were still observed but with some important differences. During wetting, the liquid bridge shape was no longer symmetric, as the receiving contact diameter was much larger than the hydrophobic donor one. This, in turn, resulted in the immediate pinch-off of the liquid bridge as the wetting regime switched to the wicking regime. Consequently, the entire wicking regime was comprised of pumping water from a constant-diameter droplet, as opposed to the previous case where the liquid bridge persisted for the majority of the wicking. Finally, when using a superhydrophobic donor substrate in figure 4.2c, the entire droplet was able to dewet and transfer to the ceramic during the wetting regime. In other words, there was no pinch-off event at all, such that 100% of the initial droplet was able to absorb into the ceramic during the wicking regime.

While figure 4.2a varied the wettability exclusively, figure 4.3 varies the working fluid, droplet volume, and the pore size of the receiving surface. In figure 4.3a, an ethanol droplet was used in place of a water droplet to decrease the surface tension by a factor of about 3.5. This resulted in longer time scales for both the wetting and wicking regimes, as evidenced by the time stamps. Otherwise, the bridging and pinch-off hydrodynamics were qualitatively consistent to that of the water droplet. When switching the working fluid once again to silicone oil (figure 4.3b), the viscosity is increased by nearly two orders of magnitude compared to water or ethanol (while the surface tension is comparable to ethanol). As a consequence, the duration of the wetting regime increased by about two orders of magnitude to $t_{\text{wet}} \sim 100\,\text{ms}$, while the wicking regime increased by four orders of magnitude to $t_{\text{wick}} \sim 1{,}000\,\text{s}$. Returning to a water droplet, figure 4.3c used a $5\,\mu\text{L}$ volume instead of $0.5\,\mu\text{L}$. Intuitively, this increased the durations of both wetting and wicking, as the droplet had to grow a larger receiving contact line for the former and pump a greater volume for the latter. Finally, figure 4.3d decreased the pore radius of the receiving surface by an order of magnitude. This did not substantially affect the external spreading of the droplet during the wetting regime, but did increase the wicking time scale by one order of magnitude. As will be seen in the next section, this is due to a combination of an order of magnitude increase in the capillary pressure and a two order of magnitude decrease in the permeability.

The evolution of the donor contact radius, the receiving contact radius, the donor contact angle, and the receiving contact angle are graphed in figure 4.4. The contact radii for each timestamp were calculated by using an edge finding program for each frame to get the shapes and positions of the bridge interfaces. Using the two sides of the bridge, the program is able to find each of the contact radii for each frame as well as any needed curvatures for the Laplace pressures or any instantaneous slopes for contact angles. All length measurements have resolutions between 4–10 μm due to the pixel size and slightly differing zooms used between trials. Each trial appears to have some lag between the wetting and wicking regimes, where the receiving radius is no longer increasing but is not yet decreasing. This intermediate state is especially apparent for the silicone oil trials, where the radii could be fixed for nearly 1,000 s before finally decreasing. This apparent stasis is actually the initial portion of the

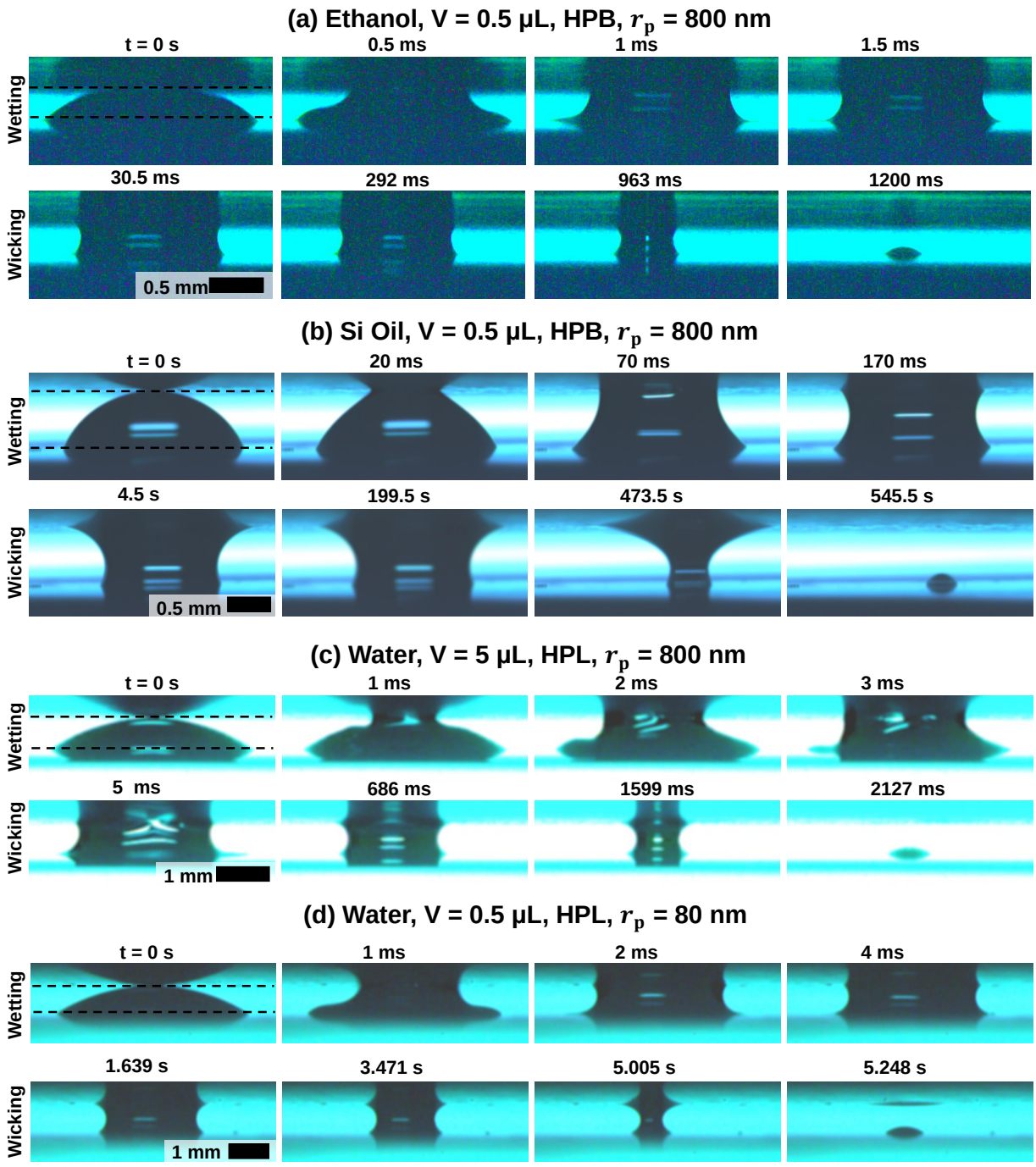

Figure 4.3: High-speed imaging of the droplet bridging process, where the working fluid, droplet volume, and pore radius were all varied. See Movies 3 and 4 in the Supporting Information.

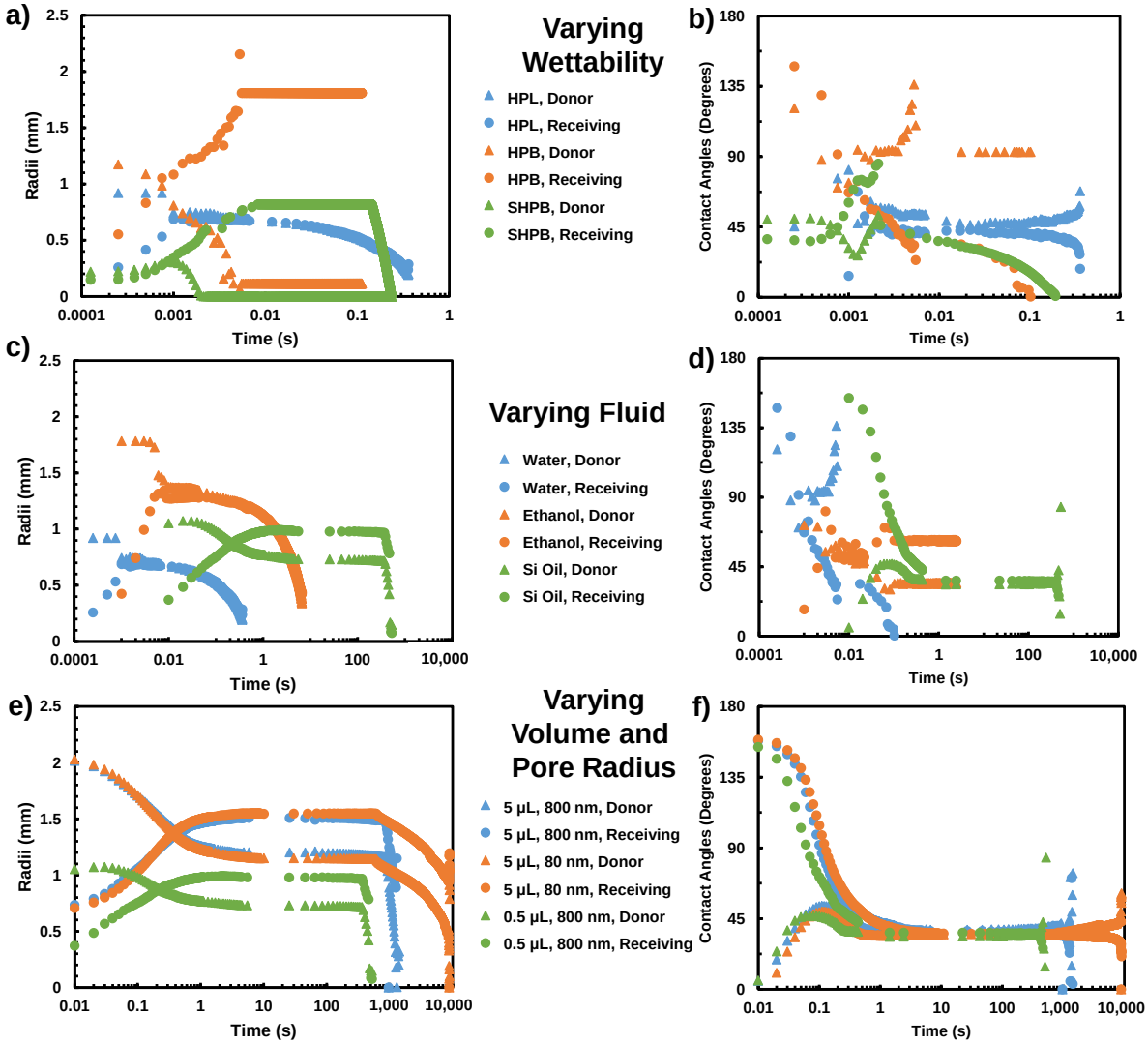

Figure 4.4: Evolving contact radii and contact angles over the entirety of the droplet bridging process. Each trial is shown as two data series, triangles for the donor radius or contact angle and circles for the receiving radius or contact angle. (a, b) The wettability of the donor substrate and (c, d) working fluid were varied for a $V = 0.5\,\mu$L droplet and a receiving pore size of $r_p = 800\,$nm. (e, f) The droplet volume and pore radius were changed, for a HPB donor substrate using silicone oil as the working fluid. The measurements of the contact radii are graphed in a), c), and e) while the measurements of apparent contact angles are graphed in b), d), and f).

wicking regime, as the receiving contact angle has to decrease from the advancing angle (during the wetting regime) to the receding angle. The contact angle data in the graphs on the right side do not reflect this, remaining surprisingly constant during the period of stasis in the contact radii. We surmise that this is because the apparent angles are being measured, rather than the actual local contact angles on the surface. This is supported in particular by the extremely high contact angles in Fig. 4.4f) during initial spreading, which are well above the expected advancing contact angle of a hydrophilic porous disk. While Fig. 4.4 contains a large amount of raw data, the relative timescales and differences between the apparent and local contact angles. The apparent advancing angle of the receiving surface varies from less than 25° to over 150°, while the apparent receding angle varies from less than 20° to over 60°, depending on the parameters of the experiment. This difference is not likely caused by an error in the image analysis program, as the only angle that can be discerned from the image is the apparent angle (see Fig. S1 in the Supporting Information). Rather, it is likely that the apparent angle is modified by the curvature and mass requirements of the liquid bridge. This is somewhat analogous to how multiple apparent and receding angles are observable with inertial contact lines, for example a sphere rapidly sinking past an interface [88]. While there should be only one true value each for the advancing and receding angles immediately at the surface, this was not observable with our setup.

4.4 High-Speed Imaging of Droplet Wetting Regime

In the first set of experiments, only a few frames were captured that corresponded to the wetting regime, due to the much longer duration of the wicking regime. Across all trials, the time duration of the wetting regime did not agree with any singular capillary-driven time scale. The capillary-inertial time scale, $t_{\mathrm{ci}} \sim \sqrt{\rho R^3/\gamma}$, ranges from $t_{\mathrm{ci}} \sim 1$–$100\,\mathrm{ms}$ depending on the droplet's volume and working fluid. This time scale dominates over the visco-capillary time scale, $t_{\mathrm{vc}} \sim \mu R/\gamma$, which ranges from $t_{\mathrm{ci}} \sim 0.1$–$1\,\mathrm{ms}$. In our case, R corresponds to the radius of curvature of the droplet prior to the onset of bridging. R is found using $R = (3V/(\pi(2+\cos\theta)(1-\cos\theta)^2))^{1/3}$, where the volume and contact angle of the droplet before bridging were known. When graphing the experimental wetting time scale against the capillary-inertial time scale, it can be seen that this single correlation doesn't agree across the entire range of conditions (figure 4.5). This indicates that the wetting regime is likely comprised of multiple sub-regimes, such that a higher temporal resolution would be fruitful for correlating experiments and theory.

To better resolve and model the hydrodynamics of the wetting regime, a second set of experiments was performed at a much higher frame rate to exclusively image the wetting regime. The results of the second set of experiments are graphed in figure 4.6. For silicone oil droplets, the receiving contact radius, $r_r(t)$, initially followed a power law of unity with respect to time (figure 4.6a,b). In contrast, droplets composed of water or ethanol appeared to initially follow a 1/2 power law (figure 4.6c,d). In both cases, the initial power law growth

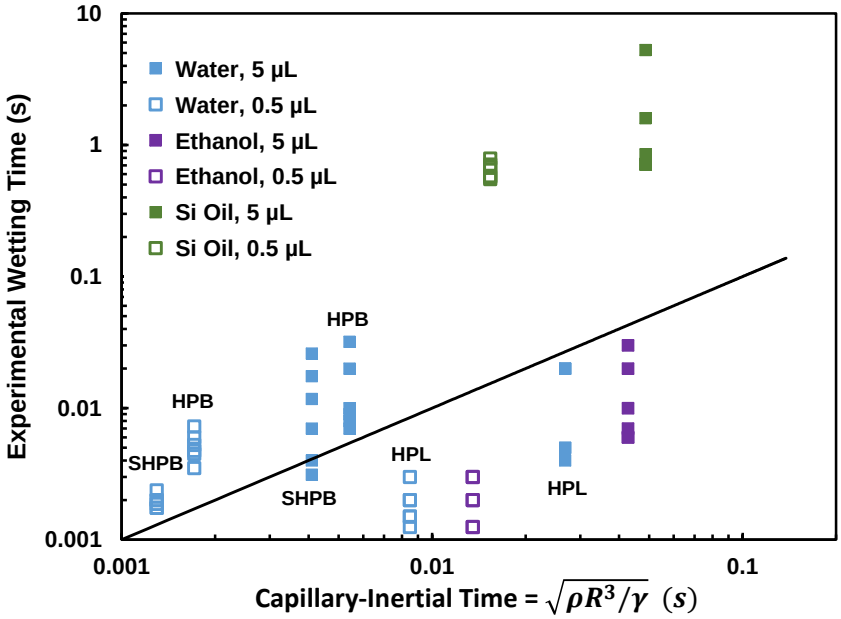

Figure 4.5: The experimental time scale for the wetting regime, versus the capillary-inertial time scale. The poor agreement motivates the more detailed modeling of the wetting regime, spliting it into donor-independent and donor-dependent subregimes.

transitioned to a slower growth rate that no longer exhibited a constant power law. This transition was observed to occur when the diameter of the receiving contact line approached the same magnitude as the height of the gap. It was also observed that the donor contact line began receding at the same time as this transition. Therefore, we hypothesize that the two sub-regimes observed during wetting can be conceptualized as a donor-independent regime followed a donor-dependent regime. The exception is the case of water droplets transferring from a SHPB substrate, in which case early pinch-off precludes the donor-dependent regime entirely. The donor-dependent regime can be abbreviated for water droplets transferring from a HPB substrate, as pinch-off tends to occur in the midst of the regime.

4.5 Modeling and Analysis

This system is difficult to model due to the lack of a characteristic (i.e., controlled) velocity. Previous studies of solid-to-solid droplet transfer used a moving receiving surface with a given velocity [3, 79, 81], while studies of spreading on porous surfaces controlled the droplet's impact velocity and were simulations. As this experiment lacks a moving substrate or droplet impact, a different approach had to be taken. All of the velocities of the system are driven by differences in Laplace pressures. Previous works on the spreading of a droplet on a porous surface revealed that when the droplet is much larger than the pores, there is a substantive disparity in the spreading velocity versus the (approximately one-dimensional) wicking velocity [89, 90, 91]. As such, we use two separate non-dimensional parameters to help begin modeling the system.

The Ohnesorge number, Oh, is the ratio of capillary-inertial and viscocapillary velocities:

$$\mathrm{Oh} = \frac{v_{\mathrm{CI}}}{v_{\mathrm{VC}}} = \frac{\mu}{\sqrt{\rho\gamma R}}, \tag{4.1}$$

where $\mathrm{Oh} > 1$ indicates that the capillary-inertial velocity is faster, such that the viscocapillary interactions are rate-limiting . The roles are flipped for $\mathrm{Oh} < 1$, resulting in capillary-inertial interactions being dominant for wetting. For these experiments, the values for Oh range from $10^{-2.5}$ to 1, indicating that the primary wetting dynamics could potentially be approximated as capillary-inertial.

The Coupling Parameter, CP, is the ratio of the (capillary-inertial) wetting speed to the wicking speed:

$$CP = \frac{v_{\mathrm{CI}}}{v_{\mathrm{Darcy}}} = \frac{\sqrt{\gamma/\rho R}}{\frac{\phi^2 r_{\mathrm{p}}\gamma}{4\mu\tau R(1-\cos\theta_{\mathrm{r}})}}, \tag{4.2}$$

where τ is the tortuosity of the porous ceramic, defined as the ratio of actual distance traveled in a porous media to the straight line distance between the beginning and end points of the flow front (i.e., $\tau \geq 1$). For these experiments, CP values ranged from $10^{3.5}$ to $10^{4.5}$, indicating that wetting occurs significantly faster than wicking, allowing the system to be analyzed as

if it's decoupled. In other words, we approximate the wetting regime as occurring prior to the wicking regime. Treating the regimes as sequential is further justified by the high-speed imaging of the bridging process, where the contact lines moved very quickly to their equilibrium position, stopped, and then later adjusted slowly as the fluid wicked into the porous disk.

4.5.1 Donor-Independent Wetting Regime

The initial donor-independent regime lasts from $r_r(t=0)=0$ until $r_r(t_{\text{cross}})\approx h$, where $r_r(t)$ is the contact radius on the receiving porous surface and t_{cross} is the cross-over time to the donor-dependent regime. The mechanism for this transition is the donor contact line's sudden onset of receding at $r_r \approx h$, which is required by conservation of mass in order for the receiving contact line to continue advancing. The power laws observed for $r_r \sim t^{\alpha}$ in the donor-independent regime, of $\alpha \approx 1/2$ and 1, correspond to the previously reported scaling laws for early contact line growth after gentle deposition on a hydrophilic surface [92, 93] and neck growth during droplet coalescence [94, 95, 96]. This similarity between droplet deposition and coalescence is due to the sharp curvature generated in either case. This sharp curvature is similarly observed here during the donor-independent regime.

The receiving contact radius, initially grows in a viscocapillary (VC) regime [96]:

$$r_r(t) = \beta_{VC}\frac{\gamma}{\mu}t, \tag{4.3}$$

where β_{VC} is a numerical pre-factor using the best fit value of a power law intercept for a given exponent. This regime is defined by the ultra-small neck radius, which limits the flow rate into the neck and increases the resisting viscous stress. The silicone oil droplets were observed to follow the power law of 1 from equation 4.3, indicating that early growth of $r_r(t)$ follows the VC regime. This was confirmed by non-dimensionalizing $r_r(t)$ in figure 4.6b using t/t_{cross} and r_r/h, where $t_{\text{cross}} = h\mu/(\beta_{VC}\gamma)$ and h are the cross-over time and radius, respectively. All data corresponding to the donor-independent regime effectively collapsed onto a master curve of $r_r/h \approx t/t_{\text{cross}}$ when the respective trials were fitted with $\beta_{VC}=0.1$ (5 μL Si oil droplets, $r_p \approx 800$ nm), $\beta_{VC}=0.08$ (5 μL Si oil droplets, $r_p \approx 80$ nm), $\beta_{VC}=0.15$ (0.5 μL Si oil droplets, $r_p \approx 800$ nm), and $\beta_{VC}=0.07$ (0.5 μL Si oil droplets, $r_p \approx 80$ nm) values. As Eq. 4.3 already has the viscocapillary velocity included in it, the β_{VC} values are purely fitting factors, wh This results in a universal cross-over from the VC regime to the donor-dependent regime occurring at $t/t_{\text{cross}} \approx 1$ and $r_r/h \approx 1$. We expect the slight variation in β_{VC} with r_p is due to the differences in effective surface roughness mildly, but not substantially, affecting the wetting.

We expect the water and ethanol trials shown in figure 4.6c similarly started in the VC regime, but it was not observed due to its short duration (~ 100 ns) at low Ohnesorge numbers. In the absence of a viscous outer fluid [97], the VC regime universally transitions into

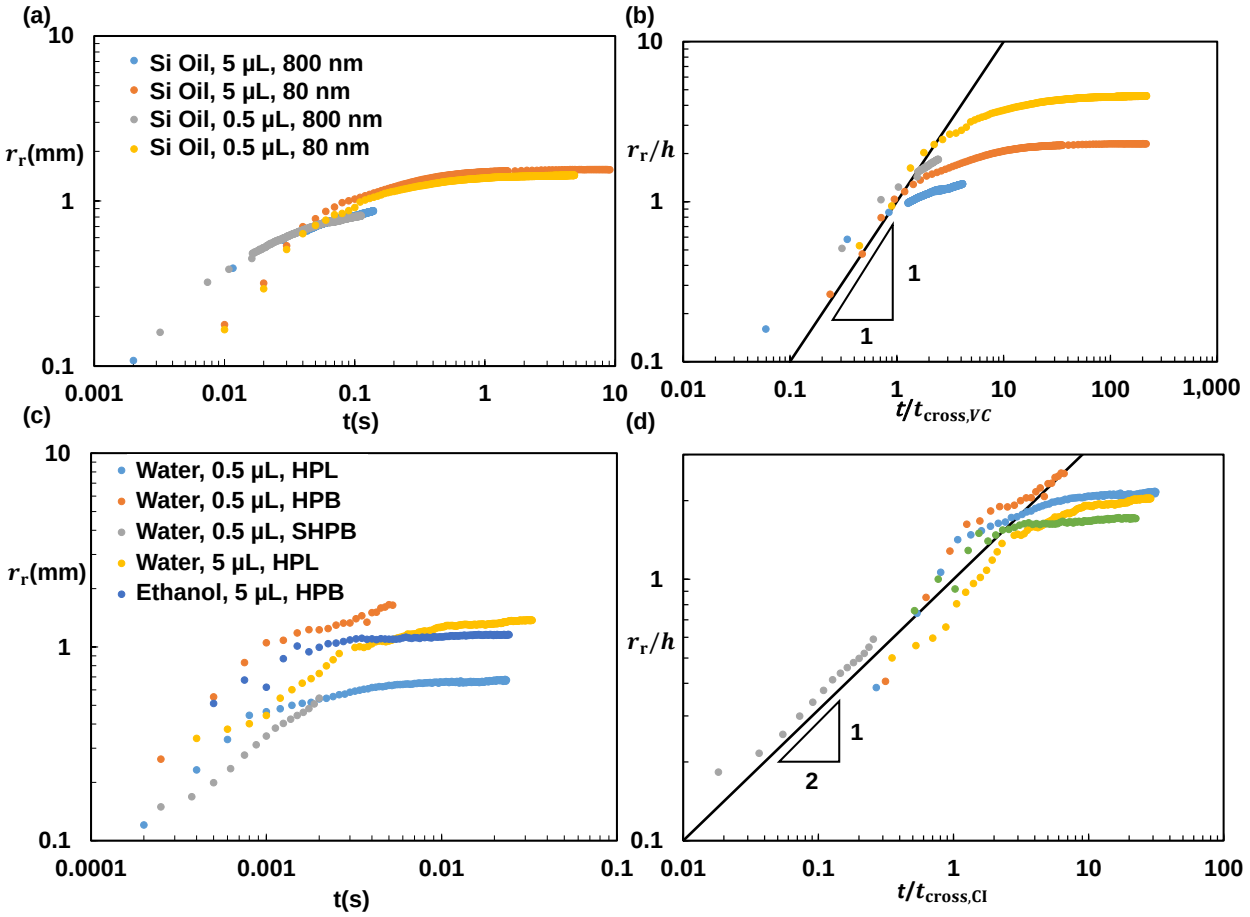

Figure 4.6: Receiving contact radii versus time during the wetting regime. (a,b) Silicone oil droplets bridging from a HPB substrate, for various droplet volumes and receiving pore radii. (c,d) Water and ethanol droplets, of varying volume and donor wettability, bridging into $r_p = 800\,\text{nm}$ pores. (a) and (c) are dimensional expressions of the receiving contact radius, whereas (b) and (d) are normalized by the gap height. During the first portion of the wetting process, r_r follows the scaling laws for droplet coalescence: (b) the mass-limited viscous regime (4.3) and (d) the capillary-inertial regime (4.4). t_{cross} is the cross-over time between the donor-dependent and donor-independent regimes, which occurs when $r_r \approx h$. The donor-dependent regime does not follow the same scalings, resulting in the divergence between the model and experiments when $t > t_{cross}$ and $r_r > h$.

the capillary-inertial regime:

$$r(t) = \beta_{CI} \left(\frac{\gamma R}{\rho} \right)^{1/4} t^{1/2}, \tag{4.4}$$

where β_{CI} is a numerical pre-factor and R is the initial radius of either droplet prior to coalescence. The data was again non-dimensionalized using t/t_{cross} and r_r/h, where now $t_{\text{cross}} = (h/\beta_{CI})^2 [\rho/(\gamma R)]^{1/2}$. This collapsed all experimental data for the donor-independent regime onto a universal curve of $r_r/h \approx (t/t_{\text{cross}})^{1/2}$ when using $\beta_{CI} = 0.7$ ($0.5\,\mu$L water droplets on a HPL substrate), $\beta_{CI} = 1.4$ ($0.5\,\mu$L water, HPB), $\beta_{CI} = 0.68$ ($0.5\,\mu$L water, SHPB), $\beta_{CI} = 1.22$ ($5\,\mu$L water, HPL), and $\beta_{CI} = 1.32$ ($5\,\mu$L ethanol, HPB). Cross-over from the capillary-inertial regime to the donor dependent regime once again occurred at $t/t_{\text{cross}} \approx 1$ and $r_r/h \approx 1$, validating that the capillary-inertial scaling law is in excellent agreement with these experimental trials during this regime. While the silicone oil droplets in figure 4.6b would hypothetically also transition to the capillary-inertial regime eventually, this could not happen in our context due to the earlier transition to the donor-dependent wetting regime, which will now be discussed.

4.5.2 Donor-Dependent Wetting

For $r_r > h$, the kinetics of the receding contact line are rate-limiting to the wetting process, rather than the kinetics of the advancing contact line. This crossover is forced by conservation of mass as the flow field grows within the droplet. The dimensions of the flow field in the donor-independent regime scale as $dz \sim r_r$ (where dz is the height of the advancing neck on the receiving surface) for both the viscocapillary and capillary-inertial regimes. This scaling stems from the neck being much smaller than the size of the droplet: $r_r \ll R$. The shape of the droplet visibly shows the growth of this flow field as mass is pulled from the sessile profile inwards, up, and then out towards the advancing contact line, allowing a trace of the height of flow field, dz, during the wetting process. This scaling breaks down when the height of the flow field matches the height of the gap, $dz = h$, as dz can longer grow but r_r continues to grow and r_d starts shrinking, transitioning from donor-independent to donor-dependent. The need for the contact line, r_d, acts as a new resistance, causing the transition at $r_r \sim h$. SHPB cases do not exhibit donor-dependent behavior as it is energetically favorable for those cases to pinch off. This is true for some of the HPB cases as well, which appear to produce bridge shapes very close to instability. This pinch-off is encouraged by the difference in contact angles between the donor and receiving surfaces, resulting in a large disparity in contact radii as well as the larger h values that result from higher initial contact angles on the donor surface. In regards to necking when it does occur in wetting, the larger the contact angle of the droplet on the donor surface, the closer the pinch-off point gets to the donor surface. An initial value of $\theta \geq 90$ results in the necking occurring at the surface, usually resulting in skipping the donor-dependent regime entirely.

This donor-dependent wetting regime does not appear to have any clean scaling law, as

supported by the constantly evolving power law slope in figure 4.6. We hypothesize that this messiness is due to the driving force now being a change in Laplace pressure across the entire liquid bridge ($\Delta P_{\text{adv}} - \Delta P_{\text{rec}}$), as opposed to the donor-independent regime where the dominant capillary force was entirely localized at the advancing contact line's neck. It is non-trivial to predict the global change in Laplace pressure across the liquid bridge, as the variance in pressure across the liquid bridge renders its shape unsteady in the absence of contact line pinning. This, in turn, makes the bridge profile indeterminate, even if the contact angles and radii are known. The dominant resisting force is not readily apparent, as it could alternately be inertial (ΔP_ρ) or viscous (ΔP_μ) in nature. To further complicate the picture, the viscous resistance could either be global (across the entire bridge) or local (within the receding wedge).

Assuming the driving force is indeed the global change in Laplace pressure across the liquid bridge, the governing stress balance is $\Delta P_{\text{adv}} - \Delta P_{\text{rec}} \approx \max(\Delta P_\rho, \Delta P_{\mu,\text{global}}, \Delta P_{\mu,\text{local}})$, where ΔP_{adv} is the Laplace pressure at the bridge's advancing contact line on the receiving surface, ΔP_{rec} is the Laplace pressure at the bridge's receding contact line on the donor substrate, and the right-hand side is governed by whichever resisting pressure drop is largest. Due to the aforementioned indeterminate shape of the liquid bridge, the evolving magnitudes of ΔP_{adv} and ΔP_{rec} had to be modeled semi-empirically, rather than using a single function for each of the pressures or the difference in the pressures that changes with respect to time, which is also true for the donor contact radius. Specifically, the radii of curvature at the advancing and receding contact lines were measured from the high-speed videos using a custom-made image analysis program. The radii of curvature at both the top and bottom of the bridge were then plugged into the Laplace pressure equation, $\Delta P = \gamma\,[(1/R_1) + (1/R_2)]$, to determine $\Delta P_{\text{adv}} - \Delta P_{\text{rec}}$. For all trials that exhibited donor-dependent wetting, we measured $\Delta P_{\text{adv}} - \Delta P_{\text{rec}} \sim 1$–$10\,\text{Pa}$ over the vast majority of the regime.

Hypothetically assuming inviscid flow across the liquid bridge and ignoring hydrostatic effects, the inertial resistance can be approximated using Bernoulli's equation. Specifically, $\Delta P_\rho \approx (\rho/2)(v_{\text{r}}^2 - v_{\text{d}}^2)$, where v_{r} and v_{d} are the average flow velocities across the liquid bridge near its top and bottom, respectively. The donor-dependent regime always begins at $r_r \approx h$, such that $r_{\text{d}} \sim r_{\text{r}}$ (i.e. the contact areas of the liquid bridge are commensurate). The aforementioned exception is the early pinch-off that occurs for water on SHPB substrates, which bypasses the donor-dependent regime entirely, and to a lesser extent for water on HPB substrates, where the donor-dependent regime is abbreviated. By conservation of mass, a natural consequence of $r_{\text{d}} \sim r_{\text{r}}$ is that the velocity of the receding contact line scales with that of the advancing one during the donor-dependent regime: $\dot{r}_d \sim \dot{r}_r$. By extension, the flow velocity across the liquid bridge scales with $v_{\text{d}} \sim \dot{r}_d$ near the bottom and by $v_{\text{r}} \sim \dot{r}_r$ at the top. This results in $\Delta P_\rho \sim 0$, i.e. the inertial resistance is vanishingly small. Plugging in experimental measurements of $\dot{r}_d$ and $\dot{r}_r$ into the Bernoulli equation validate this scaling argument, as this results in ΔP_ρ values that are three orders of magnitude smaller than the corresponding driving pressure of $\Delta P_{\text{adv}} - \Delta P_{\text{rec}}$. For example, for a $0.5\,\mu\text{L}$ water droplet transferring from a HPL substrate to a $r_p \approx 800\,\text{nm}$ porous surface, we measure $\dot{r}_d \approx 2.5\,\text{x}\,10^{-3}\,ms^{-1}$ and

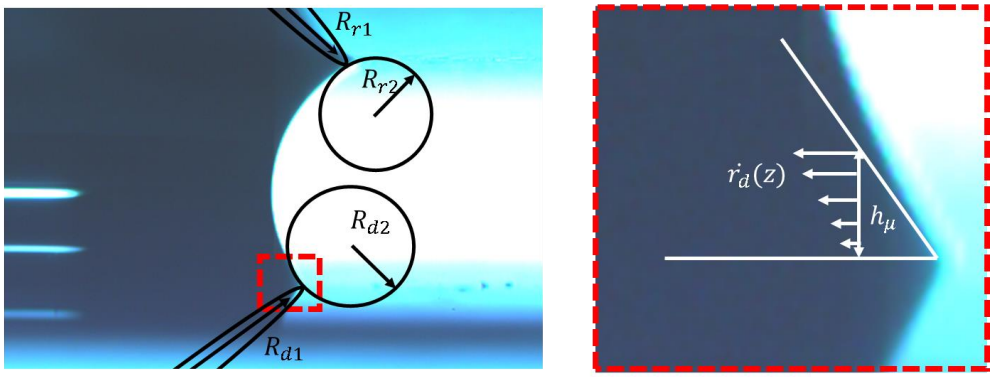

Figure 4.7: Conceptual overview of the donor-dependent wetting regime. The driving force for wetting is an asymmetric Laplace pressure caused by a mismatch in curvatures (left image). Wetting is rate-limited by a local viscous dissipation near the receding contact line (right image).

$\dot{r}_r \approx 3.5\,\mathrm{x}\,10^{-3}\,ms^{-1}$ at $t = t_{\mathrm{cross}} + 10\,\mathrm{ms}$. Still presuming that $v_\mathrm{d} \sim \dot{r}_d$ and $v_\mathrm{r} \sim \dot{r}_r$, Bernoulli's results in $\Delta P_\rho \approx 0.006\,\mathrm{Pa}$, which is significantly smaller than $\Delta P_{\mathrm{adv}} - \Delta P_{\mathrm{rec}} \approx 8.32\,\mathrm{Pa}$. We can therefore assume that the dominant pressure drop is viscous in nature and that the assumption of inviscid flow is not valid.

The bulk viscous stress was modeled as laminar pipe flow. To be conservative, the viscous pressure drop was maximized by assuming zero slip at the free interface and setting the pipe radius to the minimum neck radius of the bridge (r_{min}). This resulted in a Poiseuille pressure drop, $\Delta P_{\mu,\mathrm{global}}$, that was two orders of magnitude smaller than the difference in Laplace pressures, $\Delta P_{\mathrm{adv}} - \Delta P_{\mathrm{rec}}$. For the same example of a $0.5\,\mu$L water droplet transferring from a HPL substrate to a $r_p \approx 800\,\mathrm{nm}$ porous surface, we obtain $\Delta P_{\mu,\mathrm{global}} \approx 8\mu h \dot{r}_r / r_{\mathrm{min}}^2 \approx 0.036\,\mathrm{Pa}$ at $t = t_{\mathrm{cross}} + 10\,\mathrm{ms}$. This is again much smaller than $\Delta P_{\mathrm{adv}} - \Delta P_{\mathrm{rec}} \approx 8.32\,\mathrm{Pa}$, indicating that the bulk viscous stress is similarly insufficient to be rate-limiting.

Finally, a local viscous resistance accounts for the small length scale of the receding wedge. Previous reports have scaled the stress of a receding viscous wedge as $\Delta P_{\mu,\mathrm{local}} \sim \mu \dot{r}_\mathrm{d} / h_\mu$ [98, 99, 100], where $\dot{r}_\mathrm{d}$ is the wedge velocity and h_μ is the effective height of the viscous wedge (typically a semi-empirical fitting factor). When choosing an effective wedge height of order $h_\mu \sim 1$–$10\,\mu$m for water and plugging in the measured wedge velocity of $\dot{r}_\mathrm{d} \sim 0.1\,\mathrm{m/s}$, we obtain $\Delta P_{\mu,\mathrm{local}} \sim 1$–$10\,\mathrm{Pa} \sim (\Delta P_{\mathrm{adv}} - \Delta P_{\mathrm{rec}})$. Therefore, for a choice of $h_\mu \sim 1$–$10\,\mu$m that is consistent with previous reports, the local viscous wedge is dominant over the global inertial or viscous stresses and matches the magnitude of the driving capillary stress (figure 4.7). The governing equation for donor-dependent wetting is therefore given by:

$$(\Delta P_{\mathrm{adv}} - \Delta P_{\mathrm{rec}})(t) \approx \frac{\mu \dot{r}_\mathrm{d}(t)}{h_\mu}. \tag{4.5}$$

Using measurements of the Laplace pressures and $\dot{r}_\mathrm{d}$ from each frame in the donor-dependent

regime, we developed a semi-empirical approach to predict the evolution of r_d from equation 4.5. First we calculate the $\dot{r}_d$ and ∇P for each frame, assuming that they are roughly constant between each one. Then, using those values and equation 4.5, we calculate a value for h_μ for each frame. Then the average of the base 10 log for each h_μ is calculated and used as the best-fit value for a given trial. The ∇P, μ, and best-fit h_μ are then used to calculate a theoretical $\dot{r}_d$ for each frame, once again using equation 4.5. The results for this are then plotted against the observed values.

Four representative cases are graphed in figure 4.8, with their h_μ values in the caption. The trends in the plots show a correlation between the Laplace pressure difference across the bridge, exemplified from the theoretical data, and the velocity of the donor contact radius. The trend could then be used to predict the behavior of liquid bridges if the viscous wedge height is known. For the low viscosity cases, there can be a small increase in the donor radius temporarily. This occurs particularly in trials with short and wide liquid bridges, where there is very little room for the shape of the bridge to change, temporarily forcing some liquid outward, as parts of the liquid bridge above it changes curvature. The global Laplace pressure measurements reflect this change, allowing the model to predict this temporary advancing behavior. This estimate of the receding contact line does not directly relate to the advancing contact line due to the indeterminate nature of the shape of bridge, but recall that $|\dot{r}_d| \sim |\dot{r}_r|$ is approximately true by conservation of mass.

4.5.3 Wicking Regime

Droplet transfer enters the wicking regime when both contact lines have stopped moving. In most cases, droplets had to complete both the donor-independent and donor-dependent wetting regimes for this to be the case. However, for water droplets transferring from the SHPB or HPB surface, the wetting process ended in the midst of the donor-independent (SHPB) or donor-dependent (HPB) wetting regimes due to pinch-off occurring. Also note that wicking was occurring during the wetting regime itself; however, it did not appreciably affect the evolution of the liquid bridge due to the wicking process being much slower than wetting (figure 4.4).

Over our parameter space, the pore radius of the receiving surface is much smaller than the gap height between surfaces ($r_p \ll h$). The droplet volume's gradual migration into the wick can therefore be modeled using Darcy's law, equation 4.6 [101]:

$$v_{\text{wick}} \sim \kappa \nabla P, \tag{4.6}$$

where v_{wick} is the wicking velocity and $\kappa = \phi r_p^2 / 8\mu\tau$ is the fluid permeability of the porous surface [102]. As will be detailed later in the manuscript, a numerical model accurately captured the wicking rate for tortuosity values of $\tau \approx 2$ for the $r_p \approx 80\,\text{nm}$ ceramic surface and $\tau \approx 1.5$ for the $r_p \approx 800\,\text{nm}$ ceramic. We note that $\tau \leq 2$ is not typical for random porous media; therefore, the best-fit values for τ obtained here are assumed to be encompassing a

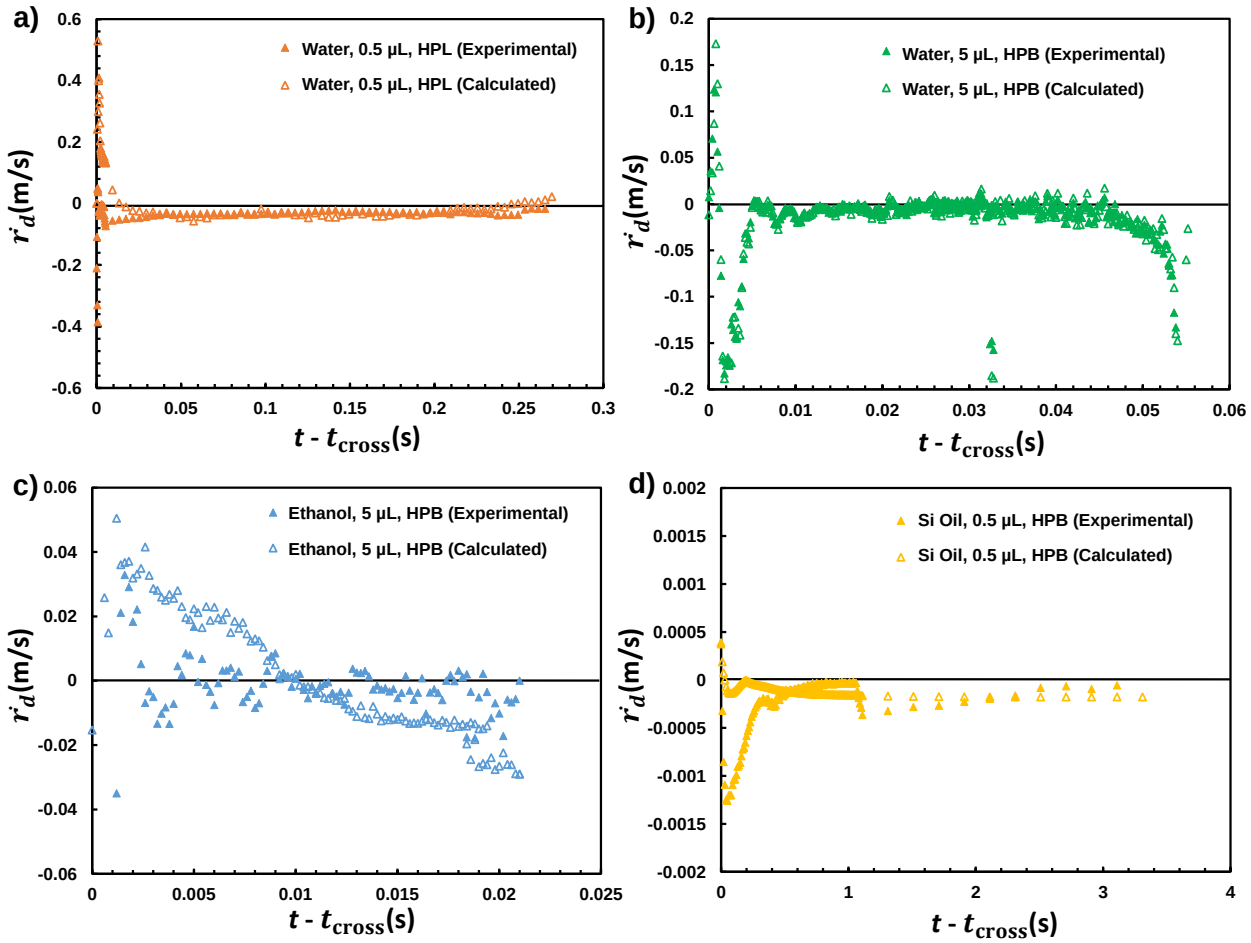

Figure 4.8: Experimental and theoretical donor contact line velocity. Time is defined as $t - t_{\text{cross}}$, where t_{cross} is the duration of the preceding donor-independent wetting regime. Experimental data is shown by solid points while theoretical data is represented by empty points. Four cases are shown with different parameter sets. a) water, $0.5\,\mu$L, HPL, $h_\mu = 11\,\mu$m, b) water, $5\,\mu$L, HPB, $1\,\mu$m, c) ethanol, $5\,\mu$L, HPB, $20\,\mu$m, and d) Si oil, $0.5\,\mu$L, HPB, $300\,\mu$m

fitting factor that accounts for various uncertainties in the porosity and wettability of the ceramic. The pressure gradient can be expressed in terms of the Laplace pressure of the menisci within the pores, $2\gamma/r_p$, divided by the wicking length scale required to fully accommodate the volume of the droplet, $L = R_c(1 - cos\theta_r)/\phi$. Note that R_c is the characteristic radius of curvature of a hypothetical droplet wetting the outside of the porous ceramic prior to wicking, where $\theta_r \approx 30°$ is a typical equilibrium contact angle of a droplet on the ceramic. The value for R_c is found by volume conservation, $R_c = (3V/(\pi(2+\cos\theta_r)(1-\cos\theta_r)^2))^{1/3}$, where V is the known droplet volume prior to the bridging process occurring. This results in a wicking velocity for a given droplet of:

$$v_{\text{wick}} = \frac{\phi r_p \gamma}{4\mu\tau L}. \tag{4.7}$$

This nonlinear velocity profile is consistent with Washburn's law and Darcy's law, as L is the distance that has to be wicked for total absorption. Finally, using $v_{\text{wick}} = \dot{L}$, Eq. 4.7 can be solved as an ODE, resulting in the following total time for wicking of an entire droplet:

$$t_{\text{wick}} = \frac{2\mu\tau L^2}{\phi r_p \gamma}. \tag{4.8}$$

Figure 4.9 compares the experimentally measured duration of the wicking regime against equation 4.8. Time zero is defined as the transition from the wetting regime to the wicking regime. The end of wicking is defined as when the last visible portion of the liquid wicks inside the porous ceramic, excluding when a pinched-off satellite droplet is trapped on the donor substrate. The experimental wicking times ranged from $t_{\text{wick}} \sim 0.1\,\text{s}$, for $V = 0.5\,\mu\text{L}$ water or ethanol droplets and $r_p \approx 800\,\text{nm}$, up to $t_{\text{wick}} \approx 10{,}000\,\text{s}$, for Si oil droplets and $r_p \approx 80\,\text{nm}$. Plotting these experimental times against the theoretical Darcy time scale results in all data collapsing consistently with a power law slope of about $y \sim x^{6/5}$. The most likely reason for the slope being slightly above unity is the scaling model's assumption that the liquid being wicked into the ceramic can be approximated as a single droplet. In reality, the liquid is usually in a bridge shape for the first portion of the wicking regime, only pinching off into a droplet part way through. This simplified model also neglects the volume of the pinched-off satellite droplet, which remains on the donor substrate. Regardless, the data collapses nicely against equation 4.8. To more explicitly capture the evolving bridge shape during the wicking process, we will now utilize a numerical approach.

Wicking Simulation

A simple numerical simulation can capture the receding speed of the liquid bridge during the first portion of the wicking regime. The bridge was treated as a quasi-equilibrium system, resulting in a constant Laplace pressure across the bridge. The quasi-equilibrium condition is supported by the multiple orders of magnitude differential between the wicking and wetting timescales. Therefore, any change to the bridge shape due to wetting will happen faster

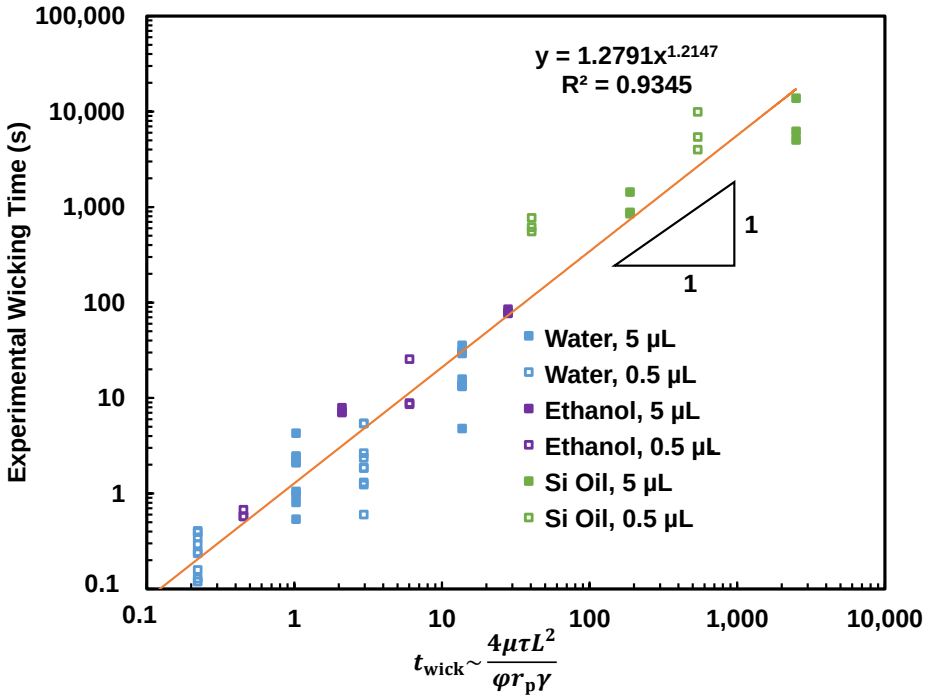

Figure 4.9: The experimental duration of the wicking regime compared with the theoretical Darcy time scale (4.8). The best-fit trendline exhibits a power law slope of greater than unity, which we attribute to the scaling model not accounting for the bridge's varying contact area and eventual pinch-off.

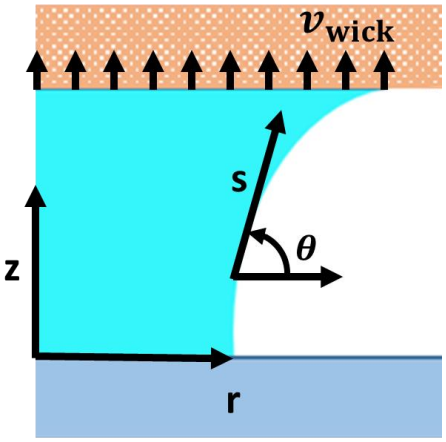

Figure 4.10: Schematic of the coordinate system used to develop a numerical model for the wicking regime. The bridge profile is made up of points moving along the free interface, s, with the changes in θ, r, and z governed by the their relationships between each other and a constraint of constant Laplace pressure.

than the changes caused by wicking, effectively decoupling the two processes. This allows the bridge shape to be numerically solved based on the following geometric constraints:

$$\frac{dz}{ds} = \sin\theta \tag{4.9}$$

$$\frac{dr}{ds} = \cos\theta \tag{4.10}$$

$$\frac{d\theta}{ds} = \frac{\Delta P}{\gamma} - \frac{\sin\theta}{r}, \tag{4.11}$$

where θ is the angle of the bridge profile with respect to the horizontal at any given point along the path of the free interface (s).

By measuring the bridge's contact angles at the donor and receiving surfaces at the beginning of the wicking regime, a bridge shape can be solved for a known liquid volume. Specifically, the contact radii on both surfaces can be solved using an implicit shooting method, where the receiving contact radius represents the area over which wicking occurs. The flow rate is then calculated from Darcy's law, equation 4.7. This wicking velocity was assumed constant over a sufficiently small time step, $\Delta t = 1\,\text{ms}$, to calculate a new (i.e., reduced) volume of the liquid bridge. The reduced volume of the liquid bridge is then used to solve for the contact radii and profile of the liquid bridge for the next time step, by assuming fixed contact angles on the surfaces and a constant Laplace pressure. By assuming the liquid wicks one-dimensionally into the wick from the contact area, the effective length scale of the liquid already within the wick is calculated as $L_{i+1} = L_i + v_{\text{wick},i}\Delta t$ to recalculate the pressure gradient for the

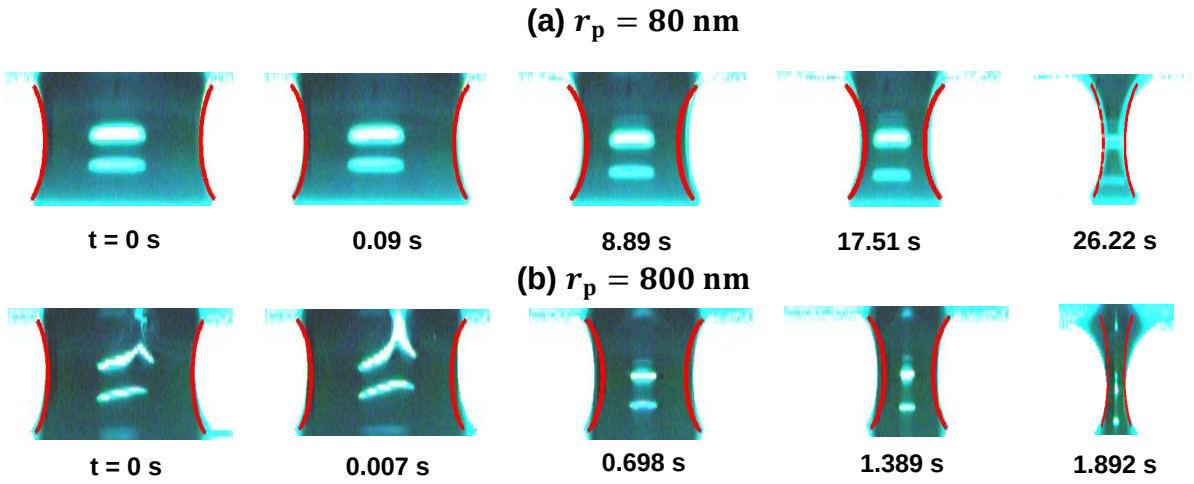

Figure 4.11: Results of the wicking simulation (red curves) overlaid on experimental time-lapse photographs. The experimental conditions are a $V = 5\,\mu$L water droplet on a HPL donor substrate, with (a) $r_p \approx 80$ nm and (b) $r_p \approx 800$ nm. Time zero corresponds to the beginning of the wicking regime, while the last frame of each video is the moment before pinch-off occurs.

next time step. The first time step arbitrarily used a wicked length scale of $L_0 = 10^{-6}$ m, to avoid a singularity in the pressure gradient and account for the minor wicking that occurred during the wetting regime. This process is then repeated iteratively to numerically capture the evolving profile of the shrinking liquid bridge as it wicks into the ceramic over time.

The numerical results are overlaid atop the experimental evolution of liquid bridges in figure 4.11. The two experiments chosen for comparison were 5 μL droplets wicking from a HPL substrate into $r_p = 80$ nm (figure 4.11a) or $r_p = 800$ nm (figure 4.11b) pores. The HPL substrate results in a liquid bridge for the vast majority of the bridging process, with pinch-off only occurring near the end. This maximizes the time duration where a comparison to the model's evolving liquid bridge can be made. Right up until the moment of pinch-off (last frame of each figure), the numerical model successfully predicts the evolving curvature and shrinking contact radii of the liquid bridge as it wicks into the porous receiving surface. The numerical model is therefore a nice complement to the simpler scaling model, as it can account for the evolving contact area over which the liquid is wicking into the pores, to obtain a more exact solution. We also used the numerical model to calibrate the porous surface's tortuosity, finding the best matching value to experimental behavior when $\tau \approx 1.5$ for $r_p = 80$ nm and $\tau \approx 2$ for $r_p = 800$ nm. These values were retroactively used in the scaling model above.

The final piece of the simulation is having the program determine when bridge failure should occur. The important factors for bridge failure are $\lambda = h/(r_d + r_r)$, $K = r_d/r_r$, and $V^\star = 8V/(r_d + r_r)^3$, which are the non-dimensional gap height, radii ratio, and non-dimensional

volume, respectively. Previous studies have performed numerical simulations where, for two given variables, the corresponding third value is solved that results in the onset of an unstable bridge shape [103]. Here, we fitted an analytical function to the simulation results, using λ and K as inputs and returning the minimum $V^\star$ for the bridge to be stable. K values varied from 0.1 to 1 and λ values varied from 0.6 to 4, with the corresponding critical $V^\star$ values being determined by numerical simulation by [103]. The resulting equation of fit for bridge stability is as follows:

$$V^\star > 5.438 - 51.88K + 6.135\lambda + 148.6K^2 - 33.36K\lambda + 4.729\lambda^2 - 122K^3 + 55.92K^2\lambda - 16.8K\lambda^2 + 2.252\lambda^3. \tag{4.12}$$

As K and λ individually increase, the stability of the bridge decreases, while an increase in volume increases stability of the bridge. The wicking simulations were stepped through time until reaching the first time step where equation 4.12 was not satisfied. For the simulation shown in figure 4.11a, pinch-off was predicted at 27.8 s, in good agreement with the experimental pinch-off which occurred at 26.2 s. In figure 4.11b, the numerical simulation combined with equation 4.12 predicted pinch-off at 2.1 s, again in fair agreement with the experimental pinch-off occurring at 1.9 s. Therefore, our numerical model can capture the onset of bridge breakup, in addition to its ability to evolve the bridge shape prior to breakup.

4.6 Conclusions

In conclusion, we have experimentally and theoretically characterized the hydrodynamics of a droplet transferring from a solid substrate to an opposing porous media. The most important findings are summarized below:

1. Droplet transfer is broadly composed of two regimes: wetting and wicking. The wetting regime is several orders of magnitude faster than the wicking regime, such that these regimes can be effectively decoupled when the pore radius is much smaller than the length scale of the bridging droplet.

2. The wetting regime is itself comprised of two sub-regimes: donor-independent and donor-dependent. In the donor-independent regime, the spreading of the receiving contact line on the porous surface follows the same established scaling laws that govern the rate of neck growth during droplet coalescence. In the donor-dependent regime, a local viscous wedge about the receding contact line on the donor substrate becomes rate-limiting, with the driving force being the global differential in Laplace pressure across the liquid bridge.

3. Using Darcy's law, a simple scaling model was able to collapse all experimental data regarding the total time required to wick the droplet into the receiving surface. The wicking time varied by several orders of magnitude, depending on the effective pore radius, liquid viscosity, and droplet volume.

4. A numerical model was developed that captured the shrinking contact radii and evolving neck shape of a quasi-steady liquid bridge during the wicking regime. By correlating our model with a pre-existing model of liquid bridge stability, we were also able to predict the onset of pinch-off, where the bridge becomes unstable, pinching off into droplets on either surface.

5. The wettability of the donor substrate heavily affects when pinch-off occurs and the duration of droplet transfer. For quasi-spherical water droplets, the droplet can fully dewet from its SHPB substrate to perfectly transfer to the porous surface, such that bridging never occurs. For hemi-spherical droplets, i.e., water transferring from a HPB substrate, bridge pinch-off either occurs during donor-dependent wetting or the very beginning of the wicking regime. Finally, for water droplets on a HPL substrate or low surface tension fluids on a HPB substrate exhibiting smaller contact angles, almost the entire liquid volume has wicked into the porous surface before the bridge becomes unstable.

These findings should inform the design of systems employing bridging-droplet transfer into porous media, such as phase-change thermal diodes.

Chapter 5

Full Scale Fog Harps: Limits of Lab Testing

The work in this chapter was funded by Comstock Inc. with assistance from Samscreen

5.1 Introduction

Water scarcity affects a majority of the world population for a portion of the year, and about 10% of the population throughout the entire year[104, 105, 106]. One of the solutions to this scarcity for certain regions is fog harvesting, potentially collecting thousands of liters of water per day[9, 10], by placing meshes perpendicular to the wind, catching the microscopic droplets suspended in the air. These sites currently use plastic meshes as they are lightweight, easy to setup and ship, and easy to replace when damaged, the most common of which is Raschel mesh[1].

Recently, harps have been proposed as a replacement to meshes[1, 11, 12, 13]. Meshes are made up of both vertical and horizontal elements. The horizontal elements can trap droplets and prevent them from sliding. These droplets fill in the holes in the mesh, increasing the aerodynamic resistance of the mesh, decreasing it's efficiency[107, 108, 109]. Harps seek to remedy this by removing the horizontal elements to allow droplets to slide freely. This presents another challenge though. The horizontal elements helped to keep the vertical elements in an even array, particularly when the droplets grow large enough to bridge between multiple wires[11]. The droplet then minimizes it's surface energy, pulling the wires together, effectively tangling them[110]. This tangling is resisted by the bending energy and the tension of the wires. The tangling pulls wires together, potentially reducing collection area.

This tangling is avoided in small scale harps, as the wires are so short that it is difficult to tangle them[1]. When harps start reaching larger scale, the scale of current meshes ($O(1\,m^2)$), the harp is tall enough that tangling can be a problem, or the harp is so short that the frame becomes large, reducing collection area. These large scale harps so far have been either hand wound, limiting tensioning capability, or with wire arrays that require more than one harp to reach the same collection values.

Here we show practical scale fog harps tested in a laboratory setting. We used ultransonic humidifiers to generate fog, allowing us to direct the fog and know the exact amounts produced for the harps to try to collect. Two harps are tested, with height being the only difference between the harps. This does result in two different areas for the harps but the collection efficiency normalizes this. We show here the limits of a laboratory testing environment as well as some of the advantages and drawbacks of fog harps.

5.2 Materials and Experiments

The harps that were tested were made by Samscreen Inc. Both of them used steel piano wires of 0.5 mm diameter(D), spaced, or pitched(P), 1 mm from center to center. This results in a P/D of 2, matching the best single layer efficiency for previous harp testing. Harp 1 was 1.35 m tall, while harp 2 was 0.6 m tall, pictures of which are shown in Figure 5.1. Each of the frames was 0.6 m wide, made up of 600 veritcal wires. The Raschel mesh was used in

a single layer.

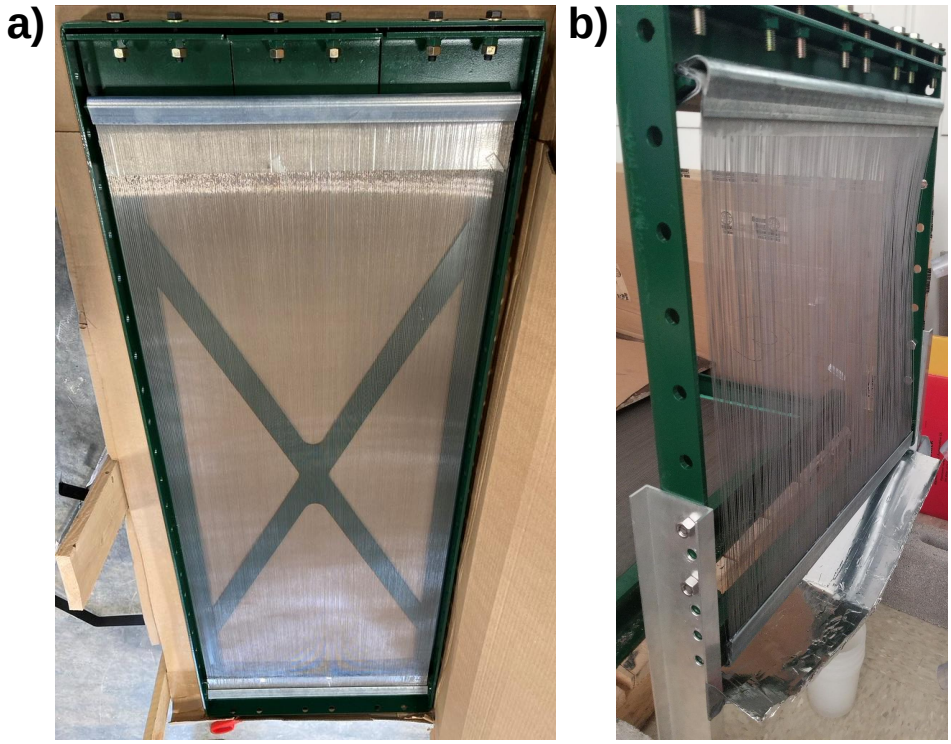

Figure 5.1: Harp 1 and harp 2 for this set of lab experiments.

The humidifers were Pure Guardian H940AR ultrasonic humidifiers. The term humidifier is a slight misnomer here as the device produces microscopic droplets similar in size to fog. 12 humidifiers were used for harp 1 and the raschel mesh, while 8 humidifiers were used for harp 2 due to space restrictions. The humidifiers were all tested to determine their fog production in g/min. This rate ranged from 0.69 g/min to 1.29 g/min and 3.14 g/min to 4.17 g/min for light and heavy settings respectively. These are the same model of humidifier used in our lab's previous fog harp tests. The humidifiers each had 1 in inner diameter tubes directing the flow of fog. The tube size and count then act as the actual collection area, rather than the area. Experiments were conducted in sets of 5 trials, each of which lasted 10 minutes. All tests were strted after a minimum of 20 minutes of fog generation, intending to simulate a steady state condition for the harvesters.

5.3 Results

Unfortunately, we were unable to test the first harp at higher tensions due to limitations of the frame. As such, we could only test collection efficiency at 4 wire tangling and higher. These

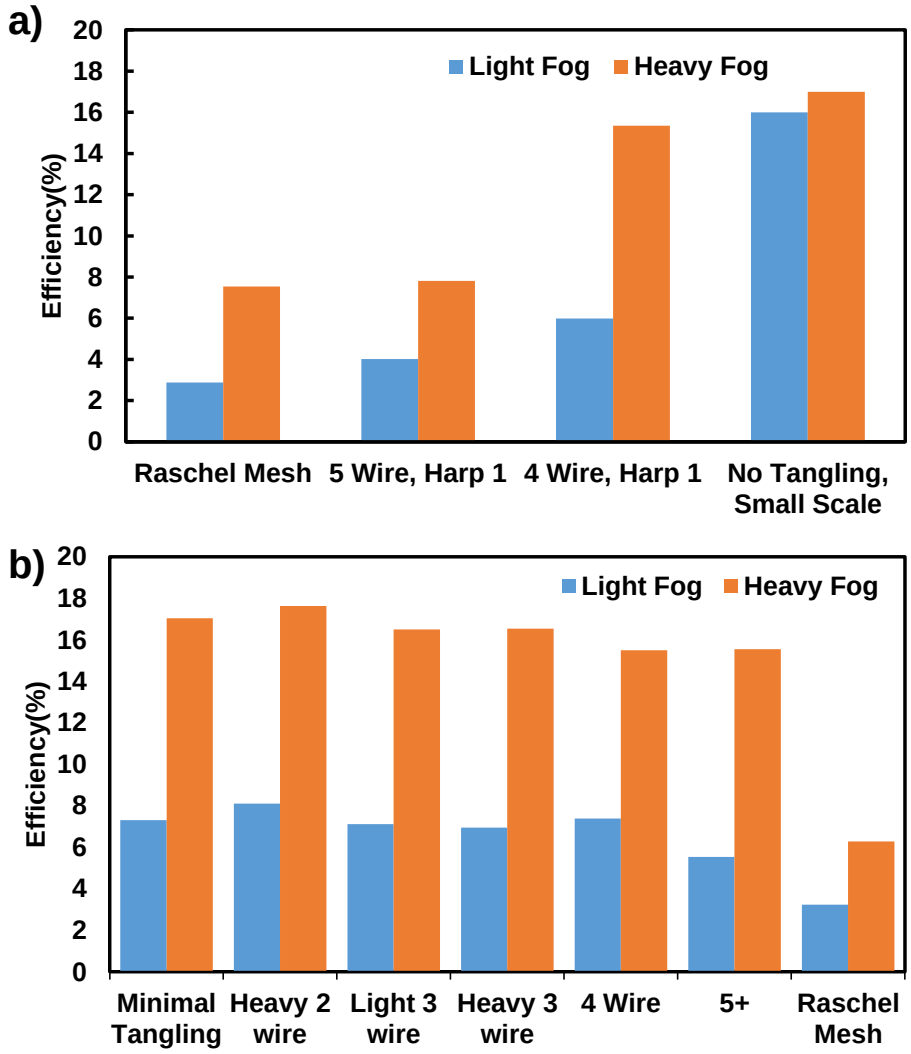

Figure 5.2: Collection efficiencies for a) Harp 1 and b) Harp 2 while showing different tangling behaviors. Raschel mesh was used as a control along with a comparison to the small scale collection efficiency previously reported in [1].

behaviors are shown in Figure 5.2a, along with a small scale and Raschel Mesh comparison. The harp with extensive tangling, up to 7 wires, performed similarly to the mesh. When increasing the tension, thus decreasing the possible wires tangled, the collection efficiency increases significantly. The efficiency matches the the small scale harp for heavy fog, but it doesn't match for light fog. Due to the inability to reach more optimal tangling behaviors, another harp was tested to attempt to find the limits of a large scale harp.

The results from the second harp are shown in Figure 5.2b. The results show a minimal increase in collection efficiency as the tangling behavior is improved, somewhat contractory

to previous results. There are slight improvements, but the tangling does not seem to be the limiting factor for this setup, especially given that harp 2 doesn't show a higher efficiency than the small scale harp does.

5.4 Analysis

These results are interesting for a couple primary reasons. The first is they show little change in the collection behavior with changes in tangling behavior for the second harp, while the first harp shows a large jump in collection from 5+ tangling to 4 wire tangling. The most recent work on fog harps showed a small increase from no tangling to 2 wire tangling, which is again seen here for harp 2. This increase is somewhat contradictory to the idea that droplets get caught in tangles and sliding efficiency is decrease by that as was previously proposed, especially since something else would need to increase to see an increase in efficiency. The sliding efficiency would only be affected by droplets being knocked off the wires. It's possible the collection area is slightly increased during two wire tangling due to droplets filling in area between wires.

The jump in efficiency for harp 1 can be explained by the non-uniform fog stream. Fog is only impacting the harp where the tubes are pointed. So, if 5 or 6 wires were suddenly pulled out of the fog stream by tangling, there could be a large drop in collection. This jump would not be nearly as pronounced for a field test with a uniform fog stream across the entire collection area. This is mathematically shown by calculating the change in collection area during n wire tangling. The collection area per wire is not as simple as the wire coverage, D/P, since droplets can be collected even if only a part of the droplet hits the wire. The collection area is estimated by $(D + 2a_{cap}D_{drop})/P$. This adjustment based on the droplet size accounts for only parts of the droplets impacting the wires. a is going to depend at least on fog velocity, wire wettability, and potentially droplet size. This is something to be explored further. From this the adjusted collection area is $(D+(2a_{cap}D_{drop}(1-(n-1))/n)/P$. This takes out $n-1$ wires worth of edges, 2 edges for 2 wire tangling and 4 edges for 3 wire tangling. This results in much smaller changes in collection area than would be necessary for the change in collection.

The other piece of this is the change in aerodynamic effects of the flow, as larger wires are going to create larger blockages, steering more flow away from them, and as such more droplets can be steered into the gaps. However, the small changes in harp 1 collection as tangling even reaches 5+ wires indicates that this doesn't have a large effect either for this setup. This aerodynamic effect is going to be limited by the velocity of the fog, which is around 1 m/s for the humidifiers, which is very slow for fog. As such, the velocity of the flow may already be limiting the aerodynamic efficiency of the setup even without the tangling. This could also be true of the raschel mesh which has much higher efficiency in field tests than it shows in lab tests with humidifers.

There is also a consistent difference in collection efficiencies for heavy and light fog which wasn't seen in previous small scale experiments. This is a piece that I don't have an explanation for yet.

5.5 Tangling Model

The previous work on this used an energy minimization process to develop a relationship between tension in the wires[1], and the tangling caused by droplets bridging between the wires.

For these harps we attempt to correlate the tangling behavior to the tension in the wires. The tension in harp 1 can be estimated using a tensiometer, in this case a Tensitron TX-1, allowing us to validate part of our model for the relationship between tangling and tension. We were unable to get accurate tension readings on harp 2 as the shorter height meant the displacement of wires to measure the tension would skew the value more.

$$[2(\pi - 2)\gamma R_{wire}]L_{dry}^2 = T[f(n, P, D)/n]^2 \tag{5.1}$$

This formula is a revised version of the previous ones used. Firstly, the beam bending term has been removed as its resistance was approximately equivalent to 1 mN of tension. As such, the beam bending term can be ignored to simplify solving the equation. L_{dry} can then be reduced for the two remaining terms. $f(n, P, D)$ is an updated wire displacement term, as the previous term of $(n - 1)$ did not accurately describe the displacement when wires tangle.

$$f(n, P, D) = \left\{ \begin{array}{ll} 0, & \text{if } n < 2 \\ D(n-1)(P/D - 1) + f(n-2, P, D), & \text{if } n \geq 2 \end{array} \right\} \tag{5.2}$$

$f(n, P, D)$ is a function for determining the amount of displacement required of wires for n wires of tangling. $f(n, P, D)$ is also a recursive function. This is because each tangling mode of n wires also includes the tangling behavior of $n-2$ wires, down to 0. For example, 4 wire tangling is 2 wire tangling with an additional 2 wires added on the outside of the original two, as shown in figure 5.3.

The modes of displacement for tangling are shown in Figure 5.3. The displacements fall into two groups, gap centered and wire centered. Even number tangling(2, 4, or 6-wire) is gap-centered, two wires meeting in the gap or wires between them. Odd numbered tangling(3, 5 or 7-wire) is wire-centered, two outer wires meeting with a wire or wires between them. This is an energy minimization process, 3 wires will meet at the middle wire not at an outer wire, as this is less displacement and therefore less energy. This presents as a recursive function as the tangling for 5 wires is the tangling of 3 wires plus two more wires on either side.

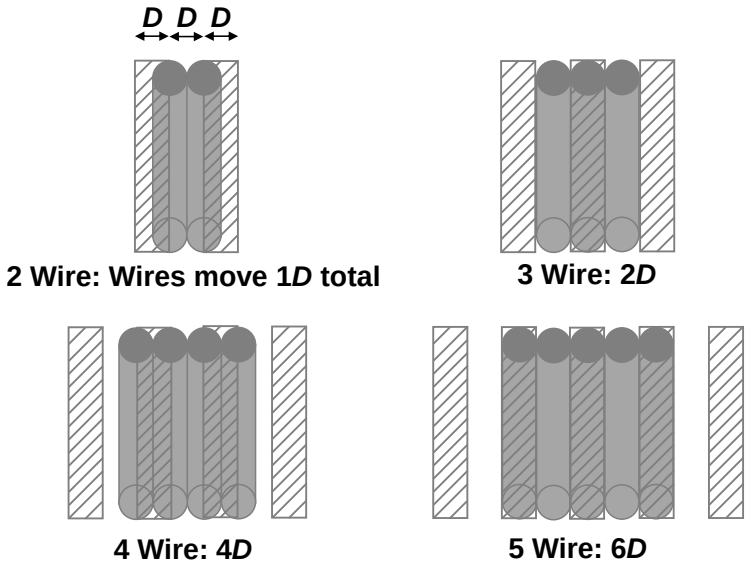

Figure 5.3: The initial positions(shaded) and the new positions of wires(solid) after tangling has occurred. The P/D for this example is 2. These modes can be expanded to other wire spacings.

This function is for the minimum displacement for n wires to be pulled together if wires are perfectly spaced.

The final tension and tangling behaviors are shown in figure 5.4. The most important piece of information here is that the required tension to prevent a tangling behavior is cut by a factor of 5. This is a massive reduction in load on the frame. The changes made here are not massive but they are significant, changing tension values for different tangling by roughly 20% compared to the previous model for all tanglings except for 2 wire, which stayed the same. This model could be useful in predicting tangling behaviors, and therefore predicting the minimum water content per area for sliding to occur on the harps. However, as shown earlier, tangling could have a very low effect on overall collection in a fog event that lasts hours with high water content.

5.6 Conclusions and Future Work

Here we've shown experiments testing large scale fog harps made using already available manufacturing techniques. The results were compared to both the industry standard Raschel mesh and the small scale harps that have been previously tested. These large scale harps seem to be capped at about 20% efficiecy, which is also consistent with the previous small scale tests. This suggests that lab tests might be limited by the nature of their setup, using humidifiers to make fog, limiting wind speed and potentially droplet size. An explanation

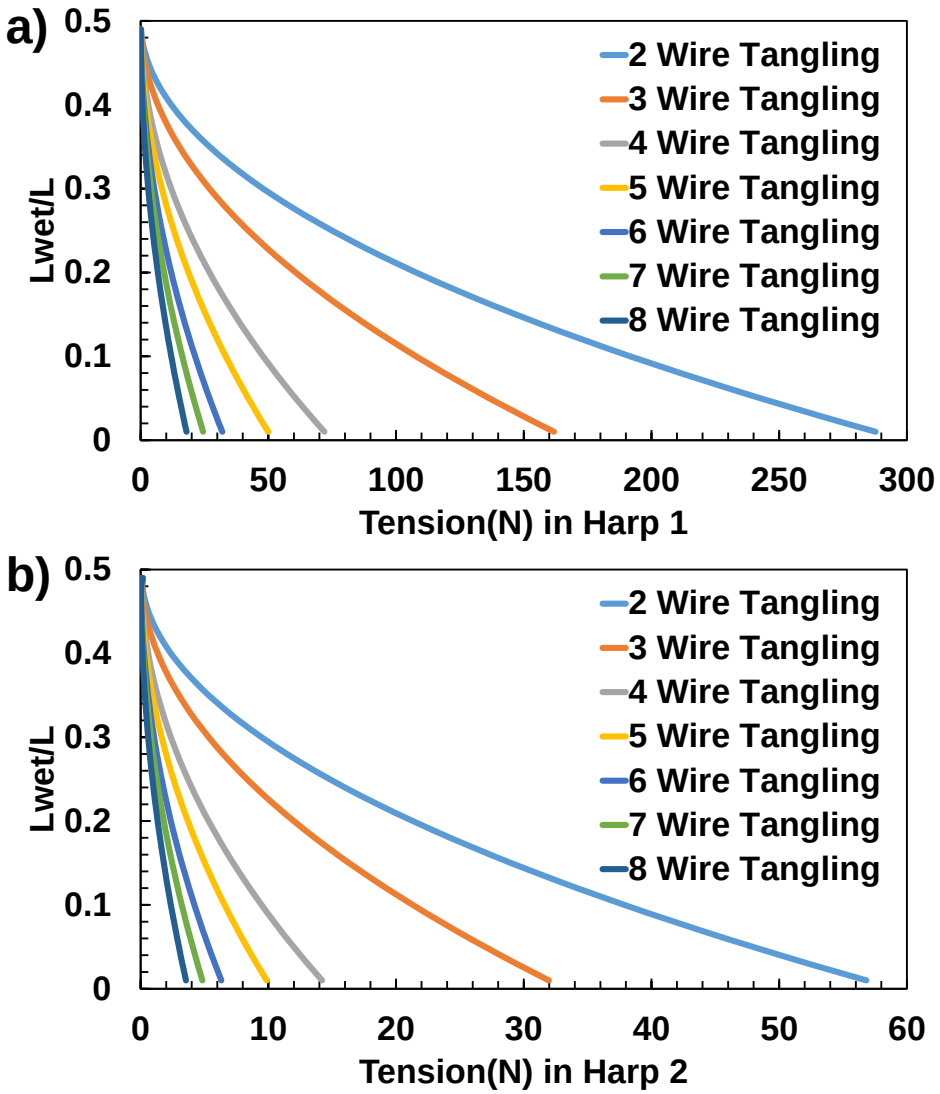

Figure 5.4: Critical tension forces for a tangling behavior to occur for each harp. Tangling occurs to the left of each line and does not to the right. Each tangling behavior can have each other tangling behavior of fewer wire count also occur.

would also be required for the difference in collection efficiency in the light and heavy settings. "Light" and "Heavy" may not be sufficient descriptors for fog events. They do not have a set standard for fog density, as well as duration of fog event being an important piece of information for fog collection. "Light" fog from a humidifier may not correspond well to a low density fog in the field. This is potentially supported by the disparity in collection efficiencies reported between Raschel mesh in the lab and Raschel mesh in the field.

Field tests need to be done to get more accurate comparisons between full size harps and meshes. CFD simulations could also be very useful for extra insights into the behavior of

flow around a harp and the behavior of droplets in that flow., potentially optimizing designs further for real world conditions. These harps could also be tested with a corona discharge setup. This might present some challenges as the wires may not all be connected depending on the manufacturing method, but could provide substantial increases in collection efficiency, similar to previous corona discharge setups.

Chapter 6

Solids being pulled on SLIPS surfaces

6.1 Introduction

The behavior of liquids and droplets on Slipper Liquid Impregnated Porous Surfaces (SLIPS) has been thoroughly explored in terms of durability, friction, sliding, and more[54, 98, 111, 112, 113, 114]. The ease of sliding for droplets on SLIPS has piqued particular interest due to the similarities to sliding on superhydrophobic surfaces[98, 112, 113, 114]. However, the studies so far are limited to liquids.

Here we begin to study the behavior of solid materials on SLIPS surfaces. The overall behaviors of liquids and their interactions with SLIPS are limited by the height of the fluid, typically limited by the capillary length of the fluid, usually $\sim 1\,\mathrm{mm}$. This limit no longer exists for a solid material, allowing much higher pressures compared to $\mathrm{O}(10)\,\mathrm{Pa}$ for water. These pressure increases have direct effects on the oil both above and within the microstructure.

Here, the behavior of a solid one inch aluminum cube when pulled along a SLIPS was studied. The force required to pull the cube at a constant speed was measured for a constant distance along the surface. Two microstructures were used for the surfaces, varying the solid fraction, with a smooth surface used as a control. Three different viscosity oils were used for infusing the surfaces, with dry surfaces used as a control. Three different spin rates were used, resulting in nine different initial thicknesses of the excess layer above the micropillars. The friction force was found to increase with the change from 10 cSt to 100 cSt, but then decrease from 100 cSt to 1000 cSt. The cube initially sinks into the oil layer following lubrication theory as it tries to displace the oil above the pillar tops. However this position in the oil is not maintained for the 1000 cSt cases and some 100 cSt cases. Importantly, the 100 cSt cases with the lowest spin-coating speed and the 1000 cSt cases have the largest excess oil thicknesses.

6.2 Materials and Methods

Three different types of silicon wafers were fabricated, two with microstructures, one remaining smooth. The microstructures were composed of square pillars in repeating square cells, as shown in Figure 6.1. This was accomplished using standard photolithography at Oak Ridge National Lab. The microstructures all used 9 μm square pillars that are 6 μm tall, h_p. The spacing between the pillars is then varied to get two different solid fractions, $\phi = 0.25$ and $\phi = 0.025$, shown in Figure 6.1. Multiple copies of each of these microstructures was made to use with different oils and spin coat rates.

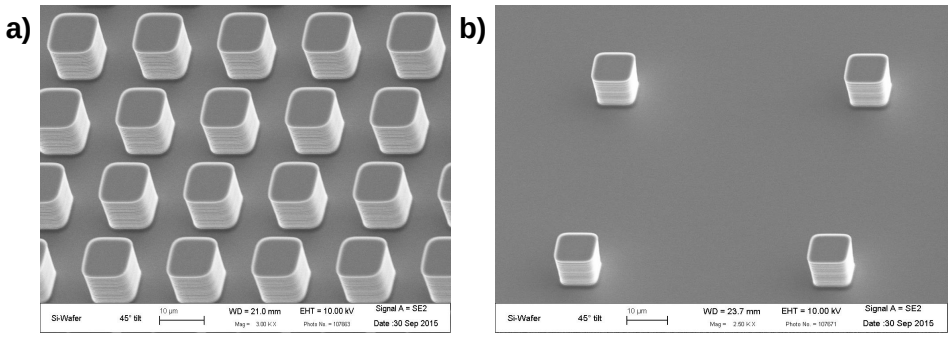

Figure 6.1: The two microstructures used to make the oil-infused surfaces. a) has a solid fraction of 0.25 and b) has a solid fraction of 0.025.

Three different silicone oils were used, varying the viscosities, ν, for 10 cSt, 100 cSt, and 1000 cSt, which can be used to calculate μ using the density. This variance in combination with three different spin coating speeds, 2000 rpm, 3000 rpm, and 5000 rpm, resulted in nine different initial excess thicknesses on the substrates for each microstructure. The spin coating time was a constant at 15 s for all combinations. This results in the initial excess thicknesses listed in table 6.1. It was assumed that the microstructure was trapping the oil within it, isolating the effects of the spin coating on the excess oil above it.

δ_0 (μm)	10 cSt	100 cSt	1000 cSt
2000 rpm	3.9	12.3	39.0
3000 rpm	2.6	8.2	26.0
5000 rpm	1.6	4.9	15.6

Table 6.1: The 9 thicknesses of oil layer above the microstructure after 30 seconds of spin time.

For all experiments a 1 in. polished aluminum cube was used. The cube was placed on the surface and allowed to sit for 60 s. The cube was then pulled at a constant 1 mm/s, U, for 20 s, totalling 2 cm of travel distance. The force during the pull was measured and graphed with time. The average of the force during the travel was used as the primary measurement.

6.3 Results

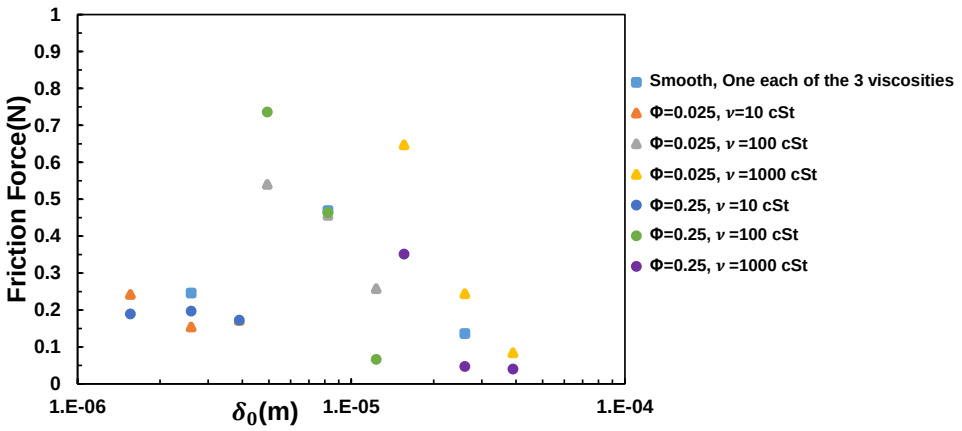

Figure 6.2: Average friction over the 20 sec pull for all trials. Friction force is plotted against δ_0, but trends with viscosity and spin coat speed can still be extracted.

The results for all trials are graphed in figure 6.2. The friction is plotted against the initial excess thickness. Moving left to right on the graph, viscosity is increasing and spin coat speed is decreasing. The most notable piece of information is the increase in friction force between 10 cSt to 100 cSt and then the decrease between 100 cSt to 1000 cSt, despite the increase in viscosity. This is contradictory to the idea of higher viscosity, higher friction, which is the intuitive idea. The other piece is that the larger excess could reduce drag by having a larger lubrication layer, but also potentially increase depending on how much the cube sinks into the oil. There are two possible sources of friction here, shear stress drag beneath the cube and Stoke's drag in front of the cube. Shear stress of the oil layer on the cube can be calculated as follows:

$$F_{fric} = W_c^2\left(\frac{\phi U \mu}{z_c} + \frac{(1-\phi)U\mu}{z_c + h_p}\right) \tag{6.1}$$

W_c is the width of the cube and z_c is the distance between the bottom of the cube and the tops of the pillars. The drag of the oil at the front of the cube can be estimated using Stoke's drag and even at the highest viscosity and excess thickness is O(1 mN), making it negligible compared to the drag the cube is experiencing. This gives a direct relationship between the friction force and z_c. This leads to the question of z_c, and estimating it for the trials.

6.4 Gravitational Drainage

The experiments start with the cube being placed on the oil-infused surface. For a known fluid and constant spin rate, the initial excess thickness that the cube is placed on can be estimated with the following:

$$\delta = \sqrt{\frac{\nu}{\omega^2 t_s}} \tag{6.2}$$

Where ν is the kinematic viscosity, ω is the angular velocity used for spin coating, and t_s is the total time for spin coating, 15 s for all trials. The microstructure holds the oil within it stationary, isolating the effects of the spin-coating to the layer above the structure. The cube is assumed to start from the top of the oil layer.

While the aluminum cube is stationary on the surface, oil is forced out from beneath it due to the hydrostatic pressure of the cube. The limiting factor is the ability of the cube to push oil off the tops of the pillars.From lubrication theory we can derive the scaling between the driving pressure of the cube and the gap through which the oil must be squeezed.

$$\frac{\Delta P_{cube}}{w/2} \sim \frac{2U_t \mu}{(z_c/2)z_c} \tag{6.3}$$

This assumes a no slip condition and mirrored flow along the lines of symmetry of the pillar tops. Equation 6.3 can then be solved for a characteristic velocity of the flow.

$$U_t \approx \frac{\Delta P_{cube} z_c^2}{8\mu w} \tag{6.4}$$

This velocity can then be used to calculate a total volumetric flow rate for the top of the pillar.

$$Q_t = \frac{8}{\phi}\frac{W_c^2}{p^2}\int_0^{w/2}\int_0^{z_c} U_t \frac{16}{w^2 z_c^2}(w/2+x)(w/2-x)(z)(z_c - z)\,dz\,dx \tag{6.5}$$

And the volumetric flow rate can be linked by conservation of mass to the sinking of the cube, $\dot{z_c}$.

$$\dot{z_c} W_c^2 = Q_t/\phi \tag{6.6}$$

This ODE can be solved for an exact solution using the initial condition of $z_c(0) = \delta_0$. Based on the fixed parameters for our experiment set this reduces to the following:

$$z_c(t) = \frac{\sqrt{30.5\mu\phi}}{\sqrt{\frac{30.5\mu\phi}{\delta^2} + 7.29 * 10^{13} t}} \tag{6.7}$$

This model was adjusted for the smooth substrate, changing the controlling length scale to that of the polished aluminum for the lubrication theory resulting in the following.

$$z_c(t) = \frac{0.478121\sqrt{\mu}}{\sqrt{\frac{0.2286\mu + 2.73812 * 10^{10}\delta_0^2 t}{\delta_0^2}}} \tag{6.8}$$

These equations result in the following z_c values for all of our trials after 60 s of the cube sitting on top of the excess.

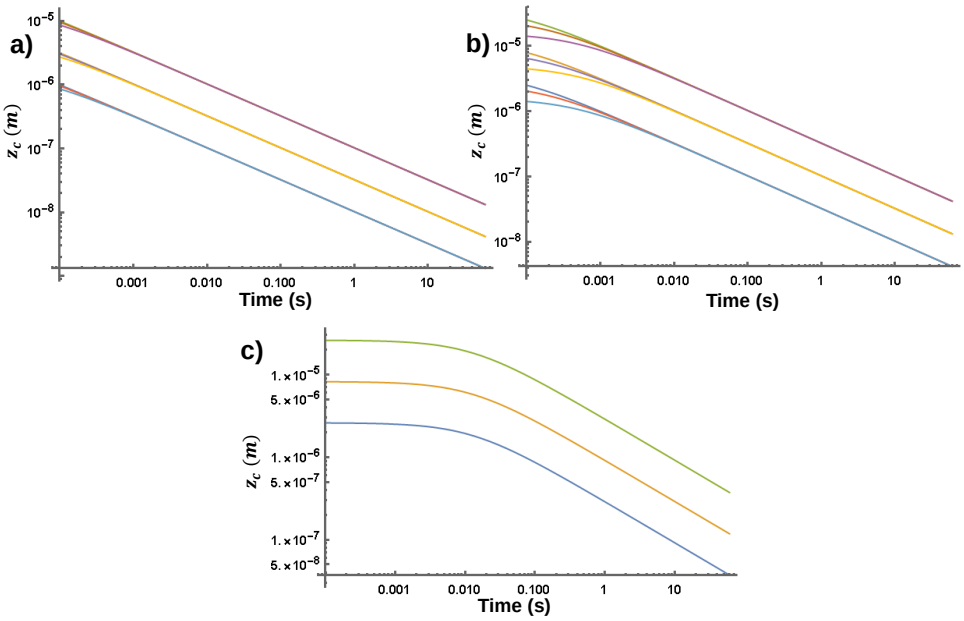

Figure 6.3: z_c for all combinations of structures, oil, and spin coat speed. a) is for ϕ =0.25, b) is for ϕ =0.025, and c) is for a smooth surface. Oil viscosity and surface structure are the primary factors in determining the position of the cube once 60 seconds have passed.

We can then take these values at 60 s and caluclate the friction force on the cube given that value using the equation for shear stress on a surface.

The gravitational drainage predicts reasonably accurately the 10 cSt and 100 cSt friction forces, implying that the cube stays at roughly that z_c throughout the 20 s pull. This needs another addition for the 1000 cSt trials, as well as the 100 cSt cases with the largest initial excesses as the friction force plummets, likely indicating that the

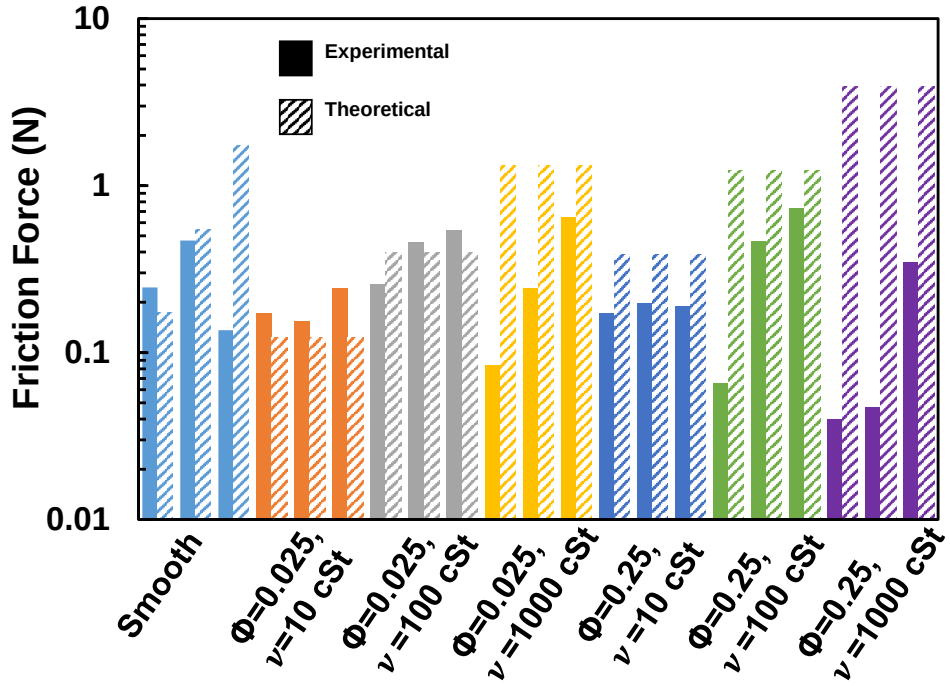

Figure 6.4: The experimental and theoretical friction values using only the gravitational drainage for cube position. The predictions are reasonably accurate for the low δ_0 cases, but not for the larger cases.

6.5 Increasing Viscosity, Decreasing Friction

There is a trend once the initial excess reaches $9\,\mu m$ that the friction force begins decreasing. However, this trend appears to be somewhat misleading. The decrease in friction force, sometimes by a factor of 10, is not inherently linked to the increased excess. The initial excess is the result of higher viscosity and lower spin coating rate. However, the initial excess is not significant for predicting the pull value after 60 s of drainage.

This becomes an interesting question then. Is this caused by a larger buildup of oil in front of the cube as it's being pulled? The visco-capillary velocity($v_{vc} \sim \gamma/\mu$) for the highest viscosity is O(0.01 m/s). This velocity is faster than the cube movement, preventing a larger excess from building up in front of the cube as it's being pulled. Therefore the only Stoke's drag force from the front is given by the δ_0 value, $F_{SD} = 6\pi\mu U\delta_0$. This force is O(0.001N) for the 1000 cSt oil, so it isn't the reason for pulling resistance and the moment generated by it is secondary to all the other forces.

The cube has a moment couple being exerted on it by the pulling force and the friction force below it, which are matched by being pulled at a constant speed. The cube is also now sinking so slowly that it can be treated as having an equal gravitational force down and normal force holding it up. The effective normal force can move to balance out the moment

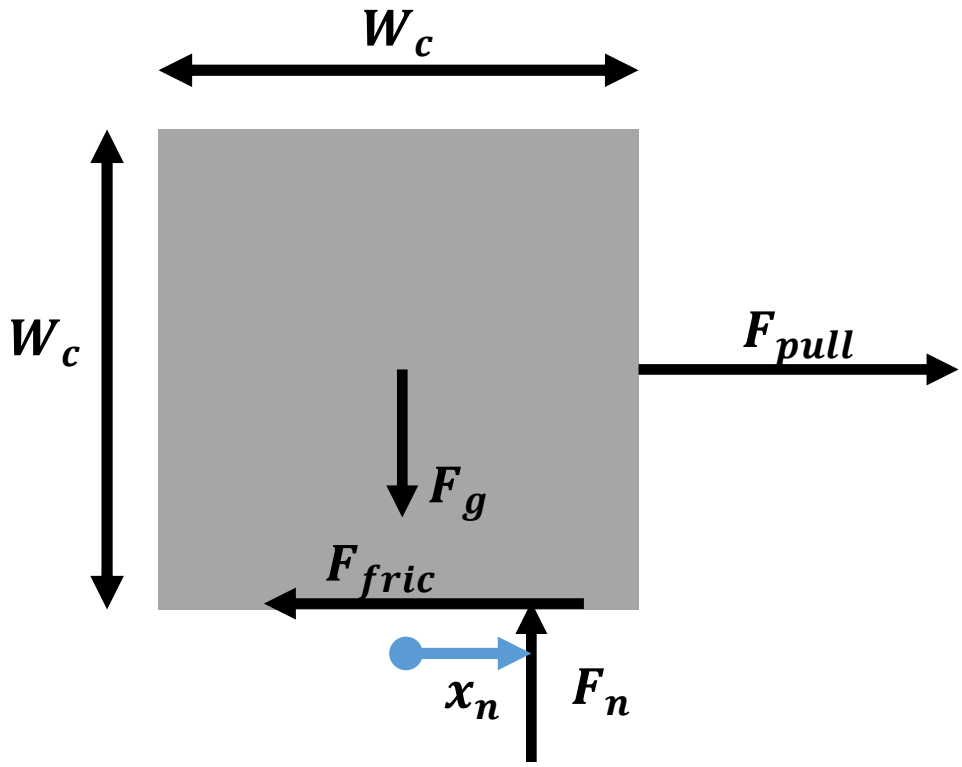

Figure 6.5: An estimate of why the cube begins turning. The normal force can be assumed to be approximately the same as the gravitational force as the cube is falling extremely slowly. The normal force is representative of a pressure that is resisting the falling and moves based on the moment produced by the pulling and friction. If the normal force reaches the front edge of the cube, the cube will start to turn.

caused by the pulling and friction. The normal force can move until it is at the front of the cube, after that the cube starts to rotate as the moments can't balance each other anymore. This happens when the initial friction force would be larger than the gravitation weight of the cube due to the setup dimensions, however a general formula for this is possible. The balancing of forces after this to solve for the friction force experienced by the cube has not been solved yet, as such this rotation is only a guess at the moment. However, the cube would experience lower friction forces as it started rotating and part of it lifted up, and the lowest friction forces are measured for the cases with the largest initial friction force, supporting the idea that they are rotating.

6.6 Conclusions

Initial steps have been made to be able to accurately predict the behavior of solid objects on oil-infused microstructured surfaces. The drainage from the gravity of the cube was modeled

reasonably accurately, allowing for accurate preictions of friction forces for cases with low initial friction. The gravitational pressure was matched by the viscous pressure between the bottom of the cube and the pillar tops. A small adjustment can be made to get a moel for the smooth substrate as well. Interestingly, the initial oil thickness was not a major contributing factor in the friction force, and was loosely correlated because it was also reliant on the density of the oil.

There is a lot more work to do for this. The turning part of the model still needs to be solved, but when it does, then the surfaces can be studied much more deeply. The surfaces can be systematically studied, varying the surface structure more, as well as testing the durability of the surfaces. The drainage of the oil can also be characterized, allowing for the understanding of sequential trials. This is the key piece of information missing still, the durability of the surfaces, a part of which is how long the oil layer lasts compared to a smooth surface.

Chapter 7

Current States and Future Works

7.1 Conclusions

Here I've shown four somewhat separated projects in fluid mechanics and fluid-surface interactions. Each project with a different application of capillarity and requirements. One was a pure fluid mechanics work, one was a very application focused work, and two more in between them.

A direct side-by-side comparison of frost melting on hydrophobic and superhydrophobic surfaces was performed, allowing precise understanding of the effects of a combined chemical and surface nanostructure on meltwater adhesion. The superhydrophobic surface uses its very low adhesion to shed meltwater from melting frost easily. It starts shedding at lower tilt angles and frost thicknesses than a hydrophobic surface does. This gets further clarified with a simple equation for predicting the largest remaining and smallest removed droplets as well as another equation for predicting removal of an upside-down frost sheet based on the thickness. The superhydrophobic surfaces do still lack durability, so while it may work the first time, it may need to be reapplied after a couple runs.

A systematic study of the behavior of sessile droplets and their transfer after they touch a porous surface was done. The experiments used varying droplet fluids, donor surface wettabilities, and porous receiving surfaces, allowing for a wide range of interactions. The behavior of the droplets can be split into two major regimes, wetting and wicking. Wetting is the the process of the droplet spreading across the outside of the porous surface and follows standard droplet spreading behavior initially. The wetting regime is split into two subregimes, donor-independent and donor-dependent. When the donor-dependent regime starts, the droplet spreading on the porous surface becomes limited by the receding behavior on the solid donor surface. The wetting continues until the Laplace pressure across the liquid bridge becomes constant. At this point, wicking takes over, with the droplet being pulled into the porous surface following Darcy's Law, taking typically 1000 times longer to complete than wetting did. Wicking has both an accurate scaling and numerical time-stepped solution.

Lab tests were performed on full scale industry fog harps, testing for the effects of harp size on collection efficiency, as well as further testing the tangling behavior of fog harps. Tall harps can tangle from droplet coalescence very easily, due to the long wires. The lab tests were somewhat limited by the ability of the humidifiers to generate fog. The tests did show

an interesting lack of dependence on tangling for the shorter harp. This could be do to the lab setups being reliant on small diameter tubes from humidifiers, allowing wires to be pulled out of the flow when a large number of wires tangle together. This leads to the question of field tests being necessary for fog harvesting.

The behavior of solid objects on SLIPS has been only initially explored, with one of the two regimes having a plausible explanation and model. There was a very interesting interaction where increasing the oil viscosity actually decreased the the friction experienced by the aluminum cube. However, this is due to the cube being able to turn as a result of high initial friction and not being confined to the space. Once the cube starts turning, friction drops drastically as the distance between the cube and the surface starts increasing, as friction force being inversely related to that distance.

7.2 Future Work

Defrosting on superhydrophobic surfaces could be applied to a number of situations, the most immediate of which is the aerospace industry. The ability to apply these treatments and maintain them could save millions in chemical usage or energy costs. The durability of the superhydrophobic coating is the limiting factor at the moment.

Droplet-bridging mechanics can be applied to the design and optimization of thermal diodes. Bridging-droplet thermal diodes have already been proposed, tested, and analyzed. They generally used structures whose characteristic length scale was approaching the length scale of the droplets, changing the hydrodynamics substantially. The hyrodynamics may need to be studied on their own, as they likely cannot be separated into wetting and wicking.

For thermal diodes where that is not the case, and the wetting and wicking regimes can be separated, wicking is likely the limiting factor for design considerations. The 1000x disparity in time scales across fluids, droplet size, and wettability means that the ability for the wick to pull the fluid back in is the mechanism that dryout is competing against. Water generally took less than a second for wicking to complete, which should be fast enough for some applications, but that time can also be decreased by decreasing the gap height and therefore the droplet size. Droplet sizes of less than $100\,\mu$m are going to be difficult to control and maintain physically though purely because of the difficulty of creating a consistent gap of that size. There could also be the consideration of heat transferring through the droplet while it's bridging if the bridge lasts long enough, and is large enough, both of which could occur for larger gap heights.

The fog harvesting work has a number of routes that it can take from this point. Field testing is the most immediate concern in my opinion. Lab testing has inherent limitations at the moment and field testing can vary a number of factors that the laboratory can't, including wind speed, wind direction, and most importantly, real world fog densities and fog event durations. These factors would need to be measured but they could impact collection

rates significantly. Wind direction in particular could artificially change the wire spacing depending on how far it's rotated. CFD could also be essential to understanding these experiments and be paired with experimental test results to find the optimal harp setups.

The other major path for fog harvesting is electrification. Corona discharge has been used in the past to get above 80% collection efficiency [12], and this should be possible for these harps as well. Some design changes may need to be made for the setup to work properly in order to ensure the wires are electrified properly, but it is definitely a route to explore.

For soilds on oil-infused microstructured surfaces, there's a lot of fundamental work to be done still. Even for the experiments that were done, some results still need to be modeled and explained. On top of the turning of the cube, there needs to be modeling for consecutive trials, in particular the oil drainage from each pull of the cube, as the structure could . The other piece that is missing is when a solid object is unable to move. This confinement could increase the friction for larger oils while these experiments didn't see that. There's still much to do for this to have been studied systemically.

Appendices

Appendix A

Programming Pseuocode

A.1 Defrosting Image Analysis

The experiments for the dewetting were done on an aluminum plate that was treated to be half hyrdophobic and half superhydrophobic, divided evenly down the middle. A sample area was cropped from each side of the plate, avoiding edges of the plate and the center line where the meltwater can be influenced by both sides of the plate. Both areas always start as completely covered in frost, allowing us to use the first frames as comparion points for the rest of the videos, since the frost appears as white compared to the grey of the aluminum seen through the droplets. A time is taken for the conversion of 50% of the meltwater dewetting. This controls the switch in the program from tracking frost to meltwater. An edge finding method was used to identify droplets after melting.

Inputs:

- File name
- Edge finding length
- Melt time

1. Get initial frame
2. for (All images in stack)
    (a) If (Before melt time)
        i. for (All x)
        ii. for (All y)
        iii. Compare to initial frame
        iv. Mark if covered or not
    (b) Else
        i. for (All x)
        ii. for (All y)

iii. Find edges-Find Droplets
iv. Mark covered pixels

(c) Sum for area

Mask figure here

A.2 Droplet Bridge Image Analysis

The code was written from scratch for a local system in Java. The high speed videos were converted from Cine files to AVIs and then split to individual images for each frame. The images were ordered in folders given their frame count as a name. The pseudo code for the image analysis follows.

Inputs:

- Video name(Directs to folder)
- Frame rate
- Surface positions(in pixels)
- Beginning and end of analysis(frame numbers)
- Zoom factor used for the video
- Volume of the droplet
- Pore size
- Image averaging radius
- Wetting to wicking transition
- SHPB switch

1. For (All images)
   (a) Create new image object
   (b) For (All x)
      i. For (All y)
         A. Get average value for each pixel using averaging radius
   (c) For (y between surface positions)

i. Find max increase in pixel values(Right edge of bridge)
ii. Find max decrease in pixel values(Left edge of bridge)
iii. Save positions

(d) For (y between surface positions)
i. Check if values are too different from nearby values
A. Anything > (threshold) x coordinates away is marked
B. 30 typical value used.

(e) Remove outlier points

(f) Generate image showing raw data points taken to compare to raw image

(g) Generate text file with the raw data points organized by y-position.

(h) (Taylor series approximations were used to fill in gaps but this was determined to produce less accurate bridge captures and was not used in final processing)

(i) Fit a polynomial to each of the bridge sides
i. Attempted polynomial orders between order 2 and 5, order 4 was typically the most accurate.
ii. $R^2 > 0.99$ for most fits with coefficients having less than 1% error compared to fits generated in Excel.

(j) Store polynomial coefficients

(k) Generate text file with points used for fitting and the resulting coefficients

2. For (All images)

(a) Generate image plotting the two fits for the bridge shape between the two surfaces for comparison to raw data

3. For (All images)

(a) Calculate the desired information using the polynomial fits to get instantaneous/local values for first and second derivatives.
i. Laplace pressures
ii. Contact radii
iii. Contact angles

(b) Store desired info in text files

An example of an experimental image and the two resulting images from the program are below.

Figure S1: The first image is a single frame directly from the video. The second image is the raw data points for the bridge shape and midline of the bridge. The third image is the fitted polynomials with the receiving contact diameter.

A.3 Wicking Modeling

The wicking simulation for Chapter 4 needed to numerically solve for the shape of the liquid bridge between the two surfaces. This is possible because the Laplace pressure of the bridge is a constant across the bridge. The solution used an intrinsic shooting method, with 4 constraints and 3 unknowns. The 4 constraints are the contact angles on each of the surfaces, the height of the gap, and the volume of the liquid bridge. The 3 unknowns are the donor contact radius, the Laplace pressure, and the length of the path along the bridge profile, which is always greater than the height of the gap.

The program starts with some educated guesses for the unknowns and the constraints are all known. Using the initial values, the program interpolates the shape of the bridge using the equations in chapter 4. Once the bridge profile is estimated, the program checks the shape against all of the constraints, adjusting the unknown values based on the error. This is repeated until the error in the known constraints is less than 0.01%. The bridge shape is then used to calculate the Darcy's flow, moving to the next time step.

Bibliography

[1] N. G. Kowalski, W. Shi, B.S. Kennedy, and J.B. Boreyko. Optimizing fog harps. *ACS Appl. Mater. Interfaces*, 13:38826–38834, 2021.

[2] P. G. de Gennes. *Capillarity and wetting phenomena: drops, bubbles, pearls, waves*. Springer Science & Business Media, 2013.

[3] H. Chen, A. Amirfazli, and T. Tang. Modeling liquid bridge between surfaces with contact angle hysteresis. *Langmuir*, 29:3310–3319, 2013.

[4] C. Antonini, F. J. Carmona, E. Pierce, M. Marengo, and A. Amirfazli. General methodology for evaluating the adhesion force of drops and bubbles on solid surfaces. *Langmuir*, 25:6143–6154, 2009.

[5] J. B. Boreyko, B. R. Srijanto, T. D. Nguyen, C. Vega, M. Fuentes-Cabrera, and C. P. Collier. Dynamic defrosting on nanostructured superhydrophobic surfaces. *Langmuir*, 29:9516–9524, 2013.

[6] Q. Xu, J. Li, J. Tian, J. Zhu, and X. Gao. Energy-effective frost-free coatings based on superhydrophobic aligned nanocones. *ACS Appl. Mater. Interfaces*, 6:8976–8980, 2014.

[7] Y. Wang, M. Li, T. Lv, Q. Wang, Q. Chen, and J. Ding. Influence of different chemical modifications on the icephobic properties of superhydrophobic surfaces in a condensate environment. *J. Mater. Chem.*, 3(9):4967–4975, 2015.

[8] F. Wang, C. Liang, and X. Zhang. Visualization study of the effect of surface contact angle on frost melting process under different frosting conditions. *Int. J. Refrigeration*, 64:143–151, 2016.

[9] O. Klemm, R.S. Schemenauer, A. Lummerich, P. Cereceda, V. Marzol, D. Corell, J. van Heerden, D. Reinhard, T. Gherezghiher, J. Olivier, P. Osses, J. Sarsour, E. Frost, M. J. Estrela, J. A. Valiente, and G. M. Fessehaye. Fog as a fresh-water resource: Overview and perspectives. *AMBIO*, 41:221–234, 2012.

[10] M. Quadir, G. Jiménez, R. Farnum, L. Dodson, and V. Smakhtin. Fog water collection: challenges beyond technology. *Water*, 10:372, 2018.

[11] W. Shi, M. J. Anderson, J. B. Tulkoff, B. S. Kennedy, and J. B. Boreyko. Fog harvesting with harps. *ACS Appl. Mater. Interfaces*, 10:11979–11986, 2018.

[12] S. Sharifvaghefi and H. Kazerooni. Fog harvesting: combination and comparison of different methods to maximize the collection efficiency. *SN Appl. Sci.*, 3:516, 2021.

[13] Y. Jiang, R. Xu, S. Liu, G. Liu, and X Yan. Electrostatic fog collection mechanism and design of an electrostatic fog collector with nenear perfect fog collection efficiency. *Chem. Eng. Sci.*, 247:117034, 2021.

[14] S. Nath, S. F. Ahmadi, and J. B. Boreyko. A review of condensation frosting. *Nanosc. Microsc. Therm.*, 21:81–101, 2017.

[15] M. J. Kreder, J. Alvarenga, P. Kim, and J. Aizenberg. Design of anti-icing surfaces: smooth, textured or slippery? *Nat. Rev. Mater.*, 1:15003, 2016.

[16] T. M. Schutzius, S. Jung, T. Maitra, P. Eberle, C. Antonini, C. Stamatopoulos, and D. Poulikakos. Physics of icing and rational design of surfaces with extraordinary icephobicity. *Langmuir*, 31:4807–4821, 2015.

[17] D. Quéré. Non-sticking drops. *Rep. Prog. Phys.*, 68:2495–2532, 2005.

[18] H. Wang, L. Tang, X. Wu, W. Dai, and Y. Qiu. Fabrication and anti-frosting performance of super hydrophobic coating based on modified nano-sized calcium carbonate and ordinary polyacrylate. *Appl. Surf. Sci.*, 253:8818–8824, 2007.

[19] S. Jung, M. Dorrestijn, D. Raps, A. Das, C. M. Megaridis, and D. Poulikakos. Are superhydrophobic surfaces best for icephobicity? *Langmuir*, 27:3059–3066, 2011.

[20] M. Wen, L. Wang, M. Zhang, L. Jiang, and Y. Zheng. Antifogging and icing-delay properties of composite micro-and nanostructured surfaces. *ACS Appl. Mater. Interfaces*, 6(6):3963–3968, 2014.

[21] A. Alizadeh, M. Yamada, R. Li, W. Shang, S. Otta, S. Zhong, L. Ge, A. Dhinojwala, K. R. Conway, V. Bahadur, A. J. Vinciquerra, B. Stephens, and M. L. Blohm. Dynamics of ice nucleation on water repellent surfaces. *Langmuir*, 28:3180–3186, 2012.

[22] L. Boinovich, A. M. Emelyanenko, V. V. Korolev, and A. S. Pashinin. Effect of wettability on sessile drop freezing: when superhydrophobicity stimulates an extreme freezing delay. *Langmuir*, 30:1659–1668, 2014.

[23] P. Guo, Y. Zheng, M. Wen, C. Song, Y. Lin, and L. Jiang. Icephobic/anti-icing properties of micro/nanostructured surfaces. *Adv. Mater.*, 24:2642–2648, 2012.

[24] L. B. Boinovich and A. M. Emelyanenko. Anti-icing potential of superhydrophobic coatings. *Mendeleev Commun.*, 23(1):3–10, 2013.

[25] P. Tourkine, M. Le Merrer, and D. Quéré. Delayed freezing on water repellent materials. *Langmuir*, 25:7214–7216, 2009.

[26] L. Cao, A. K. Jones, V. K. Sikka, J. Wu, and D. Gao. Anti-icing superhydrophobic coatings. *Langmuir*, 25:12444–12448, 2009.

[27] L. Mishchenko, B. Hatton, V. Bahadur, J. A. Taylor, T. Krupenkin, and J. Aizenberg. Design of ice-free nanostructured surfaces based on repulsion of impacting water droplets. *ACS Nano*, 4:7699–7707, 2010.

[28] T. Maitra, M. K. Tiwari, C. Antonini, P. Schoch, S. Jung, P. Eberle, and D. Poulikakos. On the nanoengineering of superhydrophobic and impalement resistant surface textures below the freezing temperature. *Nano Lett.*, 14:172–182, 2014.

[29] T. Maitra, C. Antonini, M. K. Tiwari, A. Mularczyk, Z. Imeri, P. Schoch, and D. Poulikakos. Supercooled water drops impacting superhydrophobic textures. *Langmuir*, 30(36):10855–10861, 2014.

[30] A. Lafuma and D. Quéré. Superhydrophobic states. *Nat. Mater.*, 2:457–460, 2003.

[31] K. A. Wier and T. J. McCarthy. Condensation on ultrahydrophobic surfaces and its effect on droplet mobility: ultrahydrophobic surfaces are not always water repellant. *Langmuir*, 22:2433–2436, 2006.

[32] K. K. Varanasi, T. Deng, J. D. Smith, M. Hsu, and N. Bhate. Frost formation and ice adhesion on superhydrophobic surfaces. *Appl. Phys. Lett.*, 97:234102, 2010.

[33] S. Farhadi, M. Farzaneh, and S. A. Kulinich. Anti-icing performance of superhydrophobic surfaces. *Appl. Surf. Sci.*, 257:6264–6269, 2011.

[34] J. Chen, J. Liu, M. He, K. Li, D. Cui, Q. Zhang, X. Zeng, Y. Zhang, J. Wang, and Y. Song. Superhydrophobic surfaces cannot reduce ice adhesion. *Appl. Phys. Lett.*, 101:111603, 2012.

[35] S. A. Kulinich, S. Farhadi, K. Nose, and X. W. Du. Superhydrophobic surfaces: are they really ice-repellent? *Langmuir*, 27:25–29, 2011.

[36] K. K. Lau, J. Bico, K. B. K. Teo, M. Chhowalla, G. A. J. Amaratunga, W. I. Milne, G. H. McKinley, and K. K. Gleason. Superhydrophobic carbon nanotube forests. *Nano Lett.*, 3:1701–1705, 2003.

[37] C. H. Chen, Q. Cai, C. Tsai, C. L. Chen, G. Xiong, Y. Yu, and Z. Ren. Dropwise condensation on superhydrophobic surfaces with two-tier roughness. *Appl. Phys. Lett.*, 90:173108, 2007.

[38] J. B. Boreyko and C. H. Chen. Self-propelled dropwise condensate on superhydrophobic surfaces. *Phys. Rev. Lett.*, 103:184501, 2009.

[39] R. Enright, N. Miljkovic, A. Al-Obeidi, C. V. Thompson, and E. N. Wang. Condensation on superhydrophobic surfaces: the role of local energy barriers and structure length scale. *Langmuir*, 28:14424–14432, 2012.

[40] N. Miljkovic, R. Enright, and E. N. Wang. Effect of droplet morphology on growth dynamics and heat transfer during condensation on superhydrophobic nanostructured surfaces. *ACS Nano*, 6:1776–1785, 2012.

[41] K. Rykaczewski. Microdroplet growth mechanism during water condensation on superhydrophobic surfaces. *Langmuir*, 28:7720–7729, 2012.

[42] Q. Zhang, M. He, X. Zeng, K. Li, D. Cui, J. Chen, J. Wang, Y. Song, and L. Jiang. Condensation mode determines the freezing of condensed water on solid surfaces. *Soft Matter*, 8:8285–8288, 2012.

[43] Y. Zhang, X. Yu, H. Wu, and J. Wu. Facile fabrication of superhydrophobic nanostructures on aluminum foils with controlled-condensation and delayed-icing effects. *Appl. Surf. Sci.*, 258:8253–8257, 2012.

[44] P. Kim, T. S. Wong, J. Alvarenga, M. J. Kreder, W. E. Adorno-Martinez, and J. Aizenberg. Liquid-infused nanostructured surfaces with extreme anti-ice and anti-frost performance. *ACS Nano*, 6:6569–6577, 2012.

[45] J. B. Boreyko and C. P. Collier. Delayed frost growth on jumping-drop superhydrophobic surfaces. *ACS Nano*, 7:1618–1627, 2013.

[46] Q. Zhang, M. He, J. Chen, J. Wang, Y. Song, and L. Jiang. Anti-icing surfaces based on enhanced self-propelled jumping of condensed water microdroplets. *Chem. Commun.*, 49:4516–4518, 2013.

[47] J. Guadarrama-Cetina, A. Mongruel, W. Gonzalez-Vinas, and D. Beysens. Percolation-induced frost formation. *Europhys. Lett.*, 101:16009, 2013.

[48] X. Chen, R. Ma, H. Zhou, X. Zhou, L. Che, S. Yao, and Z. Wang. Activating the microscale edge effect in a hierarchical surface for frosting suppression and defrosting promotion. *Sci. Rep.*, 3:2515, 2013.

[49] J. Petit and E. Bonaccurso. General frost growth mechanism on solid substrates with different stiffness. *Langmuir*, 30:1160–1168, 2014.

[50] Q. Hao, Y. Pang, Y. Zhao, J. Zhang, J. Feng, and S. Yao. Mechanism of delayed frost growth on superhydrophobic surfaces with jumping condensates: more than interdrop freezing. *Langmuir*, 30:15416–15422, 2014.

[51] J. B. Boreyko, R. R. Hansen, K. R. Murphy, S. Nath, S. T. Retterer, and C. P. Collier. Controlling condensation and frost growth with chemical micropatterns. *Sci. Rep.*, 6:19131, 2016.

[52] S. Nath and J. B. Boreyko. On localized vapor pressure gradients governing condensation and frost phenomena. *Langmuir*, 32:8350–8365, 2016.

[53] Y. Zhao and C. Yang. Retarded condensate freezing propagation on superhydrophobic surfaces patterned with micropillars. *Appl. Phys. Lett.*, 108:061605, 2016.

[54] T. S. Wong, S. H. Kang, S. K. Y. Tang, E. J. Smythe, B. D. Hatton, A. Grinthal, and J. Aizenberg. Bioinspired self-repairing slippery surfaces with pressure-stable omniphobicity. *Nature*, 477:443–447, 2011.

[55] S. B. Subramanyam, K. Rykaczewski, and K. K. Varanasi. Ice adhesion on lubricant-impregnated textured surfaces. *Langmuir*, 29:13414–13418, 2013.

[56] K. Rykaczewski, S. Anand, S. B. Subramanyam, and K. K. Varanasi. Mechanism of frost formation on lubricant-impregnated surfaces. *Langmuir*, 29:5230–5238, 2013.

[57] K. Golovin, S.P. Kobaku, D. H. Lee, E. T. DiLoreto, J. M. Mabry, and A. Tuteja. Designing durable icephobic surfaces. *Sci. Adv.*, 2:e1501496, 2016.

[58] D. L. Beemer, W. Wang, and A. K. Kota. Durable gels with ultra-low adhesion to ice. *J. Mater. Chem. A*, 4:18253–18258, 2016.

[59] S. B. Subramanyam, V. Kondrashov, J. Rühe, and K. K. Varanasi. Low ice adhesion on nano-textured superhydrophobic surfaces under supersaturated conditions. *ACS Appl. Mater. Interfaces*, 8:12583–12587, 2016.

[60] Y. Zhang, M. R. Klittich, M. Gao, and A. Dhinojwala. Delaying frost formation by controlling surface chemistry of carbon nanotube-coated steel surfaces. *ACS Appl. Mater. Interfaces*, 9:6512–6519, 2017.

[61] S. Wang, W. Zhang, X. Yu, C. Liang, and Y. Zhang. Sprayable superhydrophobic nano-chains coating with continuous self-jumping of dew and melting frost. *Sci. Rep.*, 7:40300, 2017.

[62] Z. Zuo, R. Liao, X. Zhao, X. Song, Z. Qiao, C. Guo, A. Zhuang, and Y. Yuan. Anti-frosting performance of superhydrophobic surface with zno nanorods. *Appl. Therm. Eng.*, 110:39–48, 2017.

[63] J. Wu, L. Zhang, Y. Wang, and P. Wang. Efficient and anisotropic fog harvesting on a hybrid and directional surface. *Adv. Mater. Interfaces*, 4:1600801, 2017.

[64] M. A. Rahman and A. M. Jacobi. Drainage of frost melt water from vertical brass surfaces with parallel microgrooves. *Int. J. Heat Mass Transfer*, 55:1596–1605, 2012.

[65] T. Matsubayashi, M. Tenjimbayashi, K. Manabe, M. Komine, W. Navarrini, and S. Shiratori. Integrated anti-icing property of super-repellency and electrothermogenesis exhibited by pedot:pss/cyanoacrylate composite nanoparticles. *ACS Appl. Mater. Interfaces*, 8:24212–24220, 2016.

[66] M. Elsharkawy, D. Tortorella, S. Kapatral, and C. M. Megaridis. Combating frosting with joule-heated liquid-infused superhydrophobic coatings. *Langmuir*, 32:4278–4288, 2016.

[67] F. Chu, X. Wu, and Y. Zhu. Defrosting on horizontal hydrophobic surfaces and the shrink angle. *Int. J. Refrig.*, 71:1–7, 2016.

[68] F. Wang, C. Liang, Y. Zhang, and X. Zhang. Defrosting performance of superhydrophobic fin-tube heat exchanger. *Appl. Therm. Eng.*, 113:229–237, 2017.

[69] W. Vedder and D. A. Vermilyea. Aluminum + water reaction. *Trans. Faraday Soc.*, 65:561–584, 1969.

[70] M. He, X. Zhou, X. Zeng, D. Cui, Q. Zhang, J. Chen, H. Li, J. Wang, Z. Cao, Y. Song, and L. Jiang. Hierarchically structured porous aluminum surfaces for high-efficient removal of condensed water. *Soft Matter*, 8:6680–6683, 2012.

[71] X. Qu, J. B. Boreyko, F. Liu, R. L. Agapov, N. V. Lavrik, S. T. Retterer, J. J. Feng, C. P. Collier, and C. H. Chen. Self-propelled sweeping removal of dropwise condensate. *Appl. Phys. Lett.*, 106:221601, 2015.

[72] A. Kim, C. Lee, H. Kim, and J. Kim. Simple approach to superhydrophobic nanostructured al for practical antifrosting application based on enhanced self-propelled jumping droplets. *ACS Appl. Mater. Interfaces*, 7:7206–7213, 2015.

[73] Z. Liu, Y. Gou, J. Wang, and S. Cheng. Frost formation on a super-hydrophobic surface under natural convection conditions. *Int. J. Heat Mass Transfer*, 51:5975–5982, 2008.

[74] C. G. L. Furmidge. Studies at phase interfaces i. the sliding of liquid drops on solid surfaces and a theory for spray retention. *J. Colloid Sci.*, 17:309–324, 1962.

[75] W. Wang, J. Xiao, Q. C. Guo, W. P. Lu, and Y. C. Feng. Field test investigation of the characteristics for the air source heat pump under two typical mal-defrost phenomena. *Appl. Energy*, 88:4470–4480, 2011.

[76] W. Wang, J. Xiao, Y. Feng, Q. Guo, and L. Wang. Characteristics of an air source heat pump with novel photoelectric sensors during periodic frost-defrost cycles. *Appl. Therm. Eng.*, 50:177–186, 2013.

[77] C. Stamatopoulos, J. Hemrle, D. Wang, and D. Poulikakos. Exceptional anti-icing performance of self-impregnating slippery surfaces. *ACS Appl. Mater. Interfaces*, 9:10233–10242, 2017.

[78] X. Sun, V. G. Damle, A. Uppal, R. Linder, S. Chandrashekar, A. R. Mohan, and K. Rykaczewski. Inhibition of condensation frosting by arrays of hygroscopic antifreeze drops. *Langmuir*, 31:13743–13752, 2015.

[79] H. Chen, T. Tang, and A. Amirfazli. Fast liquid transfer between surfaces: breakup of stretched liquid bridges. *Langmuir*, 31:11470–11476, 2015.

[80] A. D. Gat, H. K. Navaz, and M. Gharib. Wicking of a liquid bridge connected to a moving porous surface. *J. Fluid Mech.*, 703:315–325, 2012.

[81] H. Chen, T. Tang, and A. Amirfazli. Liquid transfer mechanism between two surfaces and the role of contact angles. *Soft Matter*, 10:2503–2507, 2014.

[82] H. Chen, T. Tang, H. Zhao, K.-Y. Law, and A. Amirfazli. How pinning and contact angle hysteresis govern quasi-static liquid drop transfer. *Soft Matter*, 12:1998–2008, 2016.

[83] X. Yan, F. Chen, C. Zhao, Y. Qin, X. Wang, K.F. Rabbi, M.J. Hoque, H. Zhao, J. Li, T. Gebrael, F. Chen, J. Feng, and N. Miljkovic. Near field condensation. Unpublished, available online at Research Square, 2020.

[84] M. Edalatpour, K. R. Murphy, R. Mukherjee, and J. B. Boreyko. Bridging-droplet thermal diodes. *Adv. Funct. Mater.*, 30:2004451, 2020.

[85] T.P. Koukoravas, G. Damoulakis, and C.M. Megaridis. Experimental investigation of a vapor chamber featuring wettability-patterned surfaces. *Appl. Therm. Eng.*, 178:115522, 2020.

[86] J. B. Boreyko, G. Polizos, P. G. Datskos, S. A. Sarles, and C. P. Collier. Air-stable droplet interface bilayers on oil-infused surfaces. *Proc. Natl. Acad. Sci. U.S.A.*, 111:7588–7593, 2014.

[87] B. Qian and K.S. Breuer. The motion, stability and breakup of a stretching liquid bridge with a receding contact line. *J. Fluid Mech.*, 666:554–572, 2011.

[88] S. J. Kim, K. Fezzaa, J. An, T. Sun, and S. Jung. Capillary spreading of contact line over a sinking sphere. *Appl. Phys. Lett.*, 111:134102, 2017.

[89] F. Fu, P. Li, K. Wang, and R. Wu. Numerical simulation of sessile droplet spreading and penetration on porous substrates. *Langmuir*, 35:2917–2924, 2019.

[90] N. Alleborn and H. Raszillier. Spreading and sorption of a droplet on a porous substrate. *Chem. Eng. Sci.*, 59:2071–2088, 2004.

[91] X. Frank and P. Perré. Droplet spreading on a porous surface: A lattice boltzmann study. *Phys. Fluids*, 24:042101, 2012.

[92] A-L. Biance, C. Clanet, and D. Quéré. First steps in the spreading of a liquid droplet. *Phys. Rev. E*, 69:016301, 2004.

[93] S. Mitra and S.K. Mitra. Understanding the early regime of drop spreading. *Langmuir*, 32:8843–8848, 2016.

[94] J. Eggers, J. R. Lister, and H. A. Stone. Coalescence of liquid drops. *J. Fluid Mech.*, 401:293–310, 1999.

[95] J. D. Paulsen, J. C. Burton, and S. R. Nagel. Viscous to inertial crossover in liquid drop coalescence. *Phys. Rev. Lett.*, 106:114501, 2011.

[96] J.D. Paulsen, J.C. Burton, S.R. Nagel, S. Appathurai, M.T. Harris, and O.A. Basaran. The inexorable resistance of inertia determines the initial regime of drop coalescence. *Proc. Natl. Acad. Sci. U.S.A.*, 109:6857–6861, 2012.

[97] J.D. Paulsen, R. Carmigniani, A. Kannan, J.C. Burton, and S.R. Nagel. Coalsecence of bubbles and drops in an outer fluid. *Nat. Commun.*, 5:3182, 2013.

[98] A. Keiser, L. Keiser, C. Clanet, and D. Quéré. Drop friction on liquid-infused materials. *Soft Matter*, 13:6981–6987, 2017.

[99] D. Daniel, J. V. I. Timonen, R. Li, S. J. Velling, and J. Aizenberg. Oleoplaning droplets on lubricated surfaces. *Nat. Phys.*, 13:1020–1025, 2017.

[100] J.H. Snoeijer and B. Andreotti. Moving contact lines: Scales, regimes, and dynamical transitions. *Annu. Rev. Fluid Mech.*, 45:269–292, 2013.

[101] J. Bear. *Dynamics of Flow in Porous Media*. Dover Publications, 1988.

[102] S. Gruener, T. Hofmann, D. Wallacher, A. V. Kityk, and P. Huber. Capillary rise of water in hydrophilic nanopores. *Phys. Rev. E.*, 79:067301, 2009.

[103] I. Martínez and J.M. Perales. Liquid bridge stability data. *J. Cryst. Growth*, 78:369–378, 1986.

[104] A. E. Ercin and A. Y. Hoekstra. Water footprint scenarios for 2050: A global analysis. *Environ. Int*, 64:71–82, 2014.

[105] S.L. Postel. Entering an era of water scarcity: The challenges ahead. *Ecol. Appl.*, 10:941–948, 2000.

[106] D. Gerten, J. Heinke, H. Hoff, H. Biemans, M. Fader, and K. Waha. Global water availability and requirements for future food production. *J. Hydrometeorol.*, 12:885–899, 2011.

[107] R.S. Schemenauer and P.I. Joe. The collection efficiency of a massive fog collector. *Atmos. Res.*, 24:53–69, 1989.

[108] J. d. D. Rivera. Aerodynamic collection efficiency of fog water collectors. *Atmos. Res.*, 102:335–342, 2011.

[109] K.-C. Park, S.S. Chhatre, S. Srinivasan, R.E. Cohen, and G.H. McKinley. Optimal design of permeable fiber network structures for fog harvesting. *Langmuir*, 29:13269–13277, 2013.

[110] W. Shi, L. De Koninck, B. Hart, N. Kowalski, A. Fugaro, T. van der Sloot, R. Ott, B. Kennedy, and J. Boreyko. Harps under heavy fog conditions: superior to meshes but prone to tangling. *ACS Appl. Mater. Interfaces*, 10:12329, 2020.

[111] D. Daniel, M. N. Mankin, R. A. Belisle, T. S. Wong, and J. Aizenberg. Lubricant-infused micro/nano-structured surfaces with tunable dynamic omniphobicity at high temperatures. *Appl. Phys. Lett.*, 102:231603, 2013.

[112] A. Lafuma and D. Quéré. Slippery pre-suffused surfaces. *Europhys. Lett.*, 96:56001, 2011.

[113] J. D. Smith, R. Dhiman, S. Anand, E. Reza-Garduno, R. E. Cohen, G. H. McKinley, and K. K. Varanasi. Droplet mobility on lubricant-impregnated surfaces. *Soft Matter*, 9:1772–1780, 2013.

[114] E. Jenner and B. D'Urso. Wetting states on structured immiscible liquid coated surfaces. *Appl. Phys. Lett.*, 103:251606, 2013.

Life before death, strength before weakness, journey before destination. "I will take responsibility for what I have done. If I must fall, I will rise each time a better man." Oathbringer-Brandon Sanderson